Plasma Physics Reports, Vol. 28, No. 1, 2002, pp. 1–6. Translated from Fizika Plazmy, Vol. 28, No. 1, 2002, pp. 3–8.
Original Russian Text Copyright © 2002 by Leonov.

TOKAMAKS

Simulations of Tokamak Discharges with Fast L–H Transitions

V. M. Leonov

Institute of Nuclear Fusion, Russian Research Centre Kurchatov Institute, pl. Kurchatova, Moscow, 123182 Russia

Received March 22, 2001

Abstract—Results are presented from the simulations of discharges with fast L–H transitions in the JET tokamak. During a transition, electron temperature perturbations propagate into the plasma core over a time much shorter than the transport time characteristic of this device. It is shown that the experimentally observed variations in the electron temperature may be caused by the change in the particle source intensity in the plasma when the atomic flux decreases, which is detected from the drop in the intensity of the D_α hydrogen spectral line. Hence, the experiments under consideration can be explained without the assumption about the nonlocal character of transport processes in tokamaks, which was made in some papers devoted to JET experiments. The plasma component responsible for the apparent nonlocal character of transport processes is the neutral component, whose propagation time across the plasma column is sufficiently short ($t < 100$ μs). © *2002 MAIK "Nauka/Interperiodica".*

1. INTRODUCTION

To date, several types of discharges with improved confinement (as compared to the usual discharge, referred to as the L-mode) have been obtained in tokamaks. The fundamental and best understood improved confinement mode is the so-called H-mode obtained for the first time in the ASDEX tokamak [1]. H-mode discharges with different confinement qualities have been obtained almost in all tokamaks, which differ in size, parameters, and plasma heating methods. The H-mode confinement mode was chosen as the basic one for the next generation reactors: ITER and DEMO [2, 3]. A great body of experimental and theoretical data has been accumulated in studies of these modes and the transition from the L- to H-mode (the L–H transition) in tokamaks. However, available L–H transition models still fail to explain some aspects of the problem.

One of the characteristic features of the L–H transition, by which this transition is now distinguished, is a sudden and rapid drop in the emission intensity of the H_α (D_α) hydrogen spectral line, which is accompanied by an increase in the plasma density. In different regions of the plasma column, the emission intensity is reduced to different levels. In the scrape-off layer (SOL) and the divertor, the emission intensity drops by a factor of 10 or more. In the plasma core, the reduction is several times lower [4]. The reduction in the H_α emission intensity indicates the reduction in the hydrogen neutral flux into the plasma column. The consequences of such a significant reduction in the atomic flux have not yet been sufficiently analyzed.

The study of the dynamics of the L–H transition is of great interest, because it can throw light on the mechanisms governing transport processes both at the plasma edge and in the core and, in particular, on the coupling between them.

Early experiments showed that, after the L–H transition, plasma transport first decreases rather rapidly (over a time of ~100 μs) in a narrow (~1–2 cm wide) layer adjacent to the separatrix and, then, the region with a decreased plasma transport extends over the plasma core with characteristic transport times (tens to hundreds of milliseconds) [4–6].

However, the measurements of the radial electron temperature profile during an L–H transition in the JET tokamak (shot no. 26021) [7] showed that the change in T_e propagated into the plasma core (down to $\rho/\rho_{max} \sim 0.4$–0.5) over a time of ~4–7 ms, which is much shorter than transport times characteristic of this device. Later, similar results were also obtained in shots in other devices [8, 9].

Since no mechanisms were identified for such a rapid propagation of perturbations into the plasma core (except for the possible propagation of MHD perturbations), an analysis of these experiments allowed the authors of [10, 11] to conclude that transport processes in tokamaks are of nonlocal character and the confinement regime changes simultaneously throughout the plasma column. At present, paper [7] and other analogous papers present the experimental basis for theories describing the nonlocal (global) character of transport in tokamaks.

However, there does exist *a plasma component that can ensure a rapid propagation of a signal* into the plasma core. This is *the plasma neutral component.*

In many discharges, neutrals play a significant role in the plasma energy balance, being responsible for energy losses through convection and charge exchange of the bulk plasma with the heating beams during neu-

1063-780X/02/2801-0001$22.00 © 2002 MAIK "Nauka/Interperiodica"

tral beam injection (NBI). The ionization of neutrals is a source of cold electrons in the major part of the plasma column. Hence, a rapid change in the neutral flux into the plasma column (which is detected from the reduction of the H_α emission intensity during the L–H transition) can markedly change the plasma energy balance and can result in an additional heating of the plasma regions that are subject to the action of the neutral component.

It should be noted that the time during which neutrals propagate toward the center of the plasma column is very short (≤100 μs). Hence, the steady-state radial profiles of the neutral density on the time scale of interest (several milliseconds) form almost instantaneously, and the effects associated with the change in the neutral density also almost instantaneously extend over a major part of the plasma column.

It is of interest to consider in detail the consequences of the change in the neutral flux into the plasma during an L–H transition and to compare them quantitatively with experimental results.

In this paper, we present the results of detailed simulations of the JET discharge with an L–H transition described in [7]. The model takes into consideration the behavior of the plasma neutral component. The plasma region where the neutral component plays a significant role is determined. It is shown that the rapid propagation of the jump in T_e into the plasma core in discharges of this kind can be explained without recourse to the assumption about the nonlocal character of transport processes in tokamaks. These effects may be attributed to the behavior of the neutral component, which is responsible for the apparent nonlocal character of coupling in view of the fairly high velocity of neutrals.

In [12], a model was proposed that adequately describes discharges with a slow L–H transition and the decisive role of the time evolution of the particle source during such a transition was demonstrated. The results of [12] can be briefly formulated as follows. As the parameters of the SOL change during the L–H transition, the layer permeability to the hydrogen molecule beam (which feeds the plasma with particles) increases. As a result, the molecules reach plasma layers with a higher temperature and the character of their dissociation changes. In the SOL plasma with a lower temperature, the molecules usually dissociate into two atoms, whereas, in a hotter plasma, the dissociation of a molecule into an atom and an ion becomes important. Since the neutral source intensity in this case decreases by nearly one-half, the emission intensity of the H_α spectral line also decreases (the ions do not contribute to the H_α emission), although the total particle source does not change. In addition, the particle source that previously fed particles to the SOL, thus maintaining the high plasma density there, now shifts toward the plasma surface (into the layer of width ~1–2 cm adjacent to the separatrix). As a result, the density in this region increases and pedestals form in the radial density profiles. This, in turn, leads to a decrease (in inverse proportion to the density) in the electron heat conductivity at the plasma edge, the formation of thermal barriers, and the suppression of convection due to the flattening of the density profile in deeper plasma regions. As the radial profiles vary, the process gradually propagates into the plasma core. As was shown in [12, 13], this model provides a rather good quantitative description of discharges with L–H transitions in the ASDEX, DIII-D, and JET tokamaks [1, 14, 15].

In this paper, most attention is focused on the initial phase of the H-mode immediately after the L–H transition. This phase lasts for several tens of milliseconds and exhibits a rapid penetration of the T_e perturbation into the plasma core. In order to distinguish the effects related to the behavior of the neutral component, the plasma behavior immediately after the L–H transition was simulated using the fixed transport coefficients describing the behavior of the plasma parameters in the L-mode before the transition. We assume that, on longer time scales, the behavior of the plasma parameters in response to a change in the transport coefficients can be described by a model similar to that used in [12, 13] (a more detailed analysis of this problem is beyond the scope of this paper).

In Section 2, a model used in calculations is described. In Section 3, we present the results from the simulations of the initial phase of the H-mode and consider the role of the neutral component. In the Conclusion, the results obtained are discussed and some inferences are made.

2. DESCRIPTION OF THE MODEL

Simulations were performed with the 1.5D ASTRA code [16] for calculating the 2D equilibrium of the tokamak plasma column in the three-moment approximation, 1D transport, and the processes associated with NBI heating.

The heat and particle transport was described by the magnetic surface–averaged equations

$$\frac{\partial n_e}{\partial t} = -\frac{\partial}{\partial \rho}\Gamma_e + \sum S_{\text{ion}}, \quad (1)$$

$$\frac{3}{2}\frac{\partial (n_e T_e)}{\partial t} = -\frac{\partial}{\partial \rho} q_e + \sum P_e, \quad (2)$$

$$\frac{3}{2}\frac{\partial (n_i T_i)}{\partial t} = -\frac{\partial}{\partial \rho} q_i + \sum P_i, \quad (3)$$

where $\Gamma_e = -D_e\frac{\partial n_e}{\partial \rho} + n_e V_p$, $q_{e,i} = -n_{e,i}\chi_{e,i}\frac{\partial T_{e,i}}{\partial \rho} + (5/2)\Gamma_{e,i}T_{e,i}$, t is time, ρ is the label of the magnetic surface, $n_e = \sum Z_i n_i$, and $\Gamma_e = \sum Z_i \Gamma_i$.

The ionization source S_{ion} is the sum of the sources related to the ionization of atoms arriving from the

plasma edge (S_{ia}) and atoms of the heating beam ($S_{\rm NBI}$) and the source of particles produced immediately by dissociation of molecules (S_{im}):

$$\sum S_{\rm ion} = S_{ia} + S_{\rm NBI} + S_{im}.$$

The heat sources and sinks are written in the following form:

$$\sum P_e = P_{\rm OH} + P_{e-{\rm NBI}} - P_{ei} - P_{\rm rad} - P_{e-n_0},$$

$$\sum P_i = P_{i-{\rm NBI}} + P_{ei} - P_{i-n_0},$$

where $P_{\rm OH}$ is the Ohmic heating power, $P_{e-{\rm NBI}}$ and $P_{i-{\rm NBI}}$ are the powers transferred to electrons and ions from the heating beam, P_{ei} describes the Coulomb heat exchange between electrons and ions, $P_{\rm rad}$ is the radiative loss power, and $P_{e,\,i-n_0}$ are the electron and ion heat sinks related to the interaction with neutrals (the ionization loss for electrons and the charge-exchange loss for ions).

The behavior of the neutral component was described by the kinetic equation in the flat slab approximation. This approximation seems to be quite applicable to atoms arriving from the plasma periphery, because the JET tokamak has an elongated cross section and the plasma thickness with respect to charge exchange and ionization is high. It will be shown below that, in the plasma core (at $\rho/\rho_{\rm max} < 0.4$–$0.5$), where the flat slab approximation may be incorrect, the particles are mainly produced by the heating beams.

When calculating the radial neutral density profile, we used a simplified model for the recycling of atoms near the wall. It was assumed that the atomic flux into the plasma consists of the fluxes of cold and warm atoms. The cold atoms are produced via the dissociation of deuterium atoms arriving from the wall and the gas puffing system. The warm atom flux is the sum of the flux of fast atoms produced via molecule dissociation and the atomic flux that is formed when the atoms and plasma ions escaping from the plasma are reflected from the discharge chamber wall. This model is described in more detail in [17]. The model was calibrated with the atomic distribution function measured from the Doppler profile of the H_β line in the T-11 tokamak [18]. Calculations with allowance for recycling gave the characteristic energies of two groups of atoms (~1.8 eV and ~20 eV, which are close to the experimental ones) and the proportion between the populations of these groups (1 : 0.25).

In order to more clearly demonstrate the effects associated with the behavior of the neutral component (neglecting possible variations in the transport coefficients), we present the results of simulations with the use of the following model transport coefficients that are independent of the plasma parameters and do not change during the initial phase of the L–H transition:

$$\chi_e = D = \chi_i = \kappa(1 + 3(r/a)^3),$$
$$V_p = -0.25Dr/a^2. \qquad (4)$$

The radial dependence of the transport coefficients and the normalization factor κ were chosen such that, in the L-mode before the L–H transition, the experimental radial profiles of the plasma parameters (in particular, the profile $T_e(r)$) are well reproduced by the model. These coefficients remained fixed in the course of calculations of the time evolution of the plasma parameters. Such an approach should inevitably lead to a discrepancy between the calculation and experiment on the time scale comparable to the characteristic transport time. However, it allowed us to single out the effects related to the behavior of the neutral component at the first several tens of milliseconds. Slower variations of the plasma parameters were simulated in [12, 13].

The atomic influxes were chosen so as to provide a density growth rate consistent with the experiment under consideration.

3. SIMULATION RESULTS

In simulations, the L–H transition was initiated (in accordance with the results of [12] and the time behavior of the H_α emission measured in [7]) by reducing the flux of cold atoms into the plasma by nearly one-half and introducing the corresponding ion source at the plasma edge for the behavior of the average plasma density to coincide with the experiment.

As was already noted in the Introduction, it was shown in [12] that such a behavior of the particle source is related to the fact that hydrogen molecules penetrate deeper into the plasma in the H-mode and the dominant dissociation channel is the dissociation of a molecule into an atom and an ion, instead of two atoms as in the L-mode, when dissociation proceeds in colder peripheral regions of the plasma column.

Simulations show that, within the time interval under consideration (~10–30 ms), the radial density profile has no time to vary significantly and the main effects are associated with the change in the hydrogen neutral density in the plasma column.

Figure 1 illustrates how the particle source calculated for the discharge of interest varies during the L–H transition. The particle source consists of two components. In the central region of the plasma column, the particle source produced by the heating beam of fast neutrals is dominant. As the distance from the plasma axis increases, the intensity of this source decreases and the source of neutrals arriving from the plasma periphery becomes dominant.

Since the particle source, in essence, reflects the distribution of atoms across the plasma column, it becomes clear from an analysis of this figure why the effects from neutrals arriving from the plasma periph-

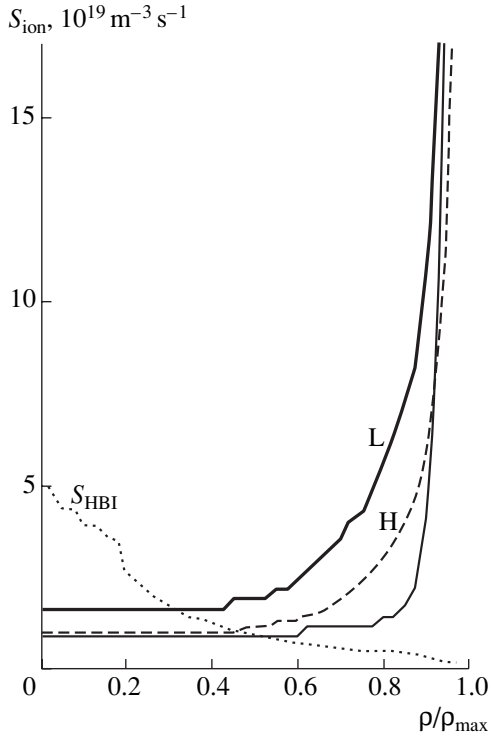

Fig. 1. Results of the simulations of the ionization particle source intensity S_{ion} for the L- and H-modes in JET (shot no. 26021) with allowance for the recycling of atoms (heavy and dashed lines, respectively) and without recycling (light line); S_{NBI} is the ionization source intensity related to the heating beam.

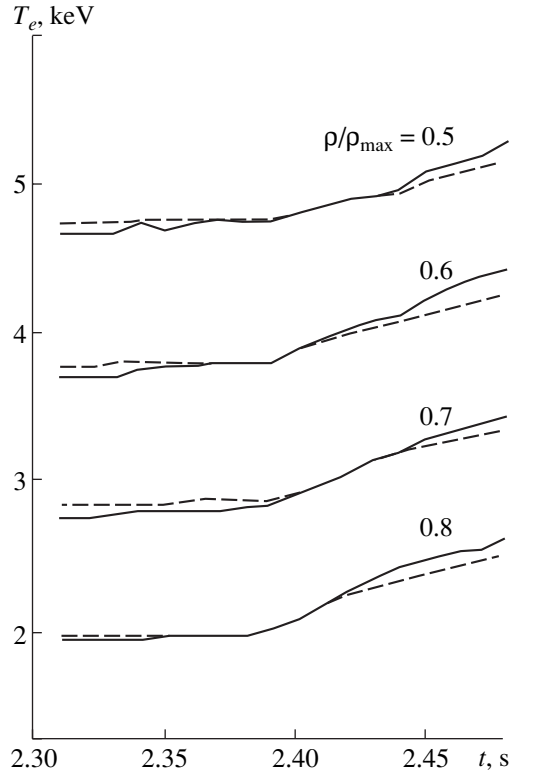

Fig. 2. Comparison of the time dependence of the electron temperature in JET (shot no. 26021) measured from the plasma electron cyclotron emission at different radii (solid lines) with the calculated one (dashed lines).

ery are experimentally detectable during the L–H transition only for $\rho/\rho_{max} \gtrsim 0.4$–$0.5$ and are absent in deeper plasma regions [7]. In deeper regions, the dominant role is played by the source of atoms from the heating beam S_{NBI}, which varies only slightly.

The mean energy of the warm atom component calculated by the recycling model is $E^w_{n_0} \approx 100$ eV, the energy of the cold component is ~2 eV, and the density ratio between the warm and cold components at the plasma edge is $n^w_0/n^c_0 \approx 20\%$.

Figure 1 also shows the curve corresponding to the calculations of the plasma particle source related to the ionization of neutral influxes without allowance for recycling. This curve corresponds to a neutral energy of 2 eV, which is often used in such calculations. It can be seen that such calculations give a substantially underestimated particle source intensity for the plasma core; it is appreciable only near the edge. For this reason, such calculations do not allow one to reveal the effect of neutrals at $\rho/\rho_{max} < 0.7$.

Simulations show that, in this case, the main change in the electron energy balance is due to the change in the cold electron source related to the ionization of atoms. The convection losses change only slightly because the radial plasma density profile has no time to vary. The charge exchange affects the ion component. The heating beam losses change; however, this change does not exceed several percent in this discharge. It should be noted that, if the heating beam losses changed more strongly, this might be noticed in the central region, which is not observed experimentally.

The role of the particle source during the L–H transition can be traced by analyzing the equations for the electron temperature and density. Substituting the density derivative from Eq. (1) into Eq. (2), we obtain the following equation:

$$\frac{3}{2}n_e\frac{\partial T_e}{\partial t} = \frac{3}{2}T_e\frac{\partial}{\partial\rho}\Gamma_e - \frac{\partial}{\partial\rho}q_e + \sum P_e - \frac{3}{2}T_e\sum S_{ion}. \quad (5)$$

At early times after the L–H transition, the conductivity heat fluxes in this model do not change, because the radial profiles are still unchanged and the transport coefficients are constant. Among the heat sources, only the heat source related to the ionization of atoms changes. However, the intensity of this source is low. If we neglect this source, then we can see that the change

in T_e is related precisely to the change in the particle source intensity:

$$\Delta\left(\frac{\partial T_e}{\partial t}\right)_{\text{L–H}} = \left.\frac{\partial T_e}{\partial t}\right|_{\text{H}} - \left.\frac{\partial T_e}{\partial t}\right|_{\text{L}} = \frac{T_e}{n_e}\left(\sum S_{\text{ion}}|_{\text{L}} - \sum S_{\text{ion}}|_{\text{H}}\right). \quad (6)$$

The final simulation results for the time interval including the beginning of the H-mode are shown in Fig. 2, where the time dependences of the calculated electron temperature at different radii are compared with those determined experimentally [7].

We see that the simulation results describe well the experimental behavior of T_e, particularly, within the time interval of interest to us (the first several tens of milliseconds after the L–H transition).

An increasing discrepancy at later times is a consequence of the use of the model time-independent transport coefficients. In the actual experiment, the radial profiles of the plasma parameters change after the L–H transition, which causes the transport coefficients to change accordingly. As was shown in [12], the use of more complicated (dependent on density and temperature) transport coefficients makes it possible to adequately describe the slow variations of the plasma parameters after the L–H transition.

4. CONCLUSION

In this paper, we have presented the results from simulations of one of the most typical JET discharges with a fast L–H transition [7], when the penetration of electron temperature variations into the plasma core (down to $\rho/\rho_{\max} \sim 0.4$–$0.5$) occurs over a time on the order of several milliseconds, which is much shorter than transport times characteristic of this device. Most attention was focused on studying the effects associated with the change in the hydrogen neutral density during the L–H transition, which was detected from the change in the H_α emission intensity.

Simulations have shown that the change in the growth rate of T_e at $\rho/\rho_{\max} \gtrsim 0.4$–$0.5$ during the L–H transition is mainly due to the decrease in the intensity of the cold electron source related to the ionization of hydrogen atoms in the plasma. The charge-exchange losses of the decelerated ions from the injected beams also slightly decrease; however, for the given discharge, the corresponding contribution comprises only several percent, which is detectable only for the ion component.

The study of the radial dependence of the particle source intensity makes it possible to explain why the effect is detectable only for $\rho/\rho_{\max} \gtrsim 0.4$–$0.5$. In deeper regions, the main source is related to the heating-beam atoms; this source does not change during the L–H transition.

When calculating the radial profiles of the atomic density and the ionization source intensity, it is necessary to take into account the recycling of atoms at the wall, because they penetrate deeper into the plasma due to the presence of the fast neutral component, which is formed when the charge exchange ions and atoms are reflected from the elements of the device construction. As a result, the source of atoms arriving from the plasma periphery becomes detectable against the background of the source of atoms from the heating beam in the deeper regions of the plasma.

The results obtained allow us to conclude that the neutral plasma component may be responsible for the apparent nonlocal character of certain processes occurring during the L–H transition (the propagation of electron temperature perturbations over a time shorter than the characteristic particle and energy transport times). Variations in the electron temperature immediately after the L–H transition can be described well even with the time-independent transport coefficients.

Finally, note that, since it is possible to explain the mentioned JET experiments by rather simple, elementary effects, these experiments cannot be considered as unambiguous evidence of the nonlocal character of transport processes in tokamaks. In other similar cases, it is necessary to perform an additional analysis with allowance for the behavior of the neutral plasma component. Taking into account the contribution of the neutral component will allow one to more correctly estimate the role of different mechanisms for the onset of the L- and H-modes in tokamaks.

REFERENCES

1. F. Wagner, G. Becker, K. Behringer, *et al.*, Phys. Rev. Lett. **49**, 1408 (1982).
2. *Technical Basis for the ITER-FEAT Outline Design* (2000).
3. *Project RF DEMO* (RRC Kurchatov Institute, Moscow, 2000), Part IV.
4. Asdex Team, Nucl. Fusion **29** (11), 1959 (1989).
5. R. J. Groebner, Preprint No. GA-A21128 (General Atomics, San Diego, 1992).
6. P. Gohil, K. H. Burrell, E. J. Doyle, *et al.*, Nucl. Fusion **34**, 1057 (1994).
7. S. V. Neudatchin, J. G. Cordey, D. G. Muir, *et al.*, Preprint No. JET-P(93)58 (JET, Ebington, 1992); S. V. Neudatchin, J. G. Cordey, and D. G. Muir, in *Proceedings of the 20th EPS Conference on Controlled Fusion and Plasma Physics, Lisbon, 1993*, Part I, p. 83; ECA **17C** (1), 83 (1993).
8. T. K. Kurki-Suonio, K. H. Burrell, R. J. Groebner, *et al.*, Nucl. Fusion **33**, 301 (1993).
9. S. V. Neudatchin, H. Shirai, T. Takizuka, *et al.*, in *Proceedings of the 22nd EPS Conference on Controlled Fusion and Plasma Physics, Bournemous, 1995*, Part III, p. 29; ECA **19C** (3), 29 (1995).
10. J. G. Cordey, D. G. Muir, S. V. Neudatchin, *et al.*, Plasma Phys. Controlled Fusion **36**, A267 (1994).

11. J. G. Cordey, D. G. Muir, V. V. Parail, *et al.*, Nucl. Fusion **35**, 505 (1995).
12. V. M. Leonov, Preprint No. IAE-5659/6 (Kurchatov Institute of Atomic Energy, Moscow, 1993); Fiz. Plazmy **20**, 381 (1994) [Plasma Phys. Rep. **20**, 341 (1994)].
13. V. M. Leonov and A. R. Polevoj, in *Proceedings of the 15th International Conference on Plasma Physics and Controlled Nuclear Fusion Research, Seville, 1994* (Vienna: IAEA, 1996), Vol. 3, p. 315.
14. K. H. Burrell, R. J. Groebner, and DIII-D Group, Report No. GA-C20051 (General Atomics, 1990).
15. JET Team, Plasma Phys. Controlled Fusion **32**, 1083 (1990).
16. G. V. Pereverzev, P. N. Yushmanov, A. Yu. Dnestrovskij, *et al.*, Preprint No. 5358/6 (Kurchatov Institute of Atomic Energy, Moscow, 1991).
17. V. M. Leonov, in *Proceedings of Workshop on Transport Barriers at Edge and Core in Three Large Tokamak Facilities, Naka, Japan, 2000.*
18. V. M. Leonov, E. L. Romanova, and A. R. Polevoĭ, in *Proceedings of the III All-Union Conference on Diagnostics of High Temperature Plasma, Dubna, 1983*, p. 43.

Translated by N. F. Larionova

Plasma Physics Reports, Vol. 28, No. 1, 2002, pp. 12–27. From Fizika Plazmy, Vol. 28, No. 1, 2002, pp. 14–31.
Original English Text Copyright © 2002 by Mourou, Chang, Maksimchuk, Nees, Bulanov, Bychenkov, Esirkepov, Naumova, Pegoraro, Ruhl.

NONLINEAR PHENOMENA IN PLASMA

On the Design of Experiments for the Study of Relativistic Nonlinear Optics in the Limit of Single-Cycle Pulse Duration and Single-Wavelength Spot Size[1]

G. Mourou[1], Z. Chang[1], A. Maksimchuk[1], J. Nees[1], S. V. Bulanov[2], V. Yu. Bychenkov[3], T. Zh. Esirkepov[4], N. M. Naumova[2], F. Pegoraro[5], and H. Ruhl[6]

[1]*Center for Ultrafast Optical Science, University of Michigan, Ann Arbor, MI, USA*
[2]*Institute of General Physics, Russian Academy of Sciences, ul. Vavilova 38, Moscow, 119991 Russia*
[3]*Lebedev Institute of Physics, Russian Academy of Sciences, Leninskiĭ pr. 53, Moscow, 119991 Russia*
[4]*Moscow Institute for Physics and Technology, Institutskiĭ per. 9, Dolgoprudnyĭ, Moscow oblast, 141700 Russia*
[5]*University of Pisa and National Institute for Physics of Matter, Pisa, Italy*
[6]*Max Born Institute, Berlin, Germany*

Received June 18, 2001

Abstract—We propose a set of experiments with the aim of studying for the first time relativistic nonlinear optics in the fundamental limits of single-cycle pulse duration and single-wavelength spot size. The laser system that makes this work possible is now operating at the Center for Ultrafast Optical Science at the University of Michigan. Its high repetition rate (1 kHz) will make it possible to perform a detailed investigation of relativistic effects in this novel regime. This study has the potential to make the field of relativistic optics accessible to a wider community and to open the door for real-world applications of relativistic optics, such as electron/ion acceleration and neutron and positron production. *© 2002 MAIK "Nauka/Interperiodica".*

1. INTRODUCTION

Over the past 15 years, we have seen a revolution in the generation of ultraintense laser pulses [1]. Present-day lasers can produce pulses with intensities five to six orders of magnitude greater than those previously possible, giving access to new physical regimes. One of these regimes is the so-called "relativistic regime," where the quiver energy of the electrons is equal to or greater than their rest-mass energy [2].

As in the 1960s, when lasers opened up the field of bound-electron nonlinear optics [3] with the demonstration of harmonic generation, stimulated Raman and stimulated Brillouin scattering, optical Kerr effect, etc., the past decade has revealed a new class of phenomena based on the relativistic character of the electron. This relativistic behavior suggests the possibility of extending the field of laser optics from the eV to the MeV/GeV regime. Let us stress in particular the generation of X-ray and γ-ray photons [4–6], as well as the generation of energetic particle beams of electrons [7], neutrons [8], and ions [9]. A number of theoretically predicted relativistic effects, such as relativistic self-focusing [10], laser wakefield acceleration (LWFA) [11], quasistatic magnetic field generation by relativistic electron beams accelerated inside self-focusing channels [12], harmonic generation [13, 14], and nonlinear Thomson scattering [15], were also demonstrated experimentally, and MeV ions and γ-rays were used for the production of nuclear reactions [16]. Until now, all these experiments were performed with lasers delivering intensities in the relativistic regime without full control over the duration, shape, or spot size of the laser pulse.

The aim of this paper is to propose relativistic optics experiments with truly table-top lasers under highly controlled conditions. We will focus on the coherent aspects of light–matter interaction in the relativistic regime. This implies working with pulses consisting of only a few optical cycles. In order to avoid beam breakup by relativistic self-focusing, we must match the laser input numerical aperture (NA) to the channel NA. This condition requires that the beam be focused to a 1-λ diameter. Only recently have we proved experimentally that the following three basic conditions can be met simultaneously [17]: (i) relativistic intensities, (ii) pulse duration of a few optical cycles, and (iii) focused spot size of 1 μm. These conditions are satisfied by the kilohertz chirped pulse amplification (CPA) laser developed at the Center for Ultrafast Optical Science (CUOS); this laser has the advantage of being stable, compact, and relatively inexpensive.

Our experimental regime differs from and complements present studies where experiments are performed with relatively long pulses (0.1–1 ps), large spot sizes

[1] This article was submitted by the authors in English.

1063-780X/02/2801-0012$22.00 © 2002 MAIK "Nauka/Interperiodica"

(10 μm), and low repetition rates (<10 Hz). Our experiments will address electron and ion acceleration, relativistic transparency, relativistic self-focusing, coherent relativistic structures (such as solitons and vortices), coherent Thomson scattering by relativistic electrons, and neutron and positron production.

2. RELATIVISTIC EFFECTS

First of all, relativistic effects qualitatively modify the electron dynamics in the field of the electromagnetic wave. From the exact solution of the equations of motion of a charged particle in a propagating planar electromagnetic wave [18], it follows that the transverse component of the generalized momentum of an electron is constant,

$$\mathbf{p}_\perp - e\mathbf{A}_\perp/c = \text{const}, \tag{1}$$

and that the energy and the longitudinal component of the momentum are related by

$$\begin{aligned} &\gamma m_e c^2 - p_\parallel c \\ &= (m_e^2 c^4 + p_\perp^2 c^2 + p_\parallel^2 c^2)^{1/2} - p_\parallel c = \text{const}. \end{aligned} \tag{2}$$

It is convenient to express the laser field amplitude in terms of the normalized vector potential $a = eA/m_e c^2$, where A is the laser-field vector potential. The value of a can be obtained from the expression $I\lambda^2/a^2 = 1.37 \times 10^{18}$ W μm^2/cm^2, where I and λ are the laser intensity and wavelength, respectively. In the reference frame where the electron was at rest before the interaction with the laser pulse, the electron kinetic energy $K = m_e c^2(\gamma - 1)$ and momentum $\mathbf{p}$ are given by [18, 19]

$$\begin{aligned} K = m_e c^2 a_\perp^2 (x - ct)/2, \quad \mathbf{p}_\perp = m_e c \mathbf{a}_\perp (x - ct), \\ p_\parallel = m_e c a_\perp^2 (x - ct)/2. \end{aligned} \tag{3}$$

Here, $\mathbf{a}_\perp(x - ct) = e\mathbf{A}_\perp(x - ct)/m_e c^2$. We can see that, for $a > \sqrt{2}$, the electron acquires a relativistic energy and the longitudinal component of its momentum is larger than the transverse component.

For a simple plane wave ($\mathbf{A}_\perp(x - ct) = -(\mathbf{E}c/\omega)\cos(\omega t - kx)$), the force in the direction of the laser pulse propagation can be expressed as

$$F_\parallel = -(e^2/4\gamma m_e \omega^2)\frac{\partial}{\partial x}\{|\mathbf{E}|^2[1 - (2\omega t - 2kx)]\}. \tag{4}$$

This expression shows two forces: one is proportional to $\partial|\mathbf{E}|^2/\partial x$ (the ponderomotive force) and the other is spatially oscillating with a period of λ/2. In the relativistic regime, where $v \sim c$, the magnetic term in the Lorentz force $(e/c)\mathbf{v} \times \mathbf{B}$ becomes as important as the electric part, $e\mathbf{E}$, and the resulting force is directed along the propagation direction. These features are the hallmarks of relativistic nonlinear optics.

The enormous oscillating transverse field of the laser pulse acts on the electrons as a longitudinal, fully rectified field. At 10^{19} W/cm^2, this field corresponds to an equivalent electric field of 60 GV/cm. The electrons in the plasma are subjected to this large Lorentz force and are pushed forward leaving the massive ions behind. The associated charge separation produces an electrostatic field [11, 20] up to $E_{\text{break}} = m_e \omega_{\text{pe}} c\sqrt{2(\gamma_{\text{ph}} - 1)}/e$, corresponding to the Akhiezer–Polovin wave-break limit [2]. Here, $\omega_{\text{pe}} = \sqrt{4\pi n e^2/m_e}$ is the electron plasma frequency and $\gamma_{\text{ph}} = 1/\sqrt{1 - v_{\text{ph}}^2/c^2} \approx \omega/\omega_{\text{pe}}$. The accelerating field propagates at the phase velocity v_{ph}, which is equal to the group velocity $c\sqrt{1 - \omega_{\text{pe}}^2/\omega^2}$ of the driving pulse, whereas the accelerated electrons move at $v \approx c$. The maximum electron energy is determined by the accelerating field over a walk-off distance

$$l_{\text{acc}} \approx \lambda_p/2(v_{\text{ph}}/c - 1) \approx \lambda_p(\omega/\omega_{\text{pe}})^2, \tag{5}$$

which is the distance over which electrons and photons move out of phase by $\lambda_p/2 = \pi c/\omega_{\text{pe}}$. For $a > 1$, the dependence of the wakefield amplitude on the driver laser pulse amplitude should be taken into account (see [20, 21]). Electron energies as large as 100 MeV have been observed, corresponding to accelerating gradients of 2 GeV/cm [11].

The distribution of the light intensity across the beam changes the electron mass profile. In addition, the ponderomotive force of the light causes a redistribution of the electron density. These two effects change the index of refraction so that it is maximum on the axis, which leads to self-focusing. As a result, the laser beam shrinks to a single-wavelength spot size and the laser intensity increases accordingly. The threshold power for the pulse self-focusing is given by P_c [GW] = $17.3(\omega/\omega_{\text{pe}})^2$.

Relativistic self-focusing plays an important role in the production of high-energy electron beams inside the self-focusing channel. Once the electrons are accelerated, they can attract the ions behind them and provide a collimated beam of ions. Proton energies up to 30 MeV have been observed, corresponding to accelerating gradients of 60 GeV/cm [9], which is the highest acceleration gradient observed to date in the laboratory. The large ponderomotive pressure associated with self-focusing is also at the origin of the so-called "hole boring" [22] in fast ignition [23]. The use of the ions accelerated by the laser pulse in order to ignite the thermonuclear fuel provides a novel approach to the fast ignition of fusion targets [24].

Relativistic nonlinearities in a plasma interacting with ultrashort high-intensity laser pulses lead to the formation of long-lived slow-propagating coherent structures such as solitons and magnetic vortices. These structures are part of the complex nonlinear interaction between the laser pulse and the plasma and represent the basic ingredients of the long-time plasma behavior in the wake of the laser pulse.

Solitons appear in the form of stable structures where low-frequency electromagnetic radiation is trapped and, together with magnetic vortices and high-energy particles, represent an important channel of conversion of the electromagnetic pulse energy into plasma energy [25, 26]. In a homogeneous plasma, their propagation velocity is very small; however, in an inhomogeneous plasma, they are accelerated against the density gradient [27] and their electromagnetic energy can thus be extracted and detected experimentally [28].

Vortices appear in the more general context of the generation of a quasistatic magnetic field in the plasma [29]. Superstrong quasistatic magnetic fields in laser plasma have been studied extensively for many years. They are observed in laser-produced plasmas and can affect the plasma dynamics and the laser self-focusing [12].

To perform the experimental studies of relativistic nonlinear optics in the fundamental limit of single-cycle pulse duration and single-wavelength spot size, we will use the recently developed ultrashort laser technology assembled at CUOS. With this technology, the coherent interaction of ultrashort pulses with near-critical-density plasmas can be studied in the relativistic-intensity regime. The duration of a 0.8-μm laser pulse will be 5–10 fs (or 2–4 optical cycles) and the intensity will be 2×10^{18}–5×10^{19} W/cm^2, which corresponds to $a^2 \simeq 1$–25. The pulse will be focused to a single-wavelength spot size in order to match it to the relativistic channel size. The target will be made of thin metallic or C-H films 20–50 nm in thickness. The plasma density will be controlled by exciting the thin target prior to the main pulse arrival by means of a properly timed auxiliary pulse. Experiments will be done in real time (at a repetition rate of 0.3–1 kHz) in order to optimize the signal-to-noise ratio. Concerning relativistic electrons, the measurements of their energy will be carried out with a magnetic spectrometer. In order to reconstruct the ultrarelativistic electron spectrum, a nuclear activation technique can be used.

Coherent interaction of ultrashort pulses with plasmas will show (i) relativistic self-focusing, (ii) electron and ion acceleration, (iii) coherent Thomson scattering, (iv) relativistic transparency, (v) relativistic solitons, (vi) relativistic electron vortices, and (vii) electron–positron pair production.

3. THE DESIGN OF LABORATORY EXPERIMENTS FOR THE STUDY OF RELATIVISTIC NONLINEAR OPTICS

3.1. Relativistic Self-Focusing: Study of the Optimal Coupling of the Laser in the Waveguide Fundamental Mode

For our laser output equal to 1 mJ in 10 fs, corresponding to a power of 100 GW, relativistic self-focusing occurs in plasmas with densities greater than $0.17 n_{cr}$. In order to avoid the breakup of the beam into filaments, we propose matching the numerical aperture of the input optics to the numerical aperture of the relativistic channel. The plasma index of refraction inside the self-focusing channel is given by $n(r) = \sqrt{1 - \omega_{pe}^2(r)/\gamma(r)\omega^2}$ with $\gamma(r) = \sqrt{1 + a^2(r)/2}$ and $\omega_{pe}(r) = \sqrt{4\pi e^2 n(r)/m_e}$. An expansion of the refractive index $n(r) \approx 1 - \omega_{pe}^2(r)/2\gamma(r)\omega^2$ corresponds to a simple waveguide with a quadratically varying index $n(r) = n(0) - \alpha^2 r^2/2$, where $\alpha = (\omega_{pe}/\gamma)''$ near the axis. From waveguide theory, we can show that the optimum numerical aperture for the relativistic waveguide is given by $NA = \omega_{p0}/\omega$, where ω_{p0} is the plasma frequency at low intensities. For $(\omega/\omega_{p0})^2 \approx 5$, we have $NA \approx 0.4$, which corresponds to a waveguide diameter of $\approx\lambda$ or 0.8 μm. We can obtain this spot size by using an $f/1$ parabola corrected with a deformable mirror. For a given laser wavelength, the value of the channel numerical aperture determines the plasma density for the rest of the experiments.

In order to verify that this optimal coupling is indeed obtained for these ultrashort pulses when the numerical apertures are matched, we have performed two-dimensional (2D) particle-in-cell (PIC) simulations with the fully relativistic code described in [30]. In Fig. 1, we show the results of the simulations of the laser plasma matching. An underdense plasma slab with density n equal to $0.5 n_{cr}$ is located in the region $10\lambda < x < 50\lambda$. The ion-to-electron mass ratio is 1836. The incident laser pulse is linearly polarized with the magnetic field vector parallel to the z direction and the electric field in the (x, y) plane (p-polarized pulse). The laser pulse is 20 fs long with the wavelength equal to $\lambda = 0.8$ μm. It is focused at the plasma–vacuum interface located at $x = 10\lambda$. The width of the focal spot is about 1λ. Here, the laser intensity is equal to $I = 5 \times 10^{19}$ W/cm^2; i.e., $a = 4.8$. In this case, the optimal conditions for the laser–plasma matching are met. Just after the focus, the laser pulse becomes guided due to relativistic self-focusing, as is seen in Fig. 1. Here, we show the distribution of the electromagnetic energy density in the (x, y) plane at $t = 15$, 30, 45, and 60 (here and below, time is in units of the laser field period $2\pi/\omega$ and coordinates are in units of λ). At $t = 50$, the laser pulse has already lost almost all its energy. We also see the hosing of the laser pulse, which was discussed in [31, 32].

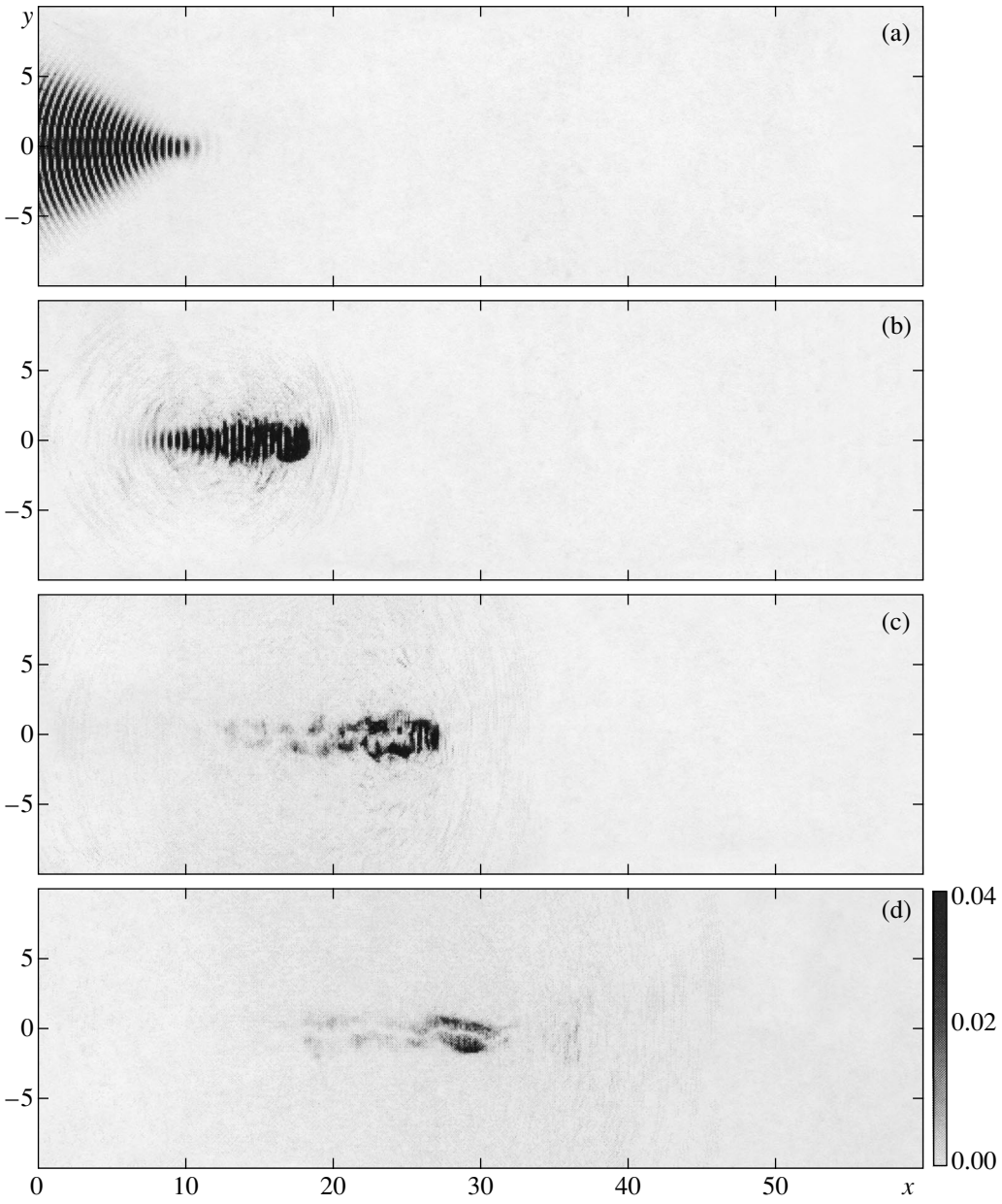

Fig. 1. Distribution of the electromagnetic energy density in the (x, y) plane at t = (a) 15, (b) 30, (c) 45, and (d) 60 for the case of the optimal matching of a high-intensity (a = 4.8) laser pulse with an underdense (n/n_{cr} = 0.5) plasma.

The ponderomotive pressure of the light forms a channel seen both in the electron and ion density distributions shown in Figs. 2a and 2b. The laser pulse accelerates the electrons predominantly in the forward direction and the ions in the transverse direction. The maximum electron energy is about 12 MeV (Fig. 2c). The ions inside the plasma are accelerated in the transverse direction due to the nonlinear ion wave breaking up to energies of about 0.5 MeV (see Fig. 2d).

A case of nonoptimal laser–plasma matching is obtained by focusing the laser pulse to 5λ inside the plasma. Just after the focus, the pulse breaks into several filaments. As a result, the laser pulse energy depletion is much faster than in the previous case. In addition, instead of a well-pronounced channel, several relatively short and wide channels appear. This nonoptimal regime of laser–plasma matching is shown in Figs. 3 and 4 for the same parameters as in Figs. 1, 2a, and 2b, except for the focal position. At approximately t = 40, the pulse has lost most of its energy.

These features, observed in PIC simulations, correlate well with observations of a laser channel produced in a gas jet. This experiment was performed with 400-fs laser pulses at λ = 1 μm. A laser beam focused to a spot

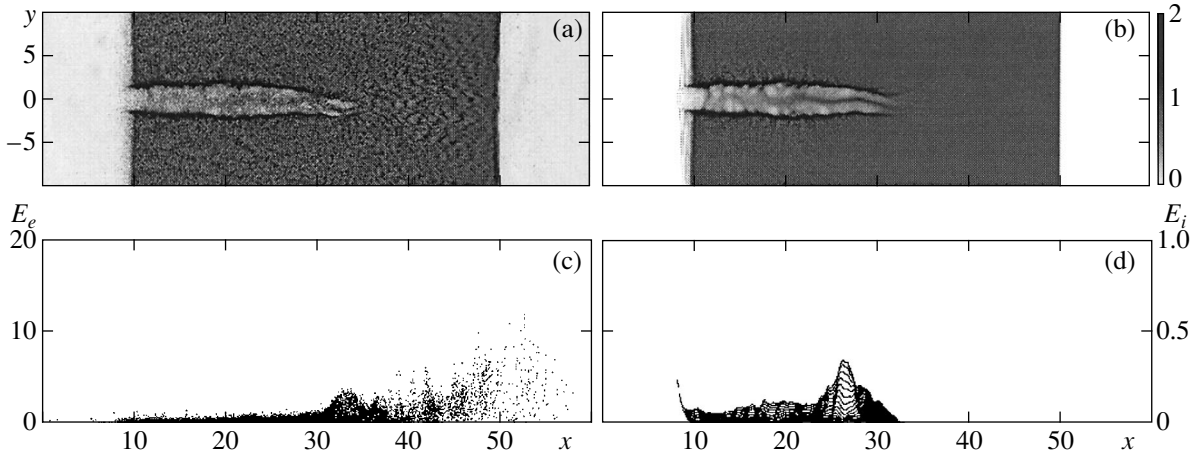

Fig. 2. Distributions of (a) the electron and (b) ion densities in the (x, y) plane and (c) electron and (d) ion kinetic energies inside the channel vs. the x coordinate at $t = 70$ for the case of the optimal matching of a high-intensity ($a = 4.8$) laser pulse with an underdense ($n/n_{cr} = 0.5$) plasma. The electron and ion densities are in units of n_{cr}, and the electron and ion energies are in units of $m_e c^2$ and $m_i c^2$, respectively.

size of about 10 μm with an $f/3.3$ parabolic mirror interacted with a He gas jet with the density $n_e \approx 0.08 n_{cr}$. The experimental setup was described in [33]. Figure 5 shows shadowgrams of a He plasma in the (a) defocusing and (b) relativistic self-focusing and self-channeling dominated regimes for a laser intensity of 6×10^{19} W/cm^2 and different distances from the nozzle top. The increase in the distance from the nozzle top corresponds to a less sharp vacuum–gas interface, which leads to a breaking of the laser–plasma matching conditions. The defocusing-dominated regime is characterized by the formation of a short on-axis channel and off-axial laser filamentation. On the other hand, the regime of relativistic self-channeling is characterized by the trapping of a significant portion of the laser beam into a long on-axial plasma channel, which extends to the end of the gas jet.

3.2. Study of Electron and Ion Acceleration

3.2.1. Electron acceleration inside the self-focusing channel. Past studies have all dealt with pulses longer than 100 fs and could not differentiate between various mechanisms for electron acceleration. It is expected that, inside the self-focusing channel, the wakefield will not have a regular structure due to the transverse inhomogeneity of the plasma density and the wakefield amplitude, which cause the transverse wave breaking [34]. Nevertheless, fast electrons are generated inside the channel, as has been seen in experiments and computer simulations. For example, PIC simulations performed in [35] seem to indicate a fairly high rate of electron acceleration in the regime when a wakefield with a regular structure is not generated. The electron acceleration under such conditions can be due to a nonlinear interplay of wakefield breaking [36], direct laser acceleration (DLA) [35, 37], betatron-resonance acceleration by the electromagnetic wave in an inhomogeneous quasistatic magnetic field generated in the self-focusing channel [38], and hosing of the laser pulse [39]. The advantage of using an ultrashort laser pulse in conjunction with a thin target was also stressed in [40], where, using PIC simulations, the electron energy scaling I (instead of $\sqrt{I}$) was shown for near-critical-density plasmas. If we respect the NA conditions found above, the light will be optimally coupled in the waveguide fundamental mode. In this channel, because of the shortness of the pulse, we expect that the first electrons will be driven by DLA, as is seen in Fig. 6, where the phase planes $(x, p_{x,e})$ and $(x, p_{y,e})$ of the electrons accelerated by the p-polarized pulse are presented. We can see electrons accelerated up to the momentum $p_{x,e} \approx 40 m_e c$, which corresponds to an energy of about 20 MeV.

The CUOS experimental arrangement will give us a unique opportunity to resolve the time structure of the electron beam with femtosecond resolution. We can manipulate the electron beam immediately after the point where it is generated by using the ponderomotive potential of a high-intensity synchronized pulse. A cross correlation between the electron pulse and the laser pulse can be obtained. This cross correlation will give us the time structure of the electron beam directly.

We conclude that, for an intensity of 5×10^{19} W/cm^2, the accelerating field can be on the order of 10 GV/cm and an electron energy of up to 20 MeV will be obtainable at a high repetition rate (1 kHz).

3.2.2. Ion acceleration during the laser pulse interaction with underdense and overdense plasmas. As was demonstrated in previous works [9], it is

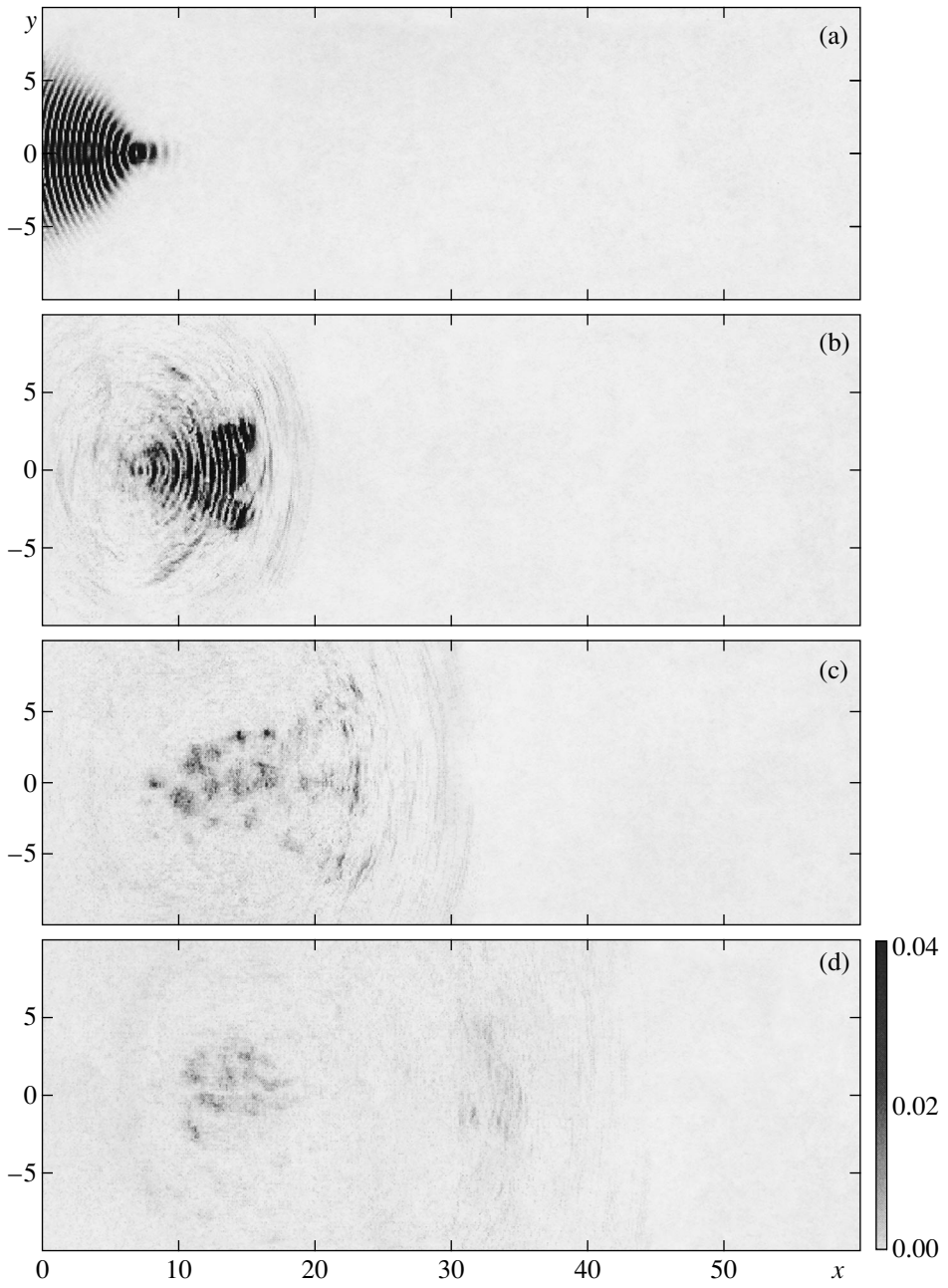

Fig. 3. Same as in Fig. 1 for nonoptimal laser–plasma matching.

expected that the charge separation between electrons and ions will in turn accelerate the ions, thus providing a collimated beam of MeV ions. The electron beam cone angle 2θ is typically given by $\tan^2\theta = 2/(\gamma - 1)$. Taking advantage of the improved signal-to-noise ratio at kilohertz repetition rates, the time-of-flight of ions will be measured across the electron beam cone. This study will be done as a function of intensity, laser polarization, plasma density, and plasma length.

In Fig. 7, we present the results of the PIC simulations of the interaction of a 20-fs *p*-polarized laser pulse ($a = 4.8$) with a slab of underdense ($n/n_{cr} = 0.5$) plasma. We can see that, at $t = 200$, the laser pulse has made a channel in the electron (Fig. 7a) and ion (Fig. 7b) densities. The fast ions are localized inside a narrow jet with a length on the order of 10 μm and a width of about 1 μm. The electric field generation and the ion beam collimation appear to be due to the self-generated magnetic field and its interaction with the plasma–vacuum

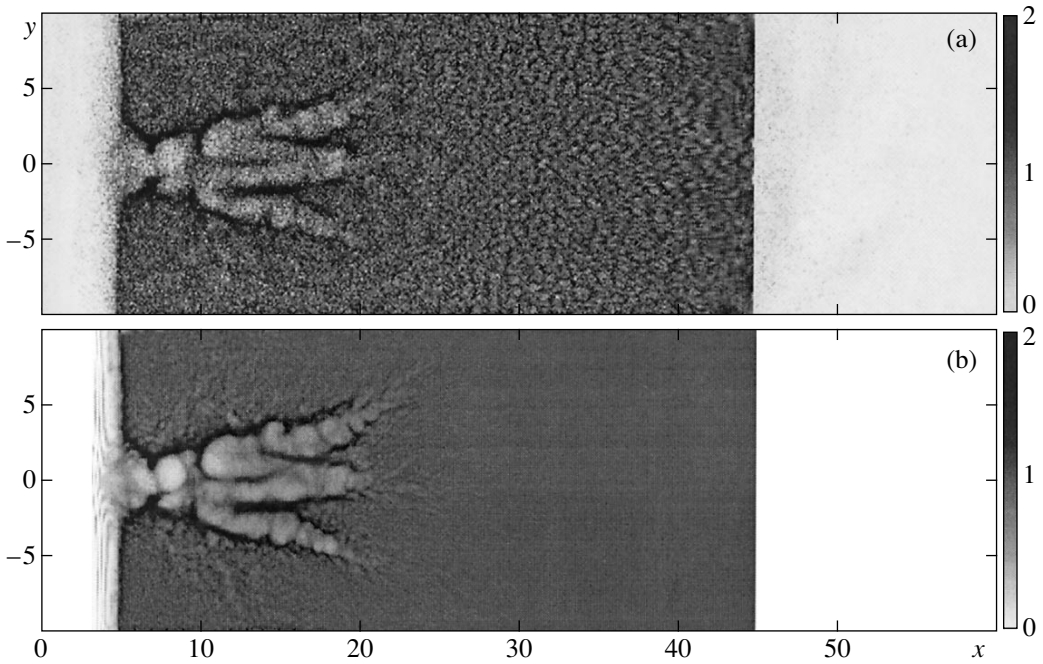

Fig. 4. Same as in Figs. 2a and 2b for nonoptimal laser–plasma matching.

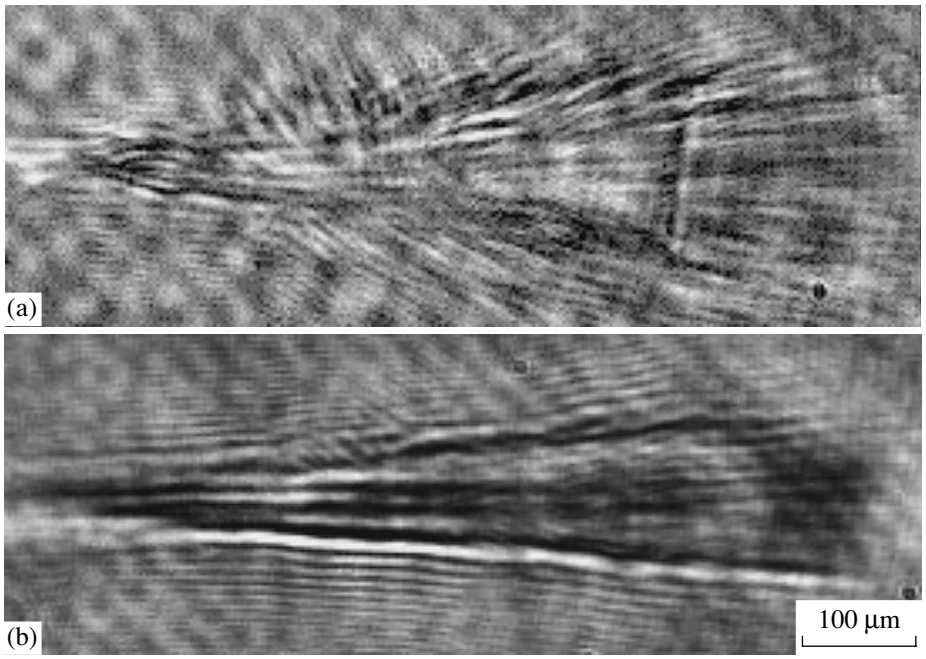

Fig. 5. Shadowgrams of laser interaction with a He jet target for a laser beam focused at a distance of (a) 1.5 and (b) 0.5 mm from the top of a supersonic gas nozzle. The probe beam is orthogonal to the pump beam and is delayed by 10 ps. The high-intensity laser beam propagates from left to right. An external plasma cone is formed due to He ionization by the spatial wings of the laser beam.

interface at the rear side of the plasma slab (see [41] for details). The x-component of the ion momentum is equal to $0.1 m_i c$, which corresponds to an ion energy of 5 MeV, and the transverse component of the ion momentum is $0.01 m_i c$. We find that the emittance of the ion beam is 10^{-4} mm rad.

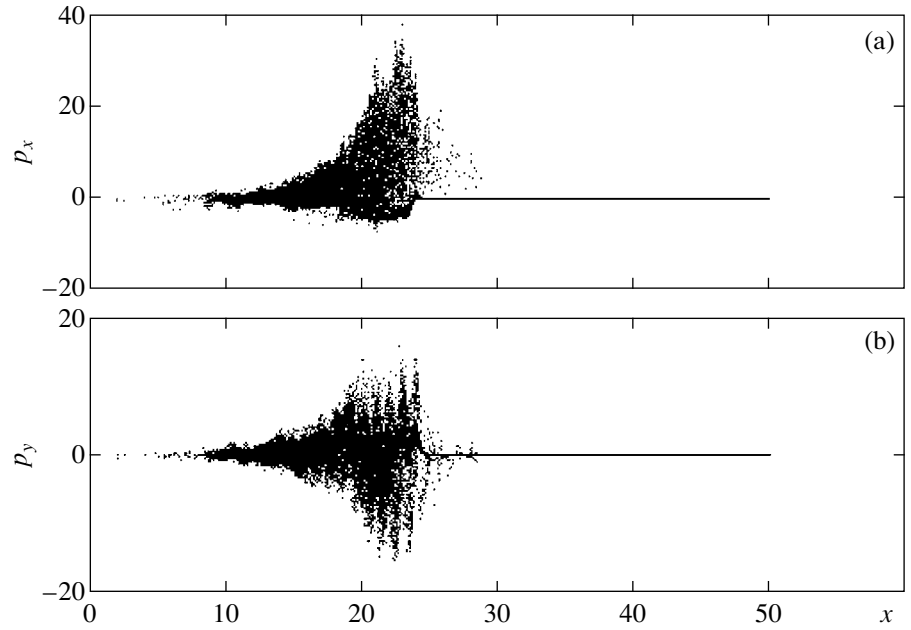

Fig. 6. Phase planes (a) $(x, p_{x,e})$ and (b) $(x, p_{y,e})$ of the electrons accelerated by a *p*-polarized pulse at $t = 40$. The electron momentum is in units of $m_e c$.

In order to simulate ion acceleration in an overdense plasma, we studied the interaction of a *p*-polarized laser pulse with an aluminum foil. The foil is assumed to be fully ionized with an ion charge number equal to 13 and atomic weight equal to 27. The foil thickness is 0.8 μm, and the foil plasma density is $n = 6.5 n_{cr}$. The foil is localized at $x = 10\lambda$ and is preceded by a 5.2-μm-long low-density plasma layer, where the density increases exponentially from zero to the critical density on the left-hand side boundary of the foil. A 20-fs-long laser pulse is focused on the foil into a spot with a diameter of 0.8 μm. At the focal spot, the pulse amplitude is $a = 6.8$, which corresponds to the intensity $I = 10^{20}$ W/cm^2. In Fig. 8, we show the distribution of the (a) electron and (b) ion densities in the (x, y) plane and (c) the ion phase plane $(x, p_{x,i})$ at $t = 200$. We see that the maximum ion energy gain is about 48 MeV.

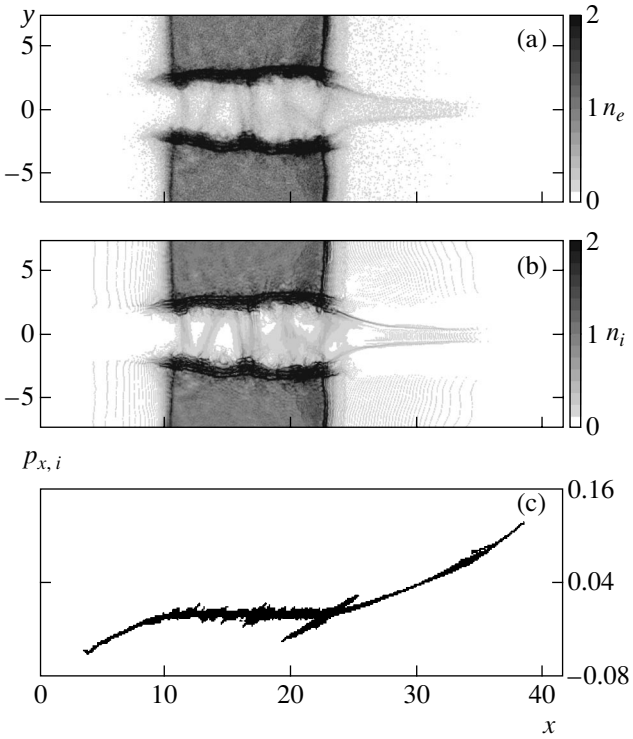

Fig. 7. Interaction of a 20-fs *p*-polarized laser pulse ($a = 4.8$) with a slab of underdense ($n/n_{cr} = 0.5$) plasma. The distributions of the (a) electron and (b) ion densities in the (x, y) plane and (c) the ion phase plane $(x, p_{x,i})$ at $t = 200$. The electron and ion densities are in units of n_{cr}, and the ion momentum is in units of $m_i c$.

3.3. Coherent Thomson Scattering

During the interaction of a relativistically intense electromagnetic wave of amplitude $a \gg 1$ with electrons, the scattered light spectrum contains high harmonics with frequencies up to ωa^3 [15]. When the laser pulse is scattered by electron bunches moving with relativistic velocities, a further frequency upshifting can appear. In this way, the scattering of an ultrashort pulse by electrons generated with γ up to 10 can be studied (at $I \simeq 5 \times 10^{19}$ W/cm^2 if we assume that γ scales as the intensity I). In the backscattering mode, an upshift is expected corresponding to $4\gamma^2\omega$ [42]. Thus, radiation

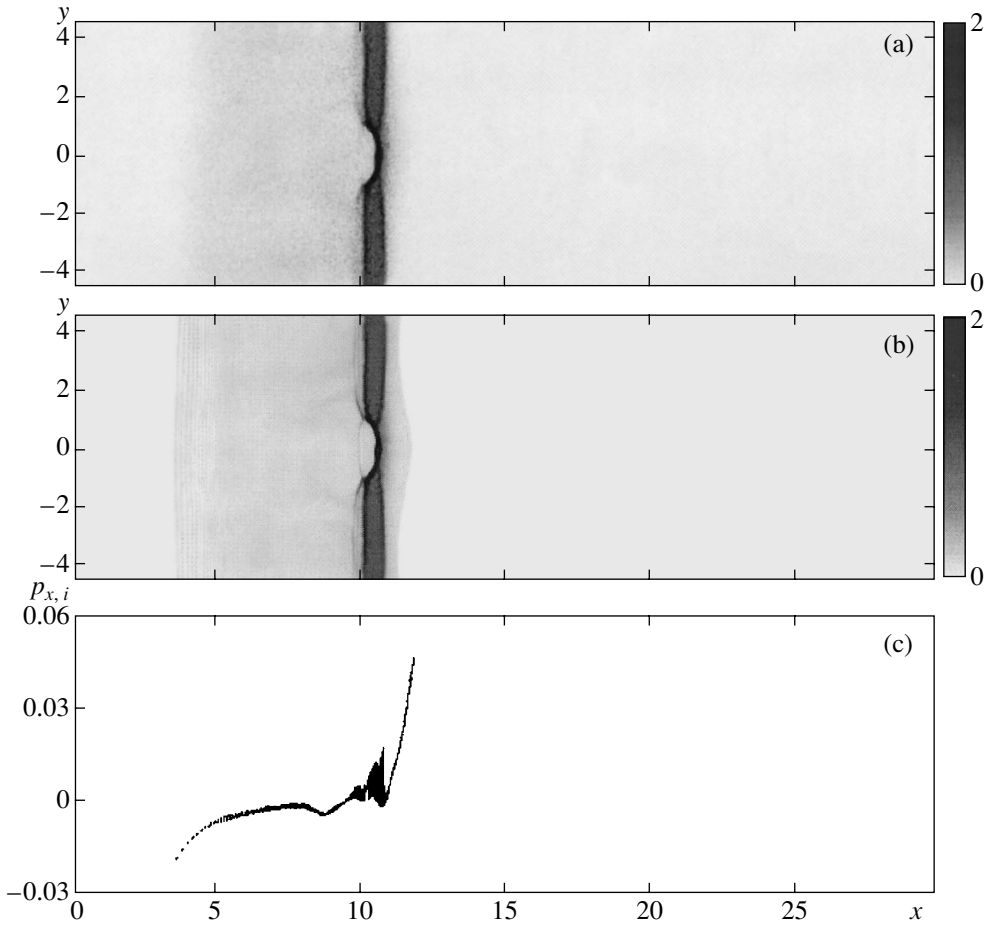

Fig. 8. Interaction of a 20-fs *p*-polarized laser pulse ($a = 6.8$) with a thin slab of overdense ($n/n_{cr} = 6.5$) plasma. The distributions of the (a) electron and (b) ion densities in the (x, y) plane and (c) the ion phase plane $(x, p_{x,i})$ at $t = 200$. The electron and ion densities are in units of n_{cr}, and the ion momentum is in units of $m_i c$.

with a wavelength down to 0.1 nm can be produced. The intensity of this radiation will be a function of the electron pulse duration. For a duration longer than the laser period (i.e., 3 fs), the scattered light will scale like N_e, whereas for pulses shorter than the light period, a coherent scattering is expected with a signal intensity scaling as N_e^2, where N_e is the electron density in the electron bunch. This possibility illustrates once more the advantage of using highly controlled pulses limited in time to a single oscillation period and focused over dimensions of a laser wavelength.

We will study the Thomson scattering of a counter-propagating laser pulse by the electron beam. Because of the small transverse size of the electron beam, the electron density will be relatively high (close to 10^{20} cm^{-3}). Probing optical pulses will be focused on the electron beam output. The spectrum of the scattered light will be studied as a function of the input light intensity and the density of the accelerated electrons.

3.4. Relativistic Transparency

Our high-repetition-rate "relativistic" laser will make possible a detailed study of the propagation of a few-cycle pulses in near-critical-density plasmas. A low-frequency wave can propagate through the plasma if the plasma electrons do not screen the electric field of the wave. The condition for wave propagation requires that the convective electric current $-env$ be smaller than the displacement current $\partial_t E/4\pi$ in the wave; i.e.,

$$en_0 v \le \frac{\omega E}{4\pi}. \tag{6}$$

In the nonrelativistic limit, we have $v \sim eE/m_e\omega$ and the transparency condition is equivalent to $\omega > \omega_{pe}$. In the ultrarelativistic limit ($a \gg 1$, $v \approx c$), we can write that the plasma becomes transparent if $\omega > \omega_{pe}/|a|^{1/2}$ [2, 43], which corresponds to the lowering of the plasma frequency. Hence, the attenuation distance will scale as $\gamma^{1/2}$. This effect significantly changes the transmission

of a thin film with a thickness comparable to the skin depth. A slab of plasma with a finite length l can screen an electric field not larger than $E = 4\pi n_e e l$. We see that, in the case of extremely thin films with thicknesses smaller than the skin depth, the relativistic transparency conditions change [14]. For relativistically strong waves with $a \gg 1$, a film is transparent if $\omega > \omega_{pe}^2 l/2ac$. This study will require a high-contrast pulse.

We will produce slightly overcritical plasmas. As in the self-focusing study, we will change the plasma density and length by varying the film thickness and the prepulse characteristics, such as delay time and intensity. Then, we will focus on studying relativistic transparency as a function of the plasma parameters (density and length) and the input pulse characteristics (intensity and polarization). The output pulse will be characterized in the spectral and time domains. The time-domain study will be done by cross correlation between the input and output pulses.

3.5. Relativistic Solitons

Solitons are a basic ingredient of electromagnetic plasma turbulence, and numerical simulations indicate that they occur in the nonlinear laser plasma interaction [26]. On the basis of the indications provided by the numerical results on soliton formation, we will concentrate on subcycle low-frequency solitons [44]. In a nonuniform plasma, the propagation of the subcycle solitons is strongly affected by the inhomogeneity of the medium. The solitons are accelerated toward the plasma–vacuum interface, where they radiate their energy away in the form of low-frequency electromagnetic bursts during their nonadiabatic interaction with the plasma boundary. These bursts can be used in order to detect subcycle solitons.

Figure 9 presents the results of the 2D PIC simulations of the laser pulse propagation in a homogeneous plasma. The laser pulse is linearly polarized with the electric field vector parallel to the z direction and the magnetic field in the (x, y) plane (s-polarized pulse).

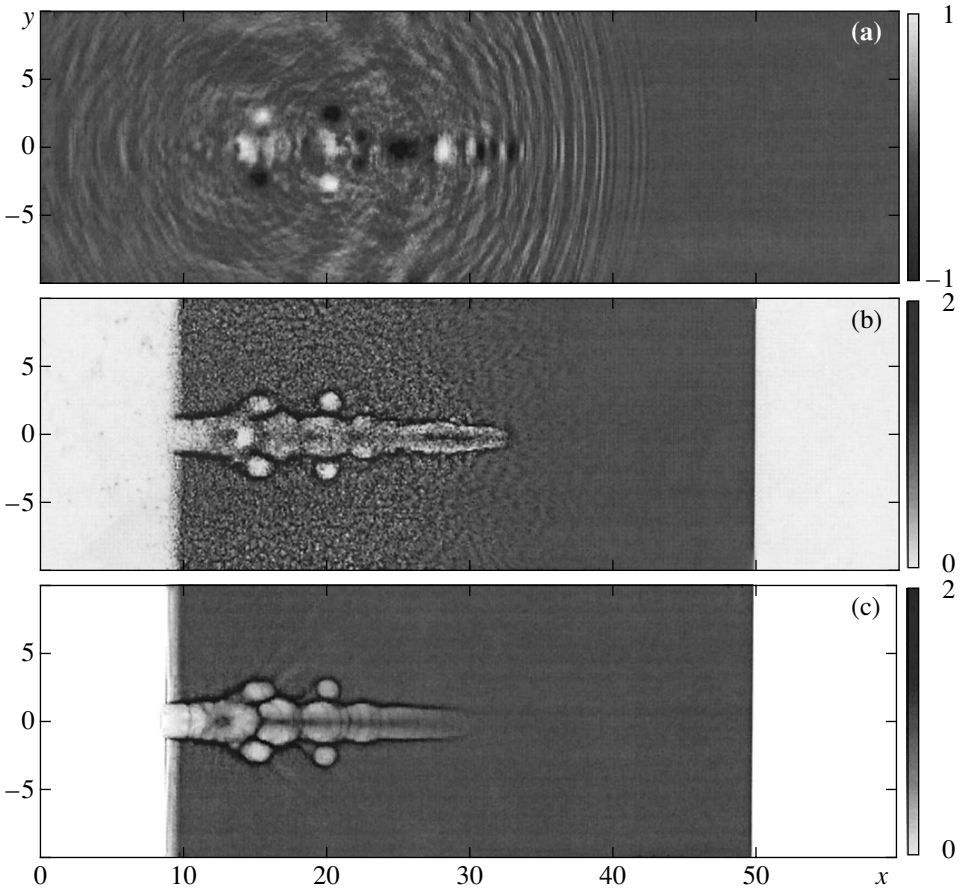

Fig. 9. Generation of solitons by an s-polarized pulse. The distributions of (a) the z-component of the electric field and the (b) electron and (c) ion densities in the (x, y) plane at $t = 55$. The electric field is in units of $m_e c\omega/e$, and the electron and ion densities are in units of n_{cr}.

The other parameters are the same as in Figs. 1 and 2. Here, we show the distributions of (a) the *z*-component of the electric field and the (b) electron and (c) ion densities in the (*x*, *y*) plane at $t = 55$. The laser pulse propagates inside the self-focusing channel with a diameter about one-half of the laser wavelength. This makes the pulse amplitude increase up to the value $a_m \approx 8$. We can see that the laser pulse leaves behind low-frequency solitons. The solitons are seen as bright spots in the electric field distribution and as bubbles in the electron and ion densities. Rigorously speaking, when the bubbles in the ion density distribution appear, these structures have lost their soliton properties and are called "postsolitons" [45, 46].

We can describe the formation of these postsolitons as follows. Since the soliton formation time is much shorter than the ion response time $t_i \approx 2\pi\sqrt{m_i/m_e}\omega_{pe}^{-1} = 2\pi\omega_{pi}^{-1}$, ions can be assumed to be at rest during the soliton formation. Inside a nonpropagating soliton (subcycle soliton [44]), the maximum electromagnetic field a_{max} and the soliton frequency ω_s are related as $a_{max} = 2\sqrt{\omega_{pe}^2 - \omega_s^2}/\omega_s$, and the soliton width is equal to $c/\sqrt{\omega_{pe}^2 - \omega_s^2}$. The ponderomotive pressure of the electromagnetic field inside the soliton is balanced by the force due to the charge-separation electric field. The amplitude of the resulting electrostatic potential is given by $\phi = \sqrt{1 + a_{max}^2}$. The ponderomotive pressure displaces the electrons outward and the Coulomb repulsion in the electrically nonneutral ion core pushes the ions away. The typical ion kinetic energy corresponds to an electrostatic potential energy on the order of $m_e c^2 a_{max}$. This process is similar to the so-called "Coulomb explosion" inside self-focusing channels (see [9]). As a result, the bubbles in the ion density distribution are formed.

3.6. Relativistic Electron Vortices

In the case of a self-focused laser pulse propagating in an underdense plasma, the fast electron beam is strongly localized in the plane perpendicular to its propagation direction. The separation between the fast electron current and the return current is expected to lead to a strongly inhomogeneous magnetic field. In a 2D model, the magnetic field is essentially dipolar; it consists of two "ribbons" of opposite polarities and vanishes at the axis of the fast electron beam. These two ribbons can be seen as the intersection of the cylindrical magnetic sheet that would be produced in a 3D configuration by a cylindrical laser pulse with the $z = 0$ plane.

A rough estimate of the magnitude of the generated magnetic field can be obtained by observing that the transverse size of the self-focusing channel is on the order of the inverse collisionless electron skin depth $d_e = c/\omega_{pe}$. Since the current density in the channel is given by $j \approx -enc$, we obtain for the generated magnetic field $eB/m_e c\omega \approx \omega_{pe}/\omega$. For a relativistic laser pulse ($a > 1$) with the wavelength 1 μm propagating in a plasma with a near-critical density, the amplitude B of the generated quasistatic magnetic field is extremely large, being on the order of 100 MG or even higher. As a consequence of the equation $\nabla \times \mathbf{B} = -4\pi en\mathbf{v}/c$, the quasistatic magnetic field in a plasma dominated by the electron dynamics is associated with electron fluid vortices with vorticity $\nabla \times \mathbf{v} = \Delta\mathbf{B}c/4\pi en$. The corresponding electron fluid motion takes the form of an antisymmetric vortex row [29]. The distance between the vortices is comparable to the collisionless skin depth. The vortex row moves as a whole in the direction of the laser pulse propagation with a velocity much smaller than the pulse group velocity.

Inside the vortex, the radial component of the force due to the magnetic pressure and the centrifugal force of the electron rotation is balanced by the force due to the charge-separation electric field [47]. Similar to the case of the postsolitons discussed above, the electrically nonneutral core pushes the ions away and accelerates them. The typical ion energy is also on the order of $m_e c^2 a$.

Two-dimensional PIC simulations of the propagation of linearly polarized laser pulses in a plasma for the same parameters as in Figs. 1–3 show the quasistatic magnetic field generated inside the self-focusing channel. In Fig. 10, we show the distribution of the *z*-component of the magnetic field in the (*x*, *y*) plane at $t = 70$ for (a) an *s*-polarized pulse and (b) a *p*-polarized pulse.

3.7. Pair Production

The kilohertz system is capable of producing intensities in the range of 10^{19} W/cm^2. At these intensities, the ponderomotive potential is higher than $2m_e c^2$. This produces conditions for the electron–positron pair generation [48]. Positrons were observed in the interaction of a relatively long and wide high-intensity laser pulse with matter [49]. Therefore, it is possible to produce (in a very controlled way) electron–positron pairs, when a single-cycle laser pulse is focused into a one-wavelength focus spot. The trident pair production has a cross section

$$\sigma_T \cong 9.6 \times 10^{-4}(\alpha r_0 Z)^2(E_\nu/2m_e c^2 - 2), \qquad (7)$$

where α is the fine structure constant, r_0 is the classical electron radius, Z is the nuclear charge number, and E_ν is the electron kinetic energy. For $\gamma = 10$ electrons and an interaction volume of 10^{-12} cm^3, we can expect to produce as many as 10^4 pair/s per one relativistic electron.

This work will depend on our success in producing electrons with $10 < \gamma < 50$. The efficiency will depend on the Z value of the target material. Positrons will also

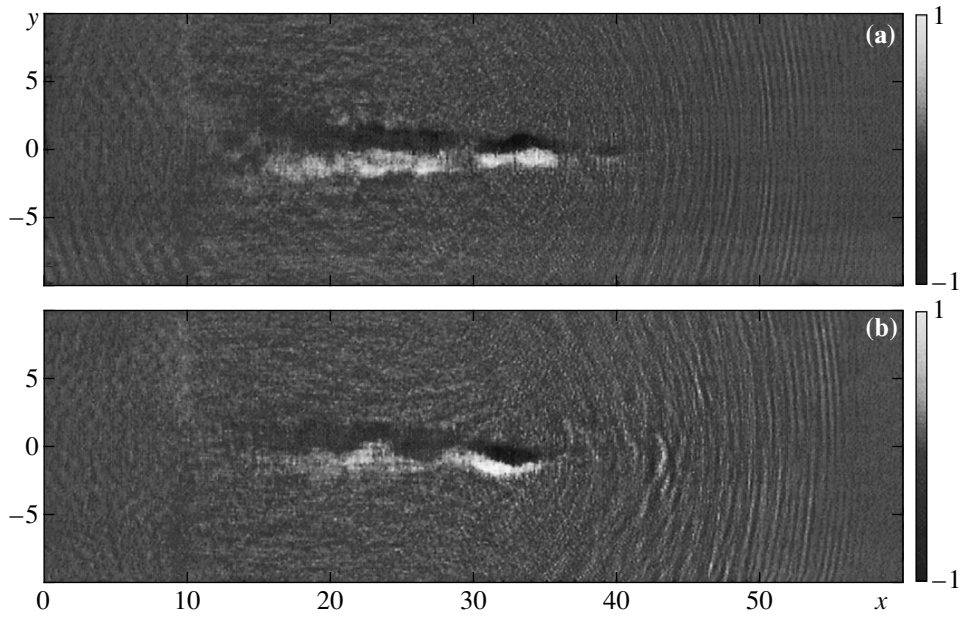

Fig. 10. Distribution of the z-component of the quasistatic magnetic field in the (x, y) plane at $t = 70$ for the cases of (a) an s-polarized pulse and (b) a p-polarized pulse. The magnetic field is in units of $m_e c\omega/e$.

be analyzed by the time-of-flight technique. Emitted γ-rays can be detected with our streak camera. Since we know precisely the instant of generation, we can accumulate the signal by using the streak camera in the jitter-free mode to time-resolve the generation processes on the subpicosecond time scale.

4. EXPERIMENTAL SETUP

4.1. The Ultrashort-Pulse Laser

The experimental study will be carried out using the Ultrafast Photon Source (UPS) Laser Facility at CUOS. The UPS is a high-repetition-rate 0.8-μm Ti : sapphire laser based on the chirped pulse amplification (CPA) design. It is the most powerful sub-10-fs laser and the first kilohertz laser that can produce relativistic intensities.

The following are the features of this laser that make it ideal for the proposed relativistic nonlinear optics studies:

Sub-10-fs pulse. The UPS laser produces 21-fs 3-mJ pulses directly. By using a hollow-core fiber and chirped mirror technique, these pulses are compressed to 8 fs with ≈1 mJ energy. The measured pulse duration is shown in Fig. 11. Work is in progress to obtain 6-fs 1-mJ pulses by optimizing the compression.

Relativistic intensity. The laser can produce focused intensities above 10^{18} W/cm^2 with both 21-fs and sub-10-fs pulses. The intensity was determined by measuring the focal spot size, pulse duration, and pulse energy. In the case of 21-fs pulses, an intensity of $>5 \times 10^{18}$ W/cm^2 was confirmed by the observation of charge states up to Ar^{13+} [50]. We believe that sub-10-fs 1-mJ pulses will be focused to intensities above 10^{19} W/cm^2 in the near future.

Wavelength scale focal spot. In order to generate intensities greater than 10^{18} W/cm^2, an $f/1$ paraboloid is used to focus the beam. A deformable mirror is used to correct the wave-front distortion from the laser system and to precompensate the aberration caused by the focusing optics. Figure 12 shows the image and line graph of the focal spot. The FWHM spot size is 1.6 μm, and 78% of the total energy is inside the $1/e^2$ radius. The actual spot size will be much smaller than that

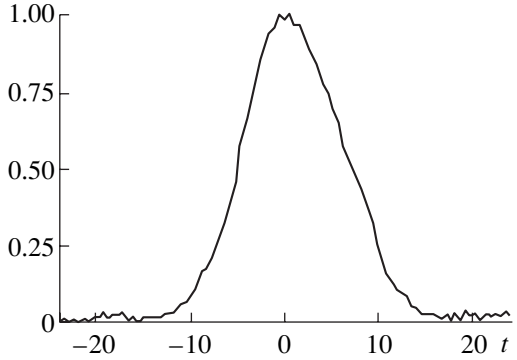

Fig. 11. Autocorrelation trace of the 8-fs pulse.

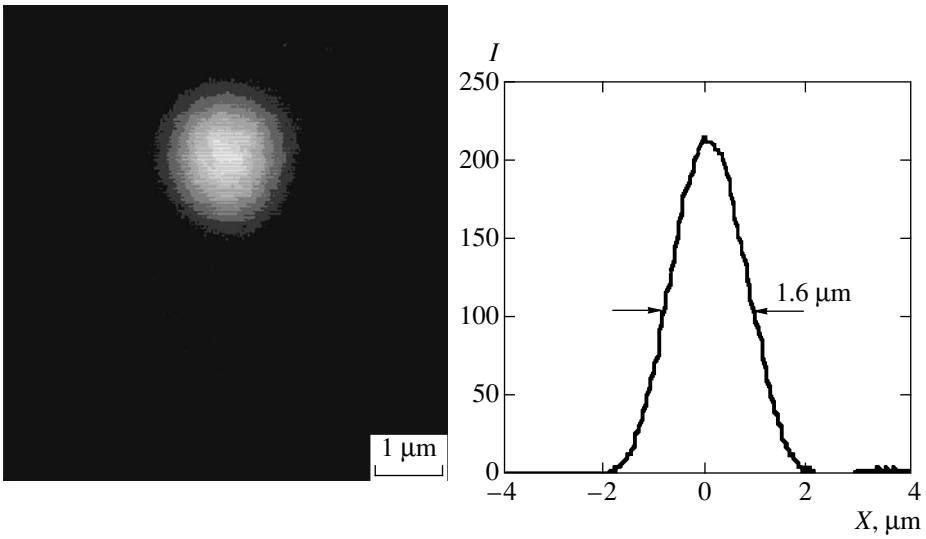

Fig. 12. The image and line graph of a near-diffraction-limited focal spot with a diameter of 1.6 μm.

shown. The difference is due to aberrations arising in the microscope objective used in our imaging system. The focal spot will match the NA of a relativistic channel, thus favoring the formation of single stable filament.

Marechal's criterion guarantees losses at the focus of less than 20% provided that the rms wave-front error is less than 1/14. The most efficient way to deliver this wave-front quality is to use a deformable mirror coupled to a wave-front measurement system or a focal intensity feedback loop. While several wave-front measurement systems are available, none offers measurements with a numerical aperture of 0.4 corresponding to *f*/1 optics. Consequently, we will utilize a genetic algorithm with feedback from the second harmonic generation or from the ionization threshold in gas as a means of optimizing the focal intensity in our laser system.

Using such a system, we have demonstrated the relativistic intensity generation from 21-fs pulses and the potential to focus 8-fs pulses to relativistic intensities. In the course of obtaining these results, we have noted that the laser system maintains sufficient stability so that we rarely have to reoptimize the deformable mirror settings.

In addition to the advantages of obtaining a small focal spot and high focal intensity, the deformable mirror also significantly decreases stray light that might cause damage to areas of the target not under investigation.

4.2. The Target

In order to delve into the realm of relativistic nonlinearity under the new conditions of high stability, high NA, and a high repetition rate, it will be necessary to use a target that can be replenished within a millisecond. With low-repetition-rate systems, there is no problem in delivering pulses with intensities of 10^{18}–10^{20} W/cm^2 to targets of gases, clusters, liquids, or solids. The long time between shots allows plenty of time for target manipulation. At a 1-kHz repetition rate, however, only experiments involving gas and cluster targets have been performed to date. In order to work with near-critical-density plasmas, we propose to manipulate solid thin-film targets to obtain a new specimen for each laser shot. This can only be done without damaging neighboring material because the pulse energy of the 1-kHz laser is in the 1-mJ range.

By using adaptive optics, we will generate a 1-μm focal spot with a Gaussian profile. This will be directed toward a target film 10–100 nm in thickness mounted on a support grid. As the experiment continues, the target will be moved to bring new material into place for the next shot. Commercial grids 2 mm in diameter with square patterns of 12.5-μm period are available. The 5-μm Ni grid bars can absorb 150 μJ of energy without melting and 4.7 mJ before vaporizing. With the precise focus previously discussed, it will be possible to avoid direct absorption of the laser radiation outside the 7.5 μm clear aperture of these cells. Then, with the greatest portion of the laser energy being directed to the target film, the anticipation is that the outermost perimeter of each cell will not melt and resolidification of any melted grid material will occur due to radiation cooling. Thus, proceeding at a 1-kHz rate, the 20000 cells of a target grid will last 20 s. A new grid will be moved into place while background calibrations are carried out. This increase from single-shot to 20000-shot measurements will have the effect of increasing signal-to-noise by a factor of 150.

Rapid registration of the target grid will be accomplished by using a video feedback from a full aperture alignment laser transmitted through the target and from a reduced aperture alignment laser monitoring diffraction from the grid. Once a target grid is registered, it will be scanned throughout its aperture.

5. SUMMARY

It is only in the last decade that we have been able to produce laser intensities in the relativistic regime. This capability has placed us at the threshold of a fundamentally new regime in nonlinear optics that could be as fruitful as conventional bound-electron nonlinear optics. A host of novel effects have been demonstrated: the generation of X-ray and γ-ray pulses, the production of high-energy electron and ion beams, the generation of higher harmonics from solids, relativistic self-focusing, nonlinear Thomson scattering, etc. The lasers involved in these studies, although more compact than their predecessors, are still very large and expensive, with energies on the joule level, repetition rates from 0.01 to 10 Hz, and a pulse duration of ≈100 fs. Owing to progress in short-pulse generation and the application of deformable mirrors for beam focusing, we have recently shown that it is possible to produce relativistic intensities ($I > 10^{18}$ W/cm^2) at a 1-kHz repetition rate. The laser pulse energy is in the millijoule range, with sub-ten-femtosecond duration, i.e., in the single-cycle regime. It has a one-wavelength focal spot size. This system is truly table-top and makes the study of laser–matter interaction in a new regime possible. The advantages of operating in this new regime are the following. First, the ultrashort time scale of a few optical cycles will favor a coherent laser–matter interaction. It is expected that electron acceleration in this regime will be proportional to the laser intensity rather than the square root of the intensity. Second, the very small spot size, limited by the laser wavelength, will provide a natural cut-off for spatial instabilities that dominate with larger spot sizes. We, therefore, expect, much like in a single-mode fiber, clean propagation in the plasma and an optimum coupling between the laser beam and the relativistic filament. Third, because of the high repetition rate and enhanced signal-to-noise ratio, we will be able to perform a precise study of laser–matter interaction in this regime. This proposal will concentrate particularly on relativistic self-focusing, relativistic transparency, laser acceleration by optical rectification in plasma (direct laser acceleration), coherent Thomson scattering from accelerated electrons, relativistic solitary waves, relativistic electron vortices associated with the quasistatic magnetic field generation, and positron generation.

To perform this study, we will use the recently developed ultrashort laser technology, assembled at CUOS. Specifically, we will employ compressed millijoule pulses of a few cycles in conjunction with deformable mirrors to reach spot sizes of one micron [17, 51] to develop an accurate understanding of relativistic nonlinear optics. We aim to demonstrate that relativistic nonlinear optics experiments can be carried out with a true table-top laser system, which will provide an inherently superior signal-to-noise ratio.

ACKNOWLEDGMENTS

This work was supported in part by the USA National Science Foundation through CUOS (contract no. STS PHY8920108) and by the Russian Foundation for Basic Research (project nos. 99-02-16997 and 00-02-16063).

REFERENCES

1. M. D. Perry and G. Mourou, Science **64**, 917 (1994); G. A. Mourou, C. P. J. Barty, and M. D. Perry, Phys. Today **51**, 22 (1998); S. Backus, C. G. Durfee III, M. M. Murnane, and H. C. Kapteyn, Rev. Sci. Instrum. **69**, 1207 (1998).
2. A. I. Akhiezer and R. V. Polovin, Zh. Éksp. Teor. Fiz. **30**, 915 (1956) [Sov. Phys. JETP **3**, 696 (1956)].
3. S. A. Akhmanov and R. V. Khokhlov, *Nonlinear Optics* (VINITI, Moscow, 1965; Gordon and Breach, New York, 1972); N. Bloembergen, *Nonlinear Optics: a Lecture Note and Reprint Volume* (W. A. Benjamin, New York, 1965; Mir, Moscow, 1966); Y. R. Shen, *The Principles of Nonlinear Optics* (Wiley, New York, 1984; Nauka, Moscow, 1989); R. W. Boyd, *Nonlinear Optics* (Academic, San Diego, 1992).
4. J. C. Kieffer, J. P. Matte, H. Pepin, *et al.*, Phys. Rev. Lett. **68**, 480 (1992).
5. J. D. Kmetec, C. L. Gordon III, J. J. Macklin, *et al.*, Phys. Rev. Lett. **68**, 1527 (1992).
6. F. Beg, A. R. Bell, A. E. Dangor, *et al.*, Phys. Plasmas **4**, 447 (1997); P. Norreys, M. Santala, E. Clark, *et al.*, Phys. Plasmas **6**, 2150 (1999).
7. C. E. Clayton, K. A. Marsh, A. Dyson, *et al.*, Phys. Rev. Lett. **70**, 37 (1993); K. Nakajima, D. Fisher, T. Kawakubo, *et al.*, Phys. Rev. Lett. **74**, 4428 (1995); A. Modena, Z. Najimudin, A. E. Dangor, *et al.*, Nature **337**, 606 (1995); D. Umstadter, S.-Y. Chen, A. Maksimchuk, *et al.*, Science **273**, 472 (1996); R. Wagner, S.-Y. Chen, A. Maksimchuk, and D. Umstadter, Phys. Rev. Lett. **78**, 3125 (1997); D. Gordon, K. C. Tzeng, C. E. Clayton, *et al.*, Phys. Rev. Lett. **80**, 2133 (1998); S.-Y. Chen, M. Krishnan, A. Maksimchuk, *et al.*, Phys. Plasmas **6**, 4739 (1999).
8. G. Pretzler, A. Saemann, A. Pukhov, *et al.*, Phys. Rev. E **58**, 1165 (1998); L. Disdier, J. P. Garconnet, G. Malka, and J. L. Miquel, Phys. Rev. Lett. **82**, 1454 (1999).
9. G. S. Sarkisov, V. Yu. Bychenkov, V. T. Tikhonchuk, *et al.*, Pis'ma Zh. Éksp. Teor. Fiz. **66**, 787 (1997) [JETP Lett. **66**, 828 (1997)]; A. G. Zhidkov, A. Sasaki, T. Tajima, *et al.*, Phys. Rev. E **60**, 3273 (1999); T. Zh. Esirkepov, Y. Sentoku, K. Mima, *et al.*, Pis'ma Zh. Éksp. Teor. Fiz. **70**, 80 (1999) [JETP Lett. **70**, 82 (1999)]; S. V. Bulanov, N. M. Naumova, T. Zh. Esirkepov, *et al.*, Pis'ma Zh. Éksp. Teor. Fiz. **71**, 593 (2000) [JETP Lett. **71**, 407 (2000)]; A. Maksimchuk, S. Gu, K. Flippo, *et al.*, Phys. Rev. Lett. **84**, 4108 (2000);

E. L. Clark, K. Krushelnick, M. Zepf, *et al.*, Phys. Rev. Lett. **85**, 1654 (2000); Y. Sentoku, T. V. Lisseikina, T. Zh. Esirkepov, *et al.*, Phys. Rev. E **62**, 7271 (2000); S. Wilks, A. B. Langdon, T. E. Cowan, *et al.*, Phys. Plasmas **8**, 542 (2001).

10. A. G. Litvak, Zh. Éksp. Teor. Fiz. **57**, 629 (1969) [Sov. Phys. JETP **30**, 344 (1969)]; C. Max, J. Arons, and A. B. Langdon, Phys. Rev. Lett. **33**, 209 (1974); G. Schmidt and W. Horton, Comm. Plasma Phys. Controlled Fusion **9**, 85 (1985); P. Sprangle, C. M. Tang, and E. Esarey, IEEE Trans. Plasma Sci. **PS-15**, 145 (1987); A. B. Borisov, A. V. Borovskiy, O. B. Shiryaev, *et al.*, Phys. Rev. A **45**, 5830 (1992); P. Gibbon, P. Monot, T. August, *et al.*, Phys. Plasmas **2**, 1305 (1995); S. V. Bulanov, F. Pegoraro, and A. M. Pukhov, Phys. Rev. Lett. **74**, 710 (1995); J. Fuchs, Phys. Rev. Lett. **80**, 1658 (1998); S.-Y. Chen, G. S. Sarkisov, A. Maksimchuk, *et al.*, Phys. Rev. Lett. **80**, 2610 (1998).
11. T. Tajima and J. M. Dawson, Phys. Rev. Lett. **43**, 267 (1979); E. Esarey, P. Sprangle, J. Krall, and A. Ting, IEEE Trans. Plasma Sci. **24**, 252 (1996).
12. D. W. Forslund, J. M. Kindel, W. B. Mori, *et al.*, Phys. Rev. Lett. **54**, 558 (1985); G. A. Askar'yan, S. V. Bulanov, F. Pegoraro, and A. M. Pukhov, Pis'ma Zh. Éksp. Teor. Fiz. **60**, 240 (1994) [JETP Lett. **60**, 251 (1994)]; A. M. Pukhov and J. Meyer-ter-Vehn, Phys. Rev. Lett. **76**, 3975 (1996); M. Borghesi, A. J. Mackinnon, R. Gaillard, *et al.*, Phys. Rev. Lett. **80**, 5137 (1998).
13. S. V. Bulanov, N. M. Naumova, and F. Pegoraro, Phys. Plasmas **1**, 745 (1994); R. Lichters, J. Meyer-ter-Vehn, and A. M. Pukhov, Phys. Plasmas **3**, 3425 (1996); D. von der Linde, AIP Conf. Proc. **426**, 221 (1998); M. Zepf, G. D. Tsakiris, G. Pretzler, *et al.*, Phys. Rev. E **58**, R5253 (1998).
14. A. V. Vshivkov, N. M. Naumova, F. Pegoraro, and S. V. Bulanov, Phys. Plasmas **5**, 2727 (1998).
15. E. S. Sarachik and G. T. Schappert, Phys. Rev. D **1**, 2738 (1970); S.-Y. Chen, A. Maksimchuk, and D. Umstadter, Nature **396**, 653 (1998); S.-Y. Chen, A. Maksimchuk, E. Esarey, and D. Umstadter, Phys. Rev. Lett. **84**, 5528 (2000).
16. K. Nemoto, A. Maksimchuk, S. Banerjee, *et al.*, Appl. Phys. Lett. **78**, 595 (2001); K. W. Ledingham, I. Spencer, T. McCanny, *et al.*, Phys. Rev. Lett. **84**, 899 (2000); T. E. Cowan, A. W. Hunt, T. W. Phillips, *et al.*, Phys. Rev. Lett. **84**, 903 (2000).
17. O. Albert, H. Wang, D. Liu, *et al.*, Opt. Lett. **25**, 1125 (2000).
18. L. D. Landau and E. M. Lifshitz, *The Classical Theory of Fields* (Nauka, Moscow, 1973; Pergamon, Oxford, 1975).
19. H. M. Lai, Phys. Fluids **23**, 2373 (1980); B. Rau, T. Tajima, and H. Hojo, Phys. Rev. Lett. **78**, 3310 (1997).
20. S. V. Bulanov, V. I. Kirsanov, and A. S. Sakharov, Pis'ma Zh. Éksp. Teor. Fiz. **50**, 176 (1989) [JETP Lett. **50**, 198 (1989)]; V. I. Berezhiani and I. G. Murusidze, Phys. Lett. A **148**, 338 (1990).
21. S. V. Bulanov, F. Califano, G. I. Dudnikova, *et al.*, in *Reviews of Plasma Physics*, Ed. by V. D. Shafranov (Kluwer, New York, 2001), Vol. 22, p. 227.
22. W. Kruer and S. C. Wilks, Plasma Phys. Controlled Fusion **34**, 2061 (1992); S. C. Wilks, W. L. Kruer, M. Tabak, and A. B. Langdon, Phys. Rev. Lett. **69**, 1383 (1992).
23. M. Tabak, J. Hammer, M. E. Glinsky, *et al.*, Phys. Plasmas **1**, 1626 (1994).
24. M. Roth, T. E. Cowan, M. H. Key, *et al.*, Phys. Rev. Lett. **86**, 436 (2001); H. Ruhl, S. V. Bulanov, T. E. Cowan, *et al.*, Fiz. Plazmy **27**, 387 (2001) [Plasma Phys. Rep. **27**, 363 (2001)]; V. Yu. Bychenkov, V. Rozmus, A. Maksimchuk, *et al.*, Fiz. Plazmy **27**, 1076 (2001) [Plasma Phys. Rep. **27**, 1017 (2001)].
25. V. A. Kozlov, A. G. Litvak, and E. V. Suvorov, Zh. Éksp. Teor. Fiz. **76**, 148 (1979) [Sov. Phys. JETP **49**, 75 (1979)]; P. K. Kaw, A. Sen, and T. Katsouleas, Phys. Rev. Lett. **68**, 3172 (1992); D. Farina and S. V. Bulanov, Phys. Rev. Lett. **86**, 5289 (2001); Fiz. Plazmy **27**, 680 (2001) [Plasma Phys. Rep. **27**, 641 (2001)].
26. S. V. Bulanov, I. N. Inovenkov, V. I. Kirsanov, *et al.*, Phys. Fluids B **4**, 1935 (1992); S. V. Bulanov, T. Zh. Esirkepov, N. M. Naumova, *et al.*, Phys. Rev. Lett. **82**, 3440 (1999).
27. H. Chen and C. Liu, Phys. Rev. Lett. **37**, 693 (1976).
28. Y. Sentoku, T. Zh. Esirkepov, K. Mima, *et al.*, Phys. Rev. Lett. **83**, 3434 (1999).
29. S. V. Bulanov, M. Lontano, T. Zh. Esirkepov, *et al.*, Phys. Rev. Lett. **76**, 3562 (1996); S. V. Bulanov, T. Zh. Esirkepov, M. Lontano, and F. Pegoraro, Fiz. Plazmy **23**, 715 (1997) [Plasma Phys. Rep. **23**, 660 (1997)].
30. T. Zh. Esirkepov, Comput. Phys. Commun. **135**, 144 (2001).
31. G. Shvets and J. S. Wurtele, Phys. Rev. Lett. **73**, 3540 (1994); P. Sprangle, J. Krall, and E. Esarey, Phys. Rev. Lett. **73**, 3544 (1994); A. G. Litvak, V. A. Mironov, and E. M. Sher, Phys. Rev. E **55**, 7441 (1997); B. J. Duda, R. G. Hemker, K. C. Tzeng, and W. B. Mori, Phys. Rev. Lett. **83**, 1978 (1999); B. J. Duda and W. B. Mori, Phys. Rev. E **61**, 1925 (2000).
32. N. M. Naumova, J. Koga, K. Nakajima, *et al.*, Phys. Plasmas **8**, 4149 (2001).
33. G. Sarkisov, V. Yu. Bychenkov, V. N. Novikov, *et al.*, Phys. Rev. E **59**, 7042 (1999).
34. S. V. Bulanov, F. Pegoraro, A. M. Pukhov, and A. S. Sakharov, Phys. Rev. Lett. **78**, 4205 (1997).
35. C. Gahn, G. D. Tsakiris, A. Pukhov, *et al.*, Phys. Rev. Lett. **83**, 4772 (1999).
36. S. V. Bulanov, V. I. Kirsanov, and A. S. Sakharov, Pis'ma Zh. Éksp. Teor. Fiz. **53**, 540 (1991) [JETP Lett. **53**, 565 (1991)]; M. Raoul, M. Trins, V. Goloviznin, *et al.*, Phys. Rev. E **63**, 26 406 (2001).
37. J. Meyer-ter-Vehn, Z. M. Sheng, and A. M. Pukhov, Phys. Plasmas **6**, 2847 (1999).
38. A. M. Pukhov and J. Meyer-ter-Vehn, Phys. Plasmas **5**, 1880 (1998).
39. K.-C. Tseng, W. B. Mori, and T. Katsouleas, Phys. Plasmas **6**, 2105 (1999).
40. Wei Yu, V. Bychenkov, Y. Sentoku, *et al.*, Phys. Rev. Lett. **85**, 570 (2000).
41. A. V. Kuznetsov, T. Zh. Esirkepov, F. F. Kamenets, and S. V. Bulanov, Fiz. Plazmy **27**, 225 (2001) [Plasma Phys. Rep. **27**, 211 (2001)].

42. P. Sprangle, A. Ting, E. Esarey, and A. Fisher, J. Appl. Phys. **72**, 5032 (1992); E. Esarey, S. K. Ride, and P. Sprangle, Phys. Rev. E **48**, 3003 (1993).
43. K. Nagashima, Y. Kishimoto, and H. Takuma, Phys. Rev. E **1**, 2738 (1970); J. Denavit, Phys. Rev. Lett. **69**, 3052 (1992); A. Giulietti, A. Barbini, P. Chessa, *et al.*, Phys. Rev. Lett. **79**, 3194 (1997).
44. T. Zh. Esirkepov, F. F. Kamenets, S. V. Bulanov, and N. M. Naumova, Pis'ma Zh. Éksp. Teor. Fiz. **68**, 33 (1998) [JETP Lett. **68**, 36 (1998)].
45. N. M. Naumova, S. V. Bulanov, T. Zh. Esirkepov, *et al.*, Phys. Rev. Lett. **87**, 185004 (2001).
46. H. Ruhl, M. Borghesi, S. V. Bulanov, *et al.*, submitted to Phys. Rev. Lett.
47. A. V. Gordeev and T. V. Loseva, Pis'ma Zh. Éksp. Teor. Fiz. **70**, 669 (1999) [JETP Lett. **70**, 684 (1999)].
48. J. W. Shearer, J. Garrison, J. Wong, and J. E. Swain, Phys. Rev. A **8**, 1582 (1973); E. P. Liang, S. C. Wilks, and M. Tabak, Phys. Rev. Lett. **81**, 4887 (1998).
49. C. Gahn, G. D. Tsakiris, G. Pretzler, *et al.*, Appl. Phys. Lett. **77**, 2662 (2000).
50. D.-F. Liu, J. Nees, H.-W. Wang, *et al.*, in *Proceedings of the Conference on Lasers and Electro-Optics, San Francisco, 2000*, Paper CPD-5.
51. J. Queneuille, F. Druon, A. Maksimchuk, *et al.*, Opt. Lett. **25**, 508 (2000).

Plasma Physics Reports, Vol. 28, No. 1, 2002, pp. 28–39. Translated from Fizika Plazmy, Vol. 28, No. 1, 2002, pp. 32–44.
Original Russian Text Copyright © 2002 by Pal', Sivokhin, Starostin, Filippov, Fortov.

DUSTY PLASMA

Potential of a Dust Grain in a Nitrogen Plasma with a Condensed Disperse Phase at Room and Cryogenic Temperatures

A. F. Pal'*, D. V. Sivokhin*, A. N. Starostin*, A. V. Filippov*, and V. E. Fortov**

**Troitsk Institute for Innovation and Fusion Research, Troitsk, Moscow oblast, 142190 Russia*

***Institute for High Energy Densities, Associated Institute for High Temperatures, Russian Academy of Sciences, Izhorskaya ul. 13/19, Moscow, 127412 Russia*

e-mail: fav@triniti.ru

Received June 22, 2001

Abstract—The first numerical study is presented of the self-consistent potential of a dust grain in a nitrogen plasma with a condensed disperse phase at room and cryogenic temperatures and at high gas pressures for which the electron and ion transport in the plasma can be described in the hydrodynamic approximation. It is shown that the potential of the dust grain is described with good accuracy by the Debye potential, in which case, however, the screening radius turns out to be larger than the electron Debye radius. The difference between the radii is especially large in a plasma with high ionization rates (about 10^{16}–10^{18} cm^{-3} s^{-1}) at room temperature. It is found that, in a certain range of the parameters of a nitrogen dusty plasma, the parameter describing the interaction between the grains exceeds the critical value above which one would expect the formation of plasma–dust structures such as Coulomb crystals. For a plasma at cryogenic temperature (T = 77 K), this range is significantly wider. *© 2002 MAIK "Nauka/Interperiodica".*

1. INTRODUCTION

Over the past decade, the problems related to a dusty (or aerosol or complex) plasma or a plasma with a condensed disperse phase (CDP) have attracted increased interest in the context of fundamental physics and purely technological applications [1, 2]. Numerical calculations of a non-self-sustained discharge (an NSSD) in nitrogen with a CDP at atmospheric pressure were reported in paper [3], which was aimed at simulating dust grain charging in a nitrogen dusty plasma. The results obtained in [3] showed that the grains may acquire a significant negative electric charge. Paper [3] also reported preliminary results from the investigation of the formation of ordered plasma–dust structures in an NSSD in nitrogen with a CDP. At present, the methods of molecular dynamics are applied to simulate gas–liquid–solid-state phase transitions in systems of particles whose interactions are described by different potentials: the Coulomb potential [4, 5]; the Lennard-Jones potential [4–6]; the potential that depends on the interparticle distance according to a power law [4, 5]; and the Debye screening potential, which is also called the Yukawa potential [7–12]. The simulations show that the conditions for phase transitions depend sensitively on the shape of the interaction potential. Thus, the phase state of a system with the Coulomb potential of interaction among the particles (as is often assumed in the so-called single-component plasma approximation) is determined by one parameter (the coupling parameter), whereas the phase state of a system in which the particles interact by means of the Yukawa potential is described by two parameters—the coupling parameter and the structure parameter. In a nonideal dusty plasma, the shape of the potential by means of which charged dust grains interact is *a priori* unknown: it may differ markedly from the potential of the interaction between charged dust grains in an ideal plasma. Here, we investigate the self-consistent potential of a charged dust grain and the possibility of the formation of ordered plasma–dust structures in a dusty plasma created by a fast electron beam in nitrogen at room and cryogenic temperatures.

2. NUMERICAL MODELING OF THE DOMAIN OF EXISTENCE OF A COULOMB CRYSTAL IN NITROGEN

As was noted above, the phase state of a system of dust grains in the single-component plasma approximation is determined by one parameter, namely, the coupling parameter or the Coulomb parameter of the interaction between charged particles [6]:

$$\Gamma = \frac{e^2 q^2}{a_d kT}. \quad (1)$$

Here, e is the proton charge, q is dust grain charge in units of the elementary charge, k is Boltzmann's constant, T is the particle temperature, the radius a_d of the Seitz–Wigner cell is equal to

$$a_d = \left(\frac{4}{3}\pi n_d\right)^{-1/3}, \quad (2)$$

1063-780X/02/2801-0028$22.00 © 2002 MAIK "Nauka/Interperiodica"

and n_d is the dust density. Note that, in the literature, the coupling parameter is also defined as the ratio of the interaction energy to the thermal energy of the particles that occur at the mean interparticle distance $a = (n_d)^{-1/3}$:

$$\tilde{\Gamma} = \frac{e^2 q^2}{akT} = \frac{\Gamma}{\left(\frac{4}{3}\pi\right)^{1/3}} \approx \frac{\Gamma}{1.61}.$$

In the single-component plasma approximation, dust crystallization occurs under the condition [6]

$$\Gamma \geq \Gamma_c \approx 172 \text{ or } \tilde{\Gamma} \geq \tilde{\Gamma}_c \approx 106. \quad (3)$$

For a system of particles whose potential is described by the Debye screening potential

$$\phi(r) = \frac{eq}{r}\exp(-r/R_D), \quad (4)$$

where r is the distance from the particle to the point of observation and R_D is the Debye screening radius, Ikezi [7] proposed to use the crystallization condition

$$\Gamma_s \geq \tilde{\Gamma}_c, \quad (5)$$

where he introduced a new coupling parameter for a Debye plasma:

$$\Gamma_s = \frac{e^2 q^2}{akT}\exp(-a/R_D) = \tilde{\Gamma}\exp(-a/R_D). \quad (6)$$

In [8–12], a system of particles interacting by means of potential (4) was simulated using the Monte Carlo (MC) method. It was shown that the conditions for phase transitions are determined by two (rather than one) parameters—the coupling parameter Γ_s and the structure parameter λ, which is defined as $\lambda = a/R_D$. The critical values of the coupling parameter, Γ_{sc}, above which dust crystallization occurs were calculated in [8–12] for different values of the structure parameter λ. The results obtained in those papers are presented in Fig. 1, which also shows the approximate dependence that was proposed by Vaulina and Khrapak [13]. One can see that, in the range of large values of the structure parameter ($\lambda > 8$), this approximation underestimates the parameter Γ_{sc}. For a dusty plasma created by a beam of fast electrons in nitrogen, the values of the structure parameter λ lie precisely in this range. That is why we applied the least squares method to the results of [8–12] and obtained the expression $\Gamma_{sc} = 54/\lambda^{1.38}$, which describes well the calculated dependence (Fig. 1, curve *6*) in the range $\lambda > 1$, which is most typical of experiments with dusty plasmas.

Ordered crystalline structures of dust grains were first observed in RF discharges [14–21]. Later, ordered dust structures were observed in double layers [22], in the strata of a dc glow discharge [23, 24], in a thermally excited plasma [25, 26], and in a nuclear-track plasma [27, 28]. In order to determine the coupling and structure parameters, it is necessary to know the dust grain charge, the screening radius, and the interparticle distance. The last parameter is relatively simple to find, but it is fairly complicated to determine the dust grain charge and Debye radius. Among the researchers whose observations of ordered crystalline structures were cited above, the authors of [14, 15] carried out the most complete investigations of the dust grain charge q and Debye screening radius R_D (see also more recent papers [29–31]). The results of these investigations showed that the experimentally measured Debye radii are larger than the ion Debye radii by a factor of 4 to 10 (this point will be discussed in more detail below); the relative error in determining R_D did not exceed a factor of 2. In [29–31], the values of R_D were determined only for the series of experiments carried out in [15] at different pressures, but they were not determined for the series of experiments carried out at different levels of the supplied RF power. That is why we recalculated the ion Debye radii presented in [15] to the electron Debye radii, assuming that the electron and ion densities are the same and the electron temperature is 3 eV. The electron Debye radii recalculated in this way were found to agree well with the experimentally determined values of the Debye radius. In Fig. 1, we show the values of the coupling parameter that were computed from the recalculated Debye radii for the conditions under which the dust structures in the liquid or crystalline phase were observed in the experiments of [15]. The calculated points are seen to occur mainly in the regions corresponding to the observed phases. For a more precise

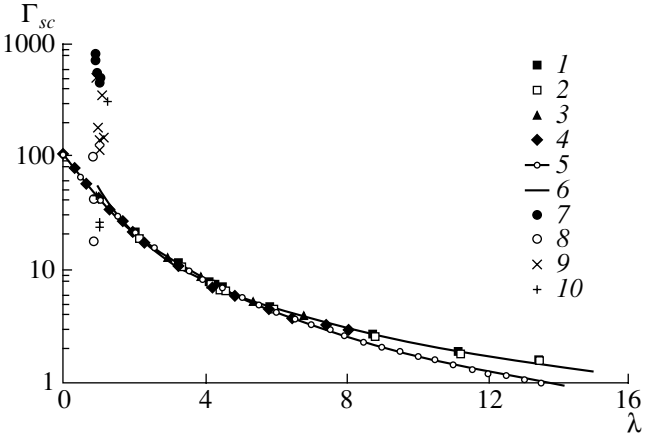

Fig. 1. Dependence of the critical value of the coupling parameter Γ_s on the structure parameter λ: (*1*, *2*) the results of [9], (*3*) the results of [10], (*4*) the results of [12], (*5*) the dependence $\Gamma_{sc} = 106/(1 + \lambda + \lambda^2/2)$ [13], (*6*) the dependence $\Gamma_{sc} = 54/\lambda^{1.38}$, and (*7–10*) the experimental data of [15] recalculated for different pressures (closed and open circles) and different powers of an RF discharge (crosses and pluses) (symbols *7* and *9* refer to a crystalline phase, and symbols *8* and *10* refer to a liquid phase).

experimental verification of the results obtained from MC calculations of the conditions for phase transitions on the basis of the Yukawa potential and the applicability of these results to dusty plasmas, it is necessary to develop more precise methods for dusty plasma diagnostics.

The region where a Coulomb crystal may exist in a nitrogen plasma was simulated using the model that was described in detail in [3, 32]. Briefly, the numerical model is based on a finite-difference method implemented on a nonuniform grid that becomes finer toward the grain surface, the implicit Crank–Nicholson scheme, and the matrix sweep method. The model implies the solution of the set of one-dimensional continuity equations and Poisson's equation in the Seitz–Wigner cell:

$$\begin{aligned}\frac{\partial n_e}{\partial t} + \nabla \cdot \mathbf{j}_e &= Q + k_{\text{ion}} n_e N - \beta_{ei} n_e n_i,\\ \frac{\partial n_i}{\partial t} + \nabla \cdot \mathbf{j}_i &= Q + k_{\text{ion}} n_e N - \beta_{ei} n_e n_i,\\ \nabla \cdot \mathbf{E} &= 4\pi e(n_i - n_e).\end{aligned} \tag{7}$$

Here, n_e and n_i are the electron and ion densities, N is the neutral density, Q is the rate of gas ionization by an external ionizing source, k_{ion} is the rate constant of gas ionization by the plasma electrons, β_{ei} is the electron–ion dissociative recombination coefficient, $\mathbf{j}_e$ and $\mathbf{j}_i$ are the electron and ion current densities, and $\mathbf{E}$ is the electric field strength. The electron and ion flux densities are treated in the drift–diffusion approximation:

$$\begin{aligned}\mathbf{j}_e &= -n_e k_e \mathbf{E} - \nabla(D_e n_e),\\ \mathbf{j}_i &= n_i k_i \mathbf{E} - D_i \nabla n_i,\end{aligned} \tag{8}$$

where k_e and k_i are the mobilities of electrons and ions and D_e and D_i are their diffusion coefficients. The drift–diffusion (or hydrodynamic) approximation for transport processes is valid under the condition that the electron and ion mean free paths are much shorter than the characteristic dimension of the problem; for a nitrogen density of about 2.7×10^{19} cm^{-3}, this condition holds for both ions and electrons. The electric field potential is determined from the equation

$$\mathbf{E} = -\nabla\phi. \tag{9}$$

The problem was solved with the following boundary conditions at the grain surface [3]:

$$\begin{aligned}\left(n_e - \gamma_{0e}\frac{\lambda_e}{r}\frac{\partial(rn_e)}{\partial r}\right)_{|r=r_0} &= 0,\\ \left(n_i - \gamma_{0i}\frac{\lambda_i}{r}\frac{\partial(rn_i)}{\partial r}\right)_{|r=r_0} &= 0.\end{aligned} \tag{10}$$

Here, r_0 is the grain radius and λ_e and λ_i are the electron and ion mean free paths. The correction factors γ_{0e} and γ_{0i} are only weakly dependent on the ratio of the mean free paths to the grain radius, and, in the limit $\lambda_e/r_0 \longrightarrow 0$ (or $\lambda_i/r_0 \longrightarrow 0$), they approach the Hopf constant: $\gamma_{0e} = \gamma_{0i} = \gamma_0 \approx 0.71$. For our analysis, it is important to justify the use of the boundary conditions (10), because they were derived without allowance for the drift motion of the plasma particles under consideration [33, 34].

Hagelaar *et al.* [35] showed that, in a planar problem, the boundary conditions for a plasma in contact with the wall have the form

$$\begin{aligned}&\left(-k_e n_e E_x - D_e\frac{\partial n_e}{\partial x}\right)\Big|_{x=x_0}\\ &= (1-R_e)\left[-\frac{1}{4}v_{\text{th},e}n_e - \frac{1}{2}D_e\frac{\partial n_e}{\partial x}\right]\Big|_{x=x_0} - \gamma j_i|_{x=x_0},\end{aligned} \tag{11}$$

$$\begin{aligned}&\left(k_i n_i E_e - D_i\frac{\partial n_i}{\partial x}\right)\Big|_{x=x_0}\\ &= (1-R_i)\left[k_i n_i E_x - \frac{1}{4}v_{\text{th},i}n_i - \frac{1}{2}D_i\frac{\partial n_i}{\partial x}\right]\Big|_{x=x_0},\end{aligned} \tag{12}$$

where R_e and R_i are the reflection coefficients of the wall surface for electrons and ions, the electron and ion thermal velocities $v_{\text{th},e}$ and $v_{\text{th},i}$ are defined as $v_{\text{th},e(i)} = \sqrt{8kT_{e(i)}/\pi m_{e(i)}}$, and γ is the secondary ion–electron emission coefficient. Conditions (11) and (12) were written under the assumption that the coordinate of the wall is $x = x_0$, which is to the left of the plasma, and that the Cartesian coordinate x is perpendicular to the wall and points toward the plasma. It was also assumed that the electric field is directed toward the wall (the component E_x is negative); this indicates that the drift flux of positive ions is directed toward the wall (as is the case with negatively charged dust grains). In conditions (11) and (12), the left-hand sides are hydrodynamic fluxes and the right-hand sides are kinetic fluxes.

From these conditions, we can obtain

$$\begin{aligned}&\left(\frac{1}{4}v_{\text{th},e} - \frac{1}{1-R_e}k_e E_x\right)n_e\Big|_{x=x_0}\\ &= \frac{1+R_e}{2(1-R_e)}D_e\frac{\partial n_e}{\partial x}\Big|_{x=x_0} - \frac{\gamma}{1-R_e}j_i\Big|_{x=x_0},\end{aligned} \tag{13}$$

$$\begin{aligned}&\left(\frac{1}{4}v_{\text{th},i} + \frac{R_i}{1-R_i}k_i E_x\right)n_i\Big|_{x=x_0}\\ &= \frac{1+R_i}{2(1-R_i)}D_i\frac{\partial n_i}{\partial x}\Big|_{x=x_0}.\end{aligned} \tag{14}$$

First, we take into account the conditions $v_{\text{th},e(i)} \gg v_{\text{drift},e(i)} = k_{e(i)}|E_x|$, which are satisfied when the fields are not too strong (the condition for the electrons coincides with the applicability condition of the two-term approximation for the electron energy distribution function; for nitrogen, the two-term approximation is

valid up to a reduced electric field of 2×10^{15} V cm^2). Second, we take into account the fact that, in a steady-state regime, the electron and ion fluxes onto the grain surface are equal to each other, so that the ion–electron emission can be incorporated by simply introducing a new reflection coefficient for the electrons: $R_e^{\text{new}} = (\gamma + R_e)/(1 + \gamma) \approx \gamma + R_e$. Finally, we also take into account the expression $D_{e(i)} = \frac{1}{3}\lambda_{e(i)} v_{\text{th}, e(i)}$, which holds in the kinetic transport theory. As a result, we can simplify conditions (13) and (14) to

$$\left(n_e - \frac{2}{3}\lambda_e \frac{1 + R_e^{\text{new}}}{1 - R_e^{\text{new}}} \frac{\partial n_e}{\partial x}\right)\Bigg|_{x = x_0} = 0, \quad (15)$$

$$\left(n_i - \frac{2}{3}\lambda_i \frac{1 + R_i}{1 - R_i} \frac{\partial n_i}{\partial x}\right)\Bigg|_{x = x_0} = 0. \quad (16)$$

Davison [33] showed that the replacement $\tilde{n} = nr$ reduces the spherical problem of particle diffusion to the planar problem for the quantity $\tilde{n}$. Consequently, in our problem, we finally obtain from conditions (15) and (16)

$$\left(n_e - \frac{2}{3}\frac{1 + R_e^{\text{new}}}{1 - R_e^{\text{new}}} \frac{\lambda_e}{r} \frac{\partial (r n_e)}{\partial r}\right)\Bigg|_{r = r_0} = 0, \quad (17)$$

$$\left(n_i - \frac{2}{3}\frac{1 + R_i}{1 - R_i} \frac{\lambda_i}{r} \frac{\partial (r n_i)}{\partial r}\right)\Bigg|_{r = r_0} = 0. \quad (18)$$

Note that the reflection coefficient for low-energy charged particles is practically zero, in which case conditions (17) and (18) differ from conditions (10) only in that the coefficients in front of the derivatives are somewhat smaller. The boundary conditions were investigated most systematically in [33, 34]; that is why, in simulations, we used conditions (10). Notably, the quantities $\gamma_{0, e(i)}$ depend on the ratio $\lambda_{e(i)}/r_0$. Based on the results obtained in [33, 34], we calculated the quantities $\gamma_{0, e(i)}$ over a wide range of values of the ratio $\lambda_{e(i)}/r_0$; for $\lambda_{e(i)}/r_0 \leq 1$, these quantities are approximated well by the expression

$$\gamma_{0, e(i)} = 0.71 + 0.18\left(\frac{\lambda_{e(i)}}{r_0}\right)^{5/2}. \quad (19)$$

When developing the theory of probes at elevated pressures, Gorbunov *et al.* [36] used a different approximation, which describes the calculated results much worse (note that, in [36], the expressions approximating γ_0 in the spherical and cylindrical cases were entangled with one another). In the simulations described below, the ratio $\lambda_{e(i)}/r_0$ is smaller than 0.2, while expression (19) implies that, even for $\lambda_{e(i)}/r_0 \approx 0.5$, the deviation of the quantities $\gamma_{0, e(i)}$ from the Hopf constant can be neglected.

Now, we discuss the question of how various processes of electron emission from the grain surface (such as thermal emission, field emission, and ion–electron and secondary electron emissions under the action of a fast electron beam) affect the dust grain charge (recall that this question was briefly analyzed in [32]). In our simulations, these processes, which may change the boundary conditions at the grain surface, were ignored for the following two reasons: first, thermal and field emissions from the "cold" grains play a negligible role, and, second, the electric field is insufficiently strong for the avalanche ionization of the gas (even near the grain surface, where the electric field is the strongest), and the secondary ion–electron emission coefficient γ is usually on the order of 10^{-2} or smaller. Consequently, in accordance with condition (17), taking into account the ion–electron emission can change the boundary conditions only slightly.

Let us discuss the process of the secondary electron emission (SEE) under the action of the beam electrons in more detail. Thus, the experiments of [3] were carried out with a 120-keV electron beam with the current density $j_b = 90$ μA/cm^2. The mass range of the electrons with such an energy in nitrogen is $R_e \approx 18$ mg/cm^2 [37], which corresponds to the mean free path $L_e \approx 14$ cm at atmospheric pressure, and, in glass–carbon compounds, the mean free path is about $L_{e, d} \approx 90$ μm. In [3], spherical glass–carbon grains with a mean diameter of 24 μm were used.

The SEE coefficient σ depends on the properties and structure of both the grain surface and grain material, the energy of the incident electrons, and the angle of incidence. For conventional materials (in particular, for glass–carbon compounds), the coefficient σ reaches its maximum value (on the order of unity) at electron energies of about several hundred electronvolts [37]. For higher electron energies, the coefficient σ gradually decreases. Under the condition $L_{e, d} > 2r_0$, the beam electrons with higher energies may knock the secondary electrons out of the grain surface opposite to that on which they are incident. However, for conventional materials, the SEE coefficient associated with such a "shooting-through" effect of the beam is also smaller than unity [37]. The smallness of the SEE coefficient is associated with the short mean free path of the secondary electrons created within the grain: only the electrons that are produced in a thin surface layer can escape from the grain. For estimates, we set $\sigma = 1$. Then, the flux of the secondary electrons from the grain surface under the action of a fast electron beam with current density j_b is described by the expression

$$J_{ee} = \frac{j_b}{e}\sigma\pi r_0^2. \quad (20)$$

Table 1. Parameters for approximating the potential of a dust grain with the radius $r_0 = 12$ μm for different ionization rates in a dusty nitrogen plasma with the neutral density $N = 2.5 \times 10^{19}$ cm^{-3} and dust density $n_d = 10^5$ cm^{-3} at room temperature ($T = T_i = T_e = 300$ K)

Q, cm^{-3} s^{-1}	1.5×10^{12}	1.5×10^{13}	1.5×10^{14}	1.5×10^{15}	1.5×10^{16}	1.5×10^{17}	7.5×10^{17}
R_D, μm	28.728	14.976	8.264	4.639	2.609	1.467	0.981
$R_{D,\,e}$	40.458	21.092	11.638	6.533	3.674	2.066	1.382
$R_{D,\,a}$	40.247	29.942	19.701	12.247	7.570	4.814	3.705
q_{cal}	−3351.927	−4328.708	−5961.526	−9220.038	−15495.92	−25351.38	−34088.65
q_1	−4432.554	−5981.463	−9437.905	−19788.97	−56167.31	−172939.3	−308065.8
q_2	−4600.606	−6375.184	−10785.03	−26627.10	−106031.7	−598937.3	−1853496
$R_{D,\,a\,short}$	61.504	43.465	28.709	18.891	12.437	7.66	5.147
$q_{1,\,short}$	−3404.71	−4439.58	−6251.96	−10087	−18267.1	−34466.4	−54224.1

Table 2. Parameters for approximating the potential of a dust grain with the radius $r_0 = 12$ μm for different ionization rates in a dusty nitrogen plasma with the neutral density $N = 2.5 \times 10^{19}$ cm^{-3} and dust density $n_d = 10^5$ cm^{-3} at cryogenic temperature ($T = T_i = T_e = 77$ K)

Q, cm^{-3} s^{-1}	1.5×10^{12}	1.5×10^{13}	1.5×10^{14}	1.5×10^{15}	1.5×10^{16}	1.5×10^{17}	7.5×10^{17}
R_D, μm	15.525	8.563	4.805	2.702	1.519	0.854	0.571
$R_{D,\,e}$	21.956	12.109	6.795	3.821	2.149	1.208	0.808
$R_{D,\,a}$	17.813	12.011	7.249	4.34	2.579	1.614	1.028
q_{cal}	−3391.431	−6035.777	−11519.84	−20830.43	−33428.32	−49930.00	−64624.17
q_1	−31055.76	−153166.4	−2221586	-4.585×10^7	-5.163×10^8	-4.926×10^9	-6.44×10^{11}
q_2	−36394.98	−208078.8	−4379966	-1.934×10^8	-9.578×10^9	-9.91×10^{11}	-5.94×10^{15}
$R_{D,\,a\,short}$	59.147	45.855	36.075	27.603	19.591	15.894	11.939
$q_{1,\,short}$	−3431.37	−6144.80	−11829.57	−21686.37	−35735.77	−49958.70	−64659.30

In [3], it was noted that, in a steady state, the ion flux (as well as the electron flux) onto the grain surface is nearly equal to the Langevin flux:

$$J_{i0} = 4\pi e k_i q n_{i0} = \beta_{id} q \sqrt{Q/\beta_{ei}}. \quad (21)$$

Now, from expressions (20) and (21), we can determine the dust grain charge at which the SEE current becomes equal to the ion current:

$$q_e = \frac{j_b}{e} \frac{\sigma \pi r_0^2}{\beta_{id} \sqrt{Q/\beta_{ei}}} \propto Q^{1/2} r_0^2. \quad (22)$$

Let us estimate the charge of dust grains of radius 12 μm for the beam current density $j_b = 90$ μA/cm^2 (at a gas density under normal conditions, equal to 2.687×10^{19} cm^{-3}, this corresponds to the gas ionization rate $Q = 1.5 \times 10^{17}$ cm^{-3} s^{-1} [38]). A nitrogen plasma at atmospheric pressure is dominated by N_4^+ ions, whose mobility at room temperature is equal to 2.3 cm^2/V s [39]. Then, taking into account the relationship $\sigma = 1$, we find that, for $Q = 1.5 \times 10^{17}$ cm^{-3} s^{-1}, the critical grain charge is about $q_e \approx 1850$. The results of numerical modeling described below (see Tables 1, 2) show that, at such a high ionization rate, the grain charge is one order of magnitude larger than the estimate that we have just obtained. Hence, we can conclude that, with allowance for dependence (22) of the grain charge q_e on the ionization rate, the SEE can be ignored in our analysis.

The fluxes through the right boundary of the elementary cell were set equal to zero. The condition for the cell to be electrically neutral implies that the electric field at the cell boundary should vanish:

$$j_e|_{r = a_d} = 0, \quad j_i|_{r = a_d} = 0, \quad E|_{r = a_d} = 0. \quad (23)$$

In order to calculate the coupling parameter of the Debye plasma, it is necessary to know the Debye screening radius. Recall that the Debye potential is introduced as a solution to Poisson's equation with the Boltzmann distributions of the ion and electron densities under the assumption that the coupling parameter is small. However, in a dusty plasma, the coupling parameter is not small and, in addition, the electron and ion distributions are thermodynamically nonequilibrium, because electron and ion fluxes onto the dust grains are not counterbalanced by the electron and ion fluxes emitted from the grain surfaces. From the probe theory [40–42], it is well known that, when the negative potential of the probes is sufficiently high in absolute value,

the electron density is approximately described by the Boltzmann distribution; on the other hand, the density of the positive ions, which are attracted by the negative charge of a dust grain, does not obey a Boltzmann distribution even approximately.[1] That is why, for a dusty plasma, the so-called Poisson–Boltzmann equation (i.e., Poisson's equation with Boltzmann distributions for electrons and ions), which is widely applied in the literature, is, in our opinion, physically unjustified. The question of whether the Debye potential with the screening radius derived from the theory of an ideal plasma can be used to describe a strongly nonideal system also requires justification. This question has already been discussed in the literature (see, e.g., [1, 43]). Another question to be addressed is whether or not the dust component takes part in the screening of the dust grain charge. Tsytovich [1] arrived at the following conclusion: if there are many dust grains inside the Debye sphere, then the dust component affects the screening processes and the plasma Debye radius should be described by the expression

$$\frac{1}{R_D^2} = \frac{1}{R_{D,e}^2} + \frac{1}{R_{D,i}^2} + \frac{1}{R_{D,d}^2}, \qquad (24)$$

where $R_{D,e}$, $R_{D,i}$, and $R_{D,d}$ are the Debye radii of the electron, ion, and dust components, respectively. However, under laboratory conditions, there is less than one dust grain inside a Debye sphere, so that the dust cannot be regarded as a plasma component and the Debye radius in such a plasma should be determined by the plasma electrons and ions.

Under discharge conditions, the electron temperature T_e is much higher than the ion temperature T_i ($T_e \gg T_i$); consequently, it seems likely that the Debye radius should be determined by the ion component [7]. In contrast, Thomas *et al.* [16] assumed that $R_D \approx R_{D,e}$. This assumption was based on the fact that, according to Bohm's theory, the ions in an RF discharge enter the space-charge electrode sheath (where $n_e \ll n_i$) with an energy of about the electron thermal energy.[2] As a result, the authors of [16] concluded that the ion temperature should be comparable to the electron temperature, in which case $R_D \approx R_{D,e}$. In our opinion, this conclusion is erroneous, because the energy with which the ions enter the sheath is associated with the directed (rather than thermal) ion motion. It is precisely the thermal motion of electrons and ions that ensures the screening of the dust grain charges in dusty plasmas.

In [29, 30, 44–46], different experimental methods were used to determine the Debye screening radius in RF discharges in He at the pressures p = 1–100 Pa [29] and p = 22 Pa [30], in Kr at the pressures p = 7–40 Pa [44], and in Ar at the pressures p = 2–3 Pa [45] and p = 2.7 Pa [46]. The most reliable results on the Debye radius were obtained by Konopka *et al.* [46], who experimentally measured the potential of the interaction between the grains in the range from about R_D to about $3R_D$ and then calculated the Debye radius by adjusting the theoretical dependence (4) to fit the experimental points. They established that the experimentally measured interaction potential is described by expression (4) with an accuracy of 10–20%. Estimates showed that the Debye screening radii measured in the experiments of [29, 30, 44–46] were an order of magnitude larger than the ion Debye radius; consequently, we can conclude that the Debye screening radius is most likely determined by the electron component.

The nature of the screening of the electric field of a highly charged macroparticle in a colloidal plasma was investigated numerically by Bystrenko and Zagorodny [47]. They simulated the behavior of the grain potential by solving the Poisson–Boltzmann equation and by MC calculation of the evolution of an ensemble of charged particles in the electric field of a grain. They established that the results from the investigation of the radial charge distribution by solving the Poisson–Boltzmann equation agree fairly well with the MC simulation results. They found that the grain potential determined from the solution to the Poisson–Boltzmann equation differs markedly from that predicted by the Debye–Hückel theory; moreover, the smaller the grain, the larger is the discrepancy. Bystrenko and Zagorodny [48] investigated the question of how the effects that they revealed in [47] influence the conditions for phase transitions in a colloidal plasma.

However, the results of [47, 48] were obtained without allowance for the electron and ion absorption by dust grains (in that case, the plasma is thermodynamically equilibrium and, accordingly, the ions and electrons obey Boltzmann distributions) and, hence, are inapplicable to a dusty plasma. In simulating the behavior of a dusty plasma, Lapenta [49, 50] showed that the calculated grain potential can be approximately described by the Debye potential, whose screening radius does not differ appreciably from the electron Debye radius. When investigating NSSDs in helium at atmospheric pressure, Ivanov *et al.* [51] numerically calculated the dust grain potential using a model that differs from our model only in a few details. They found that the screening radius obtained from the Yukawa potential, which is the best approximation for the calculated potential, differs markedly from the Debye radius calculated from the plasma parameters. Moreover, the screening radius obtained by approximating the calculated potential by the Yukawa potential was found to be even larger than the electron Debye radius.

Here, we present the results of calculations of the radial profile of the dust grain potential in a dusty nitrogen plasma at room (T = 300 K) and cryogenic (T = 77 K) temperatures. The rate of gas ionization by a fast elec-

[1] For positively charged dust grains, the situation is opposite.

[2] The condition for the sheath to be stable implies that the ion energy at the entrance to the sheath should be higher than $1/2kT_e$ [40].

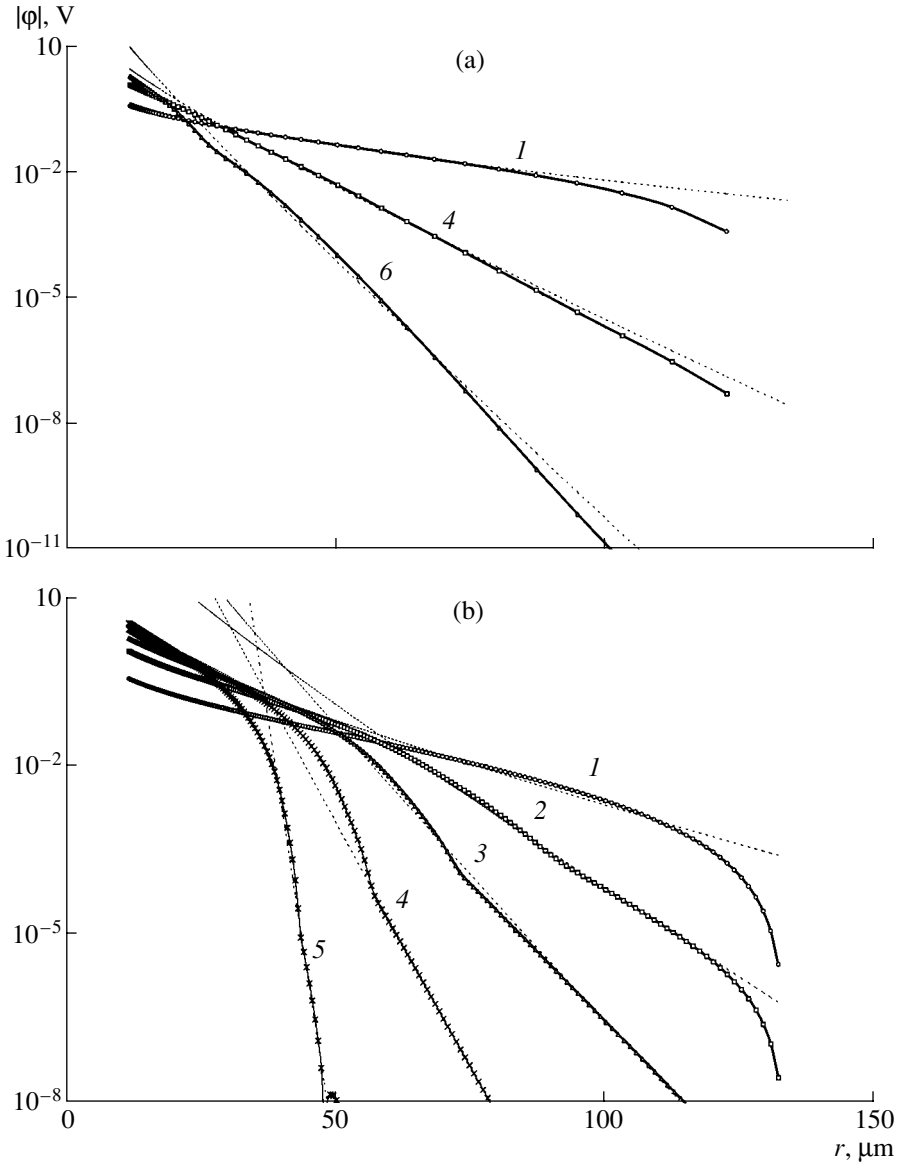

Fig. 2. Radial profiles of the calculated and approximate potentials of a dust grain with the radius $r_0 = 12$ μm in a homogeneous nitrogen plasma with the dust density $n_d = 10^5$ cm^{-3} at (a) room and (b) cryogenic temperatures for Q = (*1*) 1.5×10^{12}, (*2*) 1.5×10^{14}, (*3*) 1.5×10^{15}, (*4*) 1.5×10^{16}, (*5*) 1.5×10^{17}, and (*6*) 7.5×10^{17} cm^{-3} s^{-1}. The curves with symbols are calculated results, and the dashed curves are approximations by the Debye potential.

tron beam was varied in the range 1.5×10^{12}–7.5×10^{17} cm^{-3} s^{-1}, the dust density was 10^3–10^7 cm^{-3}, the grain radius was 6–50 μm, and the gas density was set equal to the density under normal conditions. The calculations were carried out on the reference and auxiliary grids described by the expressions

$$r_{k=0} = r_0, \quad r_{k+1} = r_k + h_k, \quad r_{k=M} = a_d,$$
$$r_{k+1/2} = (r_{k+1} + r_k)/2,$$

where M is the number of mesh points on the reference grid, $h_k = (1 + \alpha)^k h$, $h = \alpha(a_d - r_0)/\{(1 + \alpha)^{M-1} - 1\}$, and the parameter α describes the extent to which the grids are nonuniform (for $\alpha = 0$, we deal with uniform grids with a regular spacing h). For $T = 300$ K, most of the calculations were carried out at $M = 61$ and $\alpha = 0.05$. For $T = 77$ K, the calculations were mostly performed at $M = 201$ and $\alpha = 0.05$, because, at cryogenic temperature, the electron mobility is high and the electron diffusion coefficient is large. In test calculations, we increased the number of mesh points up to 1001 and varied the parameter α from 0 to 0.1. Figure 2 shows the potentials calculated for grains with the radius $r_0 = 12$ μm at the dust density $n_d = 10^5$ cm^{-3}. At low ionization rates, the grain potential is seen to decrease far more gradually than at high ionization rates. At a high

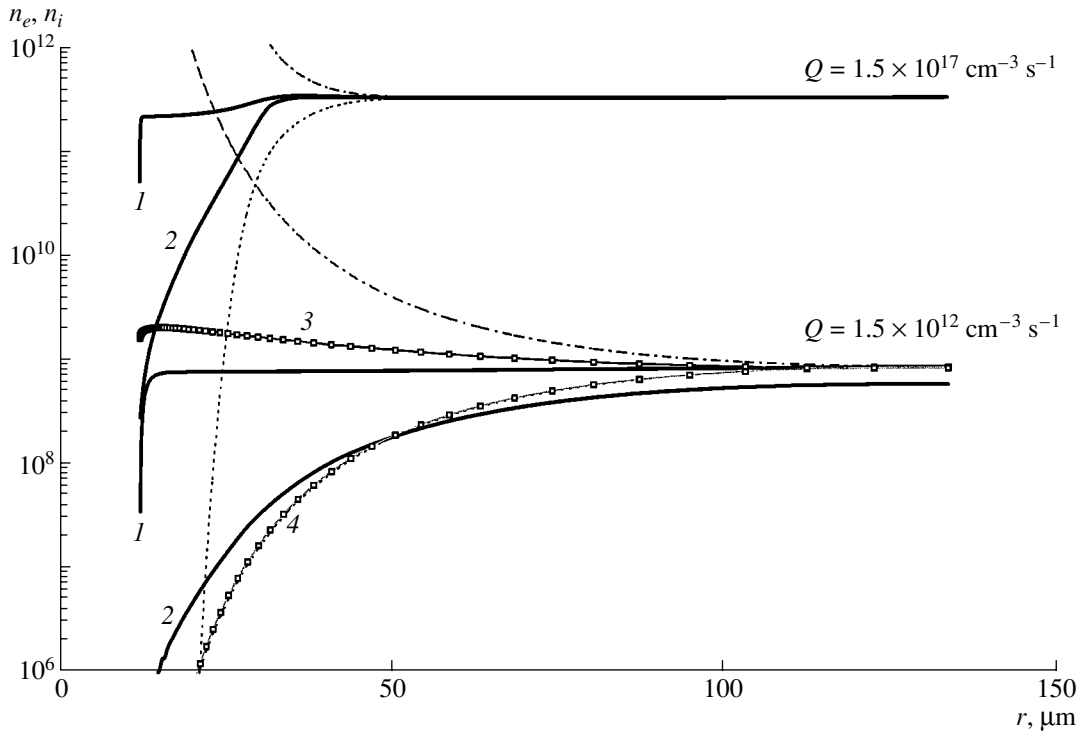

Fig. 3. Radial profiles of the (*1*) ion and (*2*) electron densities in a dusty nitrogen plasma ionized by a fast electron beam at two different rates and the Boltzmann ion (dashed-and-dotted curves) and electron (dashed curves) density distributions with the calculated potential at room temperature for $r_0 = 12$ μm and $n_d = 10^5$ cm^{-3}. Curves *3* and *4* are the ion and electron density profiles calculated from the probe theory.

ionization rate of the gas at cryogenic temperature, the potential drops especially sharply. Figure 2 also shows the curves obtained by applying the least squares method to approximate the grain potential by expression (4) at points lying at moderate and large distances from the grain, except for several points closest to the boundary of the Seitz–Wigner cell. From Fig. 2, we can see that, for the given dust density, the potentials calculated at the distances $r = 30$–100 μm from the grain are approximated well by the Debye potential. As the boundary of the Seitz–Wigner cell is approached, the deviation of the calculated potential from the Debye potential increases because the boundary condition (23) requires that the cell be quasineutral. When solving the Poisson–Boltzmann equation for the Seitz–Wigner cell in a colloidal plasma, Alexander *et al.* [52] proposed to ensure plasma quasineutrality in the cell by approximating the numerical solution for the potential by the expression

$$\varphi = \frac{A}{r}\exp(-r/R_D) + \frac{B}{r}\exp(r/R_D) + D, \qquad (25)$$

where A, B, and D are constants and the Debye radius R_D is governed by the ions of a colloidal plasma. In the Debye–Hückel theory, potential (25) is the solution to the linearized Poisson–Boltzmann equation in a spherical cell of finite radius. Note, however, that, since this approach makes it possible to improve the potential only at distances on the order of the Debye length from the grain, it cannot be used in the case under discussion, in which the Debye radius is appreciably smaller than the radius of an elementary cell.

In Fig. 3, we compare the radial profiles of the ion and electron densities with the Boltzmann distributions. One can see that, near the dust grain, the ion density profile differs radically from the Boltzmann distribution, while the electron density profile qualitatively follows it (especially at low ionization rates of the gas). This behavior of the profiles stems from the following circumstances. In the region near the grain where the plasma is nonquasineutral, both the drift component (which is the main component over most of the cell volume) and the diffusive component of the current of positive ions are directed toward the grain and are not counterbalanced. That is why the ion plasma component is strongly nonequilibrium and, as a consequence, the ion density profile $n_i(r)$ cannot be described by the Boltzmann distribution. On the other hand, the drift and diffusive components of the electron current are oppositely directed and almost completely counterbalance one another. From Fig. 3, we can see that the condition $\nabla n_e \gg \nabla n_i$ fails to hold only in a narrow layer close to

the grain surface. Consequently, in the first approximation, the term that accounts for the diffusive ion current can be discarded. Then, using the condition that the total electron and ion current in the steady state be zero and neglecting the radial variation of the ion density, we can obtain

$$n_e \approx n_{e0}\frac{k_e + k_i}{k_e}\exp\left(\frac{k_e\varphi}{D_e}\right) - n_i\frac{k_i}{k_e} \approx n_{e0}\exp\left(\frac{e\varphi}{kT_e}\right), \quad (26)$$

where $n_{e0} = n_{i0} = \sqrt{Q/\beta_{ei}}$ are the electron and ion densities in a plasma that is not perturbed by the dust component. The last of the approximate equalities (26) was obtained using the condition $k_e \gg k_i$ and the Einstein relationship

$$\frac{D_e}{k_e} = \frac{kT_e}{e}. \quad (27)$$

As follows from Fig. 3, the condition $n_i(r) \approx$ const is better satisfied at low rates of gas ionization; consequently, it is at low ionization rates that the electron density distribution is better described by the Boltzmann expression (26). Figure 3 also shows the electron and ion density profiles calculated from the probe theory for $Q = 1.5 \times 10^{12}$ cm^{-3} s^{-1} [40]. We can see that, first, the electron density profile nearly coincides with the Boltzmann distribution and, second, although the ion density profile is closer to the calculated profile than the Boltzmann distribution, it still remains markedly different from the calculated one.

Tables 1 and 2 list the parameters for approximating the potential of a dust grain with the radius $r_0 = 12$ μm in a dusty nitrogen plasma with the neutral density $N = 2.5 \times 10^{19}$ cm^{-3} and dust density $n_d = 10^5$ cm^{-3} at room and cryogenic temperatures. The effective dust grain charge can be determined from the above approximate expression for the potential, or from the requirement that the electric field at the grain surface should coincide with the Coulomb field of a grain with an effective charge q_1, or from the condition that the potential be completely described by expression (4). In the first case, we are dealing with the Derjaguin–Landau–Verwey–Overbeek (DLVO) potential, which incorporates the finite sizes of the grains [47]:

$$\phi = \frac{eq_1}{1 + r_0/R_{D,a}}\frac{1}{r}\exp\left(-\frac{r - r_0}{R_{D,a}}\right), \quad (28)$$

where $R_{D,a}$ is the approximate Debye radius. The electric field is described by the expression

$$E = \frac{eq_1}{r^2}\frac{1 + r/R_{D,a}}{1 + r_0/R_{D,a}}\exp\left(-\frac{r - r_0}{R_{D,a}}\right). \quad (29)$$

In expression (4), the effective charge q_1 and the approximate charge (which will be denoted below by q_2) are related by

$$q_2 = \frac{q_1}{1 + r_0/R_{D,a}}\exp(r_0/R_{D,a}); \quad (30)$$

under the condition $r_0 \ll R_{D,a}$, they nearly coincide. Note that it is the squared approximate charge q_2^2 that enters the expression for the coupling parameter Γ_s.

For comparison, Tables 1 and 2 present the values of the plasma Debye radius and electron Debye radius calculated from the classical expressions

$$R_D = \left(\frac{1}{R_{D,e}^2} + \frac{1}{R_{D,i}^2}\right)^{-\frac{1}{2}}, \quad R_{D,e} = \sqrt{\frac{kT_e}{4\pi e^2 n_{e0}}}, \quad R_{D,i} = \sqrt{\frac{kT_i}{4\pi e^2 n_{i0}}}. \quad (31)$$

From Tables 1 and 2, one can see that, at low rates of gas ionization, the approximate screening radius $R_{D,a}$ nearly coincides with the electron Debye radius and, as the ionization rate increases at room temperature, the approximate radius departs increasingly from the electron Debye radius in such a way that $R_{D,a} > R_{D,e}$. When the gas is ionized by an external source at the rate $Q = 1.5 \times 10^{12}$ cm^{-3} s^{-1}, the electron and ion densities far from the dust grain are about 10^9 cm^{-3}. In experiments on determining the Debye radius [29, 30, 44–46], the densities of charged particles were lower than or equal to this. Presumably, it is for this reason that, in those experiments, the measured Debye screening radii coincided with the electron Debye radii (however, we cannot speak of exact coincidence, because either the Debye radius itself or the electron density and temperature were measured with low accuracy).

The approximation of the data listed in Tables 1 and 2 by simple expressions showed that the dependence of the Debye radius $R_{D,a}$ and the calculated grain charge q_{cal} on the ionization rate is described with good accuracy by the relationships

$$R_{D,a} = 0.9Q^{-0.19} \quad (T = 300\ \text{K}), \quad R_{D,a} = 5.2Q^{-0.275} \quad (T = 77\ \text{K}), \quad (32)$$

$$q_{\text{cal}} = -1900(1 + 0.001Q^{0.237}) \quad (T = 300\ \text{K}), \quad q_{\text{cal}} = -565(1 + 0.0072Q^{0.237}) \quad (T = 77\ \text{K}), \quad (33)$$

where $R_{D,a}$ is in cm and Q is in cm^{-3} s^{-1}. Note that, according to expressions (33), the dust grain charge at low ionization rates approaches the value predicted by

a simplified theory of grain charging [53] at low dust density:

$$q_0 = -\frac{kT_e r_0}{e^2}\ln\left(1 + \frac{k_e}{k_i}\right). \quad (34)$$

At cryogenic temperature (T = 77 K), we have k_i = 1.9 V cm^2/s and k_e = 51850 V cm^2/s, so that q_0 = –565; at room temperature (T = 300 K), we have k_i = 2.3 V cm^2/s and k_e = 16280 V cm^2/s, so that q_0 = –1910. It is of interest to note that, at room and cryogenic temperatures, the dust grain charges as functions of the ionization rate obey the same power law.

A comparison between the grain charges in Tables 1 and 2 that were calculated numerically and were approximated from the potential at moderate and large distances from the grain shows that the effective and approximate charges are both larger than the calculated charge, $q_1 > q_{cal}$ and $q_2 > q_{cal}$ (according to Fig. 2, the approximate potential at $r = r_0$ is higher than the calculated one). Such a value of the effective charge of a dust grain cannot be explained in terms of an ion cloud around the grain (in this case, the effective charge would be smaller than the real charge). Approximating the potential from the data obtained at short distances from the grain (r = 12–20 μm) showed that, in accordance with Tables 1 and 2, the approximate charge $q_{1,\,short}$ nearly coincides with the calculated charge (especially at low ionization rates) and the Debye radius is appreciably larger than that approximated from the points lying at moderate distances from the grain.

The dependence of the coupling parameter on the gas ionization rate for a dusty nitrogen plasma at room temperature is illustrated in Fig. 4a, which shows that the approximations of the potential from the data calculated at both short and long distances from the grain lead to nearly the same behavior of the coupling parameter as the gas ionization rate changes. That is why, in what follows, we will determine the coupling parameter Γ_s at T = 300 K by using the parameters for approximating the grain potential from the data obtained over the entire Seitz–Wigner cell. On the other hand, at T = 77 K (Fig. 4b), the approximations from the data obtained at short and long distances from the grain lead to radically different values of Γ_s. This difference stems from the fact that, at cryogenic temperature, the grain potential exhibits a more complicated behavior (Fig. 2). From Fig. 4b, we can see that, at T = 77 K, the Γ_s values approximated from the data obtained at short distances from the grain are larger than Γ_{sc} for ionization rates up to $Q \sim 10^{17}$ cm^{-3} s^{-1}; in contrast, at T = 300 K, we have $\Gamma_s > \Gamma_{sc}$ for ionization rates up to $Q \approx 3 \times 10^{14}$ cm^{-3} s^{-1}. Hence, we can conclude that, at cryogenic temperature, the parameter range in which the ordered dust-grain structures can exist at dust densities higher than 10^5 cm^{-3} will be significantly wider in comparison with that at room temperature. On the other hand, according to the approximations from the data obtained at moderate and long distances from the grain, the parameter range over which the crystallization condition $\Gamma_s \geq \Gamma_{sc}$ is satisfied at room temperature turns out to be only slightly wider than that at cryogenic temperature.

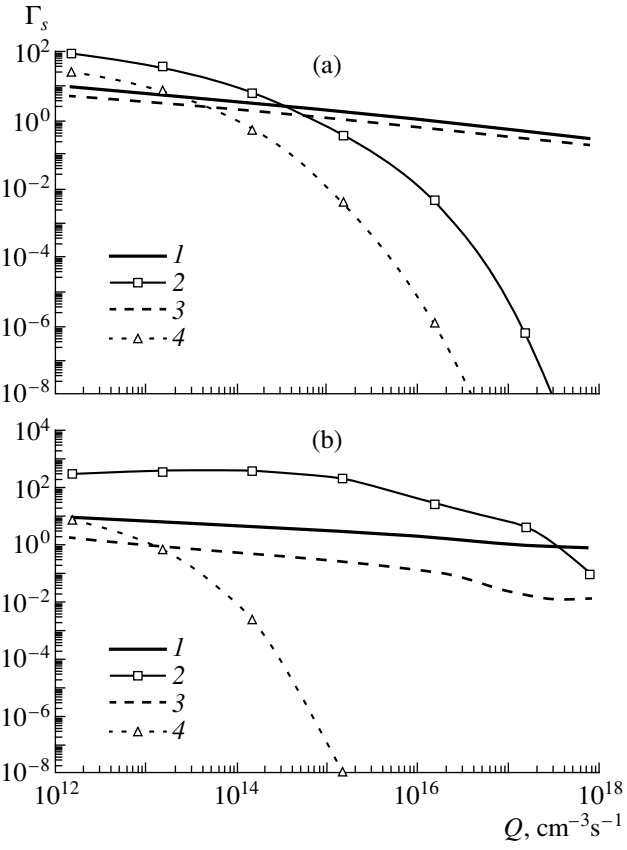

Fig. 4. Dependence of the coupling parameter on the gas ionization rate in a dusty nitrogen plasma at (a) room and (b) cryogenic temperatures for r_0 = 12 μm and $n_d = 10^5$ cm^{-3}. The critical values Γ_{sc} (curves *1*, *3*) and the coupling parameter (curves *2*, *4*) are calculated from the parameters for approximating the potential at short (curves *1*, *2*) and long (curves *3*, *4*) distances from the grain.

Figure 5 illustrates the coupling parameter calculated as a function of the structure parameter at r_0 = 12 μm for a dusty nitrogen plasma at room temperature. In Fig. 5, we also show the range of plasma parameters where ordered plasma–dust structures such as Coulomb crystals are expected to form. It is seen in Figs. 4 and 5 that there exists a range of dusty plasma parameters in which the coupling parameter Γ_s substantially exceeds its critical value Γ_{sc}.

Figure 5 also shows that, as the gas ionization rate increases at a fixed dust density, the coupling parameter Γ_s goes through a maximum. Such behavior is associated with the fact that, at low ionization rates, the dust grains acquire a small charge, so that the values of $\tilde{\Gamma}$

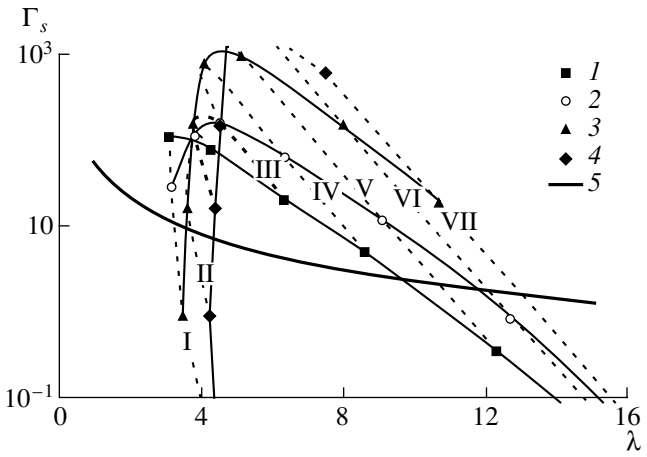

Fig. 5. Dependence of the coupling parameter on the structure parameter in a dusty nitrogen plasma containing dust grains with the radius $r_0 = 12$ μm at room temperature for $n_d = (1)\ 2\times10^5$, $(2)\ 5\times10^5$, $(3)\ 2\times10^6$, and $(4)\ 5\times10^6$ cm^{-3}. Curve *5* shows the dependence $\Gamma_{sc} = 54/\lambda^{1.38}$. The dotted curves are the contour lines of the ionization rate Q = (I–VI) $1.5\times(10^{12}$–$10^{17})$ and (VII) 7.5×10^{17} cm^{-3} s^{-1}.

and, accordingly, Γ_s are both small. As Q grows, $\tilde{\Gamma}$ increases, in which case Γ_s also increases, although the Debye radius decreases, which leads to an increase in the structure parameter and a decrease in the exponential factor in formula (6). As Q grows further, an increase in $\tilde{\Gamma}$, which is associated with an increase in the grain charge, becomes insufficient to cancel out a decrease in the exponential factor, so that the coupling parameter Γ_s starts decreasing. Note that, as the dust density increases at a constant ionization rate, the coupling parameter exhibits an interesting behavior: it also goes through a maximum. Such behavior can be explained as follows. At low dust densities, the grain charge is practically independent of n_d. An increase in n_d leads to a reduction in the interparticle distance and, accordingly, in the structure parameter:

$$q \propto n_d^0, \quad \tilde{\Gamma} \propto n_d^{1/3},$$
$$\lambda \propto n_d^{-1/3} \Rightarrow \Gamma_s \propto n_d^{1/3}\exp(-n_d^{-1/3}R_D^{-1}).$$

This indicates that Γ_s increases with n_d. For high dust densities, the simplified theory of grain charging [53] predicts the following dependence of the dust grain charge on the parameters of the dusty plasma: $q \propto \sqrt{Q}n_d^{-1}$. In this case, we obtain $\tilde{\Gamma} \propto n_d^{-5/3}$ and $\Gamma_s \propto n_d^{-5/3}\exp(-n_d^{-1/3}R_D^{-1})$. Hence, taking into account the smallness of the structure parameter, we see that, at high dust densities, the coupling parameter Γ_s is a decreasing function of n_d.

3. CONCLUSIONS

The results of our study can be summarized as follows.

(i) The self-consistent potential of a dust grain can be approximated with reasonable accuracy by the Debye potential. At low gas ionization rates, the Debye screening radius $R_{D,a}$ practically coincides with the electron Debye radius $R_{D,e}$. At higher ionization rates, the radius $R_{D,a}$ becomes significantly larger than $R_{D,e}$.

(ii) At low ionization rates, the electron density closely obeys a Boltzmann distribution. As the ionization rate increases, the radial electron density profile progressively deviates from the Boltzmann distribution. On the other hand, the Boltzmann distribution cannot be used for ions, even as a rough approximation.

(iii) For a homogeneous nitrogen plasma ionized by an external source, there exists a parameter range in which an ensemble of dust grains is expected to pass over to a crystalline phase.

(iv) The plasma parameter range in which Coulomb crystals of dust grains can exist at cryogenic temperature (T = 77 K) may turn out to be much wider than that at room temperature (T = 300 K).

ACKNOWLEDGMENTS

This work was supported in part by the Russian Foundation for Basic Research, project no. 01-02-17726-a.

REFERENCES

1. V. N. Tsytovich, Usp. Fiz. Nauk **167**, 57 (1997) [Phys. Usp. **40**, 53 (1997)].
2. A. P. Nefedov, O. F. Petrov, and V. E. Fortov, Usp. Fiz. Nauk **167**, 1215 (1997) [Phys. Usp. **40**, 1163 (1997)].
3. A. F. Pal', A. O. Serov, A. N. Starostin, *et al.*, Zh. Éksp. Teor. Fiz. **119**, 272 (2001) [JETP **92**, 235 (2001)].
4. J. P. Hansen, Phys. Rev. A **8**, 3096 (1973).
5. J. P. Hansen, Phys. Rev. A **8**, 3110 (1973).
6. S. Ichimaru, Rev. Mod. Phys. **54**, 1017 (1982).
7. H. Ikezi, Phys. Fluids **29**, 1764 (1986).
8. M. O. Robbins, K. Kremer, and G. S. Grest, J. Chem. Phys. **88**, 3286 (1988).
9. M. J. Stevens and M. O. Robbins, J. Chem. Phys. **98**, 2319 (1993).
10. E. J. Meijer and D. Frenkel, J. Chem. Phys. **94**, 2269 (1991).
11. R. T. Farouki and S. Hamaguchi, Appl. Phys. Lett. **61** (25), 2973 (1992).
12. S. Hamaguchi, R. T. Farouki, and D. H. E. Dubin, Phys. Rev. E **56**, 4671 (1997).
13. O. S. Vaulina and S. A. Khrapak, Zh. Éksp. Teor. Fiz. **117**, 326 (2000) [JETP **90**, 287 (2000)].
14. A. Melzer, T. Trottenberg, and A. Piel, Phys. Lett. A **191**, 301 (1994).
15. A. Melzer, A. Homann, and A. Piel, Phys. Rev. E **53**, 2757 (1996).

16. H. Thomas, G. E. Morfill, V. Demmel, *et al.*, Phys. Rev. Lett. **73**, 652 (1994).
17. H. M. Thomas and G. E. Morfill, Nature **379**, 806 (1996).
18. J. H. Chu and Lin I, Phys. Rev. Lett. **72**, 4009 (1994).
19. J. H. Chu, J.-B. Du, and Lin I, J. Phys. D **27**, 296 (1994).
20. Y. Hayashii and K. Tachibana, Jpn. J. Appl. Phys., Part 2 **33**, L804 (1994).
21. Y. Hayashii and K. Takahashi, Jpn. J. Appl. Phys., Part 1 **36**, 4976 (1997).
22. A. Barkan and R. L. Merlino, Phys. Plasmas **2**, 3261 (1995).
23. V. E. Fortov, A. P. Nefedov, V. M. Torchinskiĭ, *et al.*, Pis'ma Zh. Éksp. Teor. Fiz. **64**, 86 (1996) [JETP Lett. **64**, 92 (1996)].
24. V. E. Fortov, A. P. Nefedov, V. M. Torchinsky, *et al.*, Phys. Lett. A **229**, 317 (1997).
25. V. E. Fortov, A. P. Nefedov, O. F. Petrov, *et al.*, Pis'ma Zh. Éksp. Teor. Fiz. **63**, 176 (1996) [JETP Lett. **63**, 187 (1996)].
26. V. E. Fortov, A. P. Nefedov, O. F. Petrov, *et al.*, Zh. Éksp. Teor. Fiz. **111**, 476 (1997) [JETP **84**, 256 (1997)].
27. V. E. Fortov, V. I. Vladimirov, L. V. Deputatova, *et al.*, Dokl. Akad. Nauk **366**, 184 (1999) [Dokl. Phys. **44**, 279 (1999)].
28. V. E. Fortov, A. P. Nefedov, V. I. Vladimirov, *et al.*, Phys. Lett. A **258**, 305 (1999).
29. S. Peters, A. Homann, A. Melzer, and A. Piel, Phys. Lett. A **223**, 389 (1996).
30. A. Homann, A. Melzer, S. Peters, and A. Piel, Phys. Rev. E **56**, 7138 (1997).
31. A. Homann, A. Melzer, and A. Piel, Phys. Rev. E **59**, R3835 (1999).
32. A. F. Pal', A. N. Starostin, and A. V. Filippov, Fiz. Plazmy **27**, 155 (2001) [Plasma Phys. Rep. **27**, 143 (2001)].
33. B. Davison, *Neutron Transport Theory*, with the collaboration of J. B. Sykes (Clarendon Press, Oxford, 1957; Atomizdat, Moscow, 1960).
34. G. I. Marchuk, *Methods of Computation of Nuclear Reactors* (Atomizdat, Moscow, 1961).
35. G. J. M. Hagelaar, F. J. De Hoog, and G. M. W. Kroesen, Phys. Rev. E **62**, 1452 (2000).
36. N. A. Gorbunov, N. B. Kolokolov, and A. A. Kudryavtsev, Fiz. Plazmy **15**, 1513 (1989) [Sov. J. Plasma Phys. **15**, 881 (1989)].
37. *Handbook of Physical Quantities*, Ed. by I. S. Grigoriev and E. Z. Meilikhov (Énergoizdat, Moscow, 1991; CRC Press, Boca Raton, 1997).
38. C. Cason, J. E. Perkins, A. H. Werkheizer, and J. Duderstadt, AIAA J. **15**, 1079 (1977).
39. H. Bohringer and F. Arnold, Int. J. Mass Spectrom. Ion Phys. **49**, 61 (1983).
40. O. V. Kozlov, *Electrical Probe in Plasmas* (Atomizdat, Moscow, 1969).
41. P. M. Chung, L. Talbot, and K. J. Touryan, *Electric Probes in Stationary and Flowing Plasmas: Theory and Application* (Springer-Verlag, Berlin, 1975; Mir, Moscow, 1978).
42. B. V. Alekseev and V. A. Kotel'nikov, *Probe Technique of Plasma Diagnostics* (Énergoatomizdat, Moscow, 1988).
43. V. E. Fortov and I. T. Iakubov, *Physics on Nonideal Plasma* (Hemisphere, New York, 1990).
44. J. B. Pieper and J. Goree, Phys. Rev. Lett. **77**, 3137 (1996).
45. U. Konopka, L. Ratke, and H. M. Thomas, Phys. Rev. Lett. **79**, 1269 (1997).
46. U. Konopka, G. E. Morfill, and L. Ratke, Phys. Rev. Lett. **84**, 891 (2000).
47. O. Bystrenko and A. Zagorodny, Phys. Lett. A **255**, 325 (1999).
48. O. Bystrenko and A. Zagorodny, Phys. Lett. A **262**, 72 (1999).
49. G. Lapenta, Phys. Plasmas **6**, 1442 (1999).
50. G. Lapenta, Phys. Rev. E **62**, 1175 (2000).
51. V. V. Ivanov, A. F. Pal', T. V. Rakhimova, *et al.*, Zh. Éksp. Teor. Fiz. **115**, 2020 (1999) [JETP **88**, 1105 (1999)].
52. S. Alexander, P. M. Chaikin, P. Grant, *et al.*, J. Chem. Phys. **80**, 5776 (1984).
53. V. Yu. Baranov, I. A. Belov, A. V. Dem'yanov, *et al.*, in *Isotopes: Properties, Production, Applications*, Ed. by V. Yu. Baranov (AT, Moscow, 2000), p. 626.

Translated by O. E. Khadin

Plasma Physics Reports, Vol. 28, No. 1, 2002, pp. 40–45. Translated from Fizika Plazmy, Vol. 28, No. 1, 2002, pp. 45–50.
Original Russian Text Copyright © 2002 by Kondrat'ev, Matveenko.

PLASMA DYNAMICS

Plasma Acceleration Efficiency in a Pulsed Electrodynamic Accelerator

A. A. Kondrat'ev and Yu. I. Matveenko

Zababakhin All-Russia Research Institute of Technical Physics, Russian Federal Nuclear Center, Snezhinsk, Chelyabinsk oblast, 456770 Russia

Received May 5, 2001; in final form, July 26, 2001

Abstract—Results are presented from two-dimensional gas-dynamic simulations of plasma acceleration in the channel of a pulsed electrodynamic accelerator. The electrical conductivity of the plasma is assumed to be infinite and its thermal conductivity is neglected. The effect of the initial plasma density distribution on the acceleration efficiency is investigated. It is shown that the acceleration efficiency can be as high as ~40%, the acceleration length being one order of magnitude larger than the width of the initial gas density distribution. © *2002 MAIK "Nauka/Interperiodica".*

1. INTRODUCTION

Pulsed electrodynamic accelerators [1–3] are capable of producing plasmoids with an energy of about 100 kJ and a directed stream velocity of up to 10^8 cm/s. An accelerator of this type consists of two coaxial metal electrodes connected to a capacitor bank. The interelectrode gap is filled with a working gas. Pulsed electrodynamic accelerators can be divided into two classes depending on the manner in which the working gas is admitted into the interelectrode gap: systems in which the gap is entirely filled with the gas and systems in which the gas is localized near the entrance holes. The discharge of a bank of capacitors initiates an electrical breakdown of the gas and causes the formation of a current sheet, in which the plasma is accelerated by the gradient of the magnetic field pressure. Since, in vacuum, the magnetic field strength is inversely proportional to the radius, $B \propto 1/r$, the magnetic field pressure and, accordingly, the plasma motion velocity are higher near the internal electrode. As a result, the current sheet becomes inclined to the electrodes, leading to a radial redistribution of the plasma mass. Nevertheless, for the initial plasma density distribution with a half-width of 10 cm in a 160-cm-long accelerator with conical electrodes (the external electrode is between 80 and 30 cm in diameter, and the interelectrode distance increases from 3.6 to 7.2 cm), the plasma shell between the electrodes remains continuous and the acceleration efficiency is about 20% [3]. Stable acceleration is achieved by the use of so-called compact toroids [4] and is ensured by an additional poloidal magnetic field, which is frozen in the plasma of the forming toroid. However, such systems are not considered in our paper.

In electrodynamic models in which the plasma is regarded as an electrically conducting shell with a localized mass and in one-dimensional models reviewed by Kalmykov [1], the radial redistribution of the plasma mass in the accelerator channel is neglected. The dynamics of a plasma uniformly filling a ring-shaped channel of constant radius was considered in two-dimensional numerical studies of the plasma focus [5, 6] (Maxon and Eddleman [6] asserted that the results obtained by Potter [5] are erroneous). In those papers, the analysis was carried out with allowance for the finite electrical conductivity, thermal conductivity, and the temperature difference between the electrons and ions. The total current flowing through the plasma was determined by solving the electric-circuit equation. However, the acceleration efficiency, as well as the initial plasma density distributions of finite width that make it possible to achieve higher plasma stream velocities at a higher efficiency, was not studied.

The goal of our paper is to investigate the acceleration efficiency in systems filled entirely or locally with a plasma. We use a simplified model in which the plasma is completely ionized and perfectly conducting, the plasma thermal conductivity is neglected, and the total current through the accelerator is constant in time. This model corresponds to a sufficiently high plasma density, $n > 10^{16}$ cm^{-3}, at which the current sheet is opaque to the gas and a shock wave (SW) forms [1]. We study how the plasma dynamics is affected by the initial plasma density distribution and the accelerator dimensions. We also investigate the possibility of plasma acceleration over a distance one order of magnitude larger than the width of the initial gas density distribution.

2. METHOD FOR NUMERICAL SOLUTION

We treat the problem in the gas-dynamic approximation, assuming that the specific plasma resistivity is zero and neglecting plasma thermal conductivity, ion-

1063-780X/02/2801-0040$22.00 © 2002 MAIK "Nauka/Interperiodica"

ization kinetics, and the effects associated with different electron and ion velocities. We solve the following set of equations:

$$\frac{\partial \rho}{\partial t} + \nabla \cdot (\rho \mathbf{v}) = 0,$$

$$\frac{\partial (\rho \mathbf{v})}{\partial t} + \nabla \cdot (\rho \mathbf{v} \cdot \mathbf{v}) = -\nabla p + [\nabla \times \mathbf{B}] \times \mathbf{B},$$

$$\frac{\partial (\rho \varepsilon)}{\partial t} + \nabla \cdot (\rho \varepsilon \mathbf{v}) = -p \nabla \cdot \mathbf{v},$$

where ρ is the density, $\mathbf{v}$ is the velocity, $\mathbf{B}$ is the magnetic field, p is the pressure, and ε is the specific internal energy. We use the equation of state for an ideal gas, $p = (\gamma - 1)\rho\varepsilon$, with the adiabatic index $\gamma = 5/3$. The set of equations is written in dimensionless form. The main dimensional units are taken to be those of length, density, and magnetic field. The problem is assumed to be axisymmetric ($\partial/\partial\varphi = 0$) and is treated in two-dimensional geometry. The magnetic field inside the plasma is absent because of the infinite electrical conductivity of the plasma. Outside the plasma, the magnetic field $\mathbf{B} = (0, 0, B_\varphi)$ is created by the currents flowing along the plasma surface and in the electrodes. The plasma surface is a contact boundary (CB) between the plasma and vacuum. The absorption of the plasma by the electrodes is neglected, and the velocity vector component perpendicular to the electrode surfaces is set equal to zero.

The Eulerian approach allows us to calculate highly deformed plasma streams, which cannot be calculated by regular Lagrangian methods without readjustment of the numerical grid. For this reason, the basic set of equations is solved on a fixed rectangular grid. The values of the density, pressure, specific internal energy, and magnetic field refer to the centers of the cells of the difference grid, while the values of the velocity vector components refer to the centers of the cell boundaries. The vacuum regions are explicitly distinguished by the volume density method [7]. This method implies that each cell of the difference grid is assigned the relative volume plasma concentration $0 \le \beta \le 1$, which is equal to the ratio of the plasma volume in the cell to the cell volume. The cells with zero relative concentration ($\beta = 0$) are treated as vacuum cells, in which the magnetic field is calculated from the formula $B(r) = B_0 r_0/r$. The contact boundary passes through the cells with $0 < \beta < 1$, in which the plasma density is calculated from the volume actually occupied by the plasma.

At each time step, the basic set of equations is solved in two stages. In the first stage, the equations are solved in Lagrangian variables using an implicit, completely conservative difference scheme [8]. In the second stage, the velocity, density, and internal energy found in the first stage are used to compute the fluxes of the plasma volume, mass, momentum, and total energy (i.e., the sum of kinetic and internal energies) through the boundaries of the fixed cells by an explicit scheme of first-order accuracy. The plasma fluxes from the cell are calculated based on the analysis of the plasma density in the neighboring cells [7]. Then, the density, velocity, and internal energy are calculated from the laws of mass, energy, and momentum conservation using the previously calculated fluxes. An analogous two-stage approach to finding the solution is used in the coarse particle method [9]. However, our approach to solving the basic equation in the first stage is based on a difference scheme other than that applied in [9]. The above difference scheme is completely conservative [8] and ensures first-order accuracy in both space and time. In all calculations, the sizes of the grid cells were $\Delta z = 2.5 \times 10^{-3}$ in the axial direction and $\Delta r = 1.25 \times 10^{-3}$ in the radial direction.

3. CALCULATED RESULTS

The electrodynamic accelerator under investigation consists of two coaxial cylindrical electrodes with a plasma between them. The calculations were performed for the external electrode radius $R_1 = 1$ and different values of the internal electrode radius R_2. Initially, the plasma–vacuum CB is the $z = 0$ plane. A constant magnetic field $B(r) = B_0/r$ is applied within the left half-space $z < 0$; the calculations were carried out for $B_0 = 1$. The same field was specified in the vacuum cells that appear in the right half-space $z > 0$ during the plasma motion. The acceleration efficiency $\eta = E_K/E_S$ was determined as the ratio of the plasma kinetic energy E_K to the total energy of the magnetic field and plasma, $E_S = E_B + E_K + E_I$, where E_B is the energy of the magnetic field between the $z = 0$ plane and the CB and E_I is the plasma internal energy.

3.1. Accelerator with a Continuous Uniform Plasma Filling

Let a plasma with the density $\rho_0 = 1$ and pressure $p_0 = 6 \times 10^{-6}$ fill the half-space $z > 0$. In the limit $\Delta R = R_1 - R_2 \longrightarrow 0$, the motion is one-dimensional and the solution to the relevant equations describes a shock wave propagating in the plasma. In the limit $p_0 \ll B_0^2/2$, the shock front velocity D and plasma velocity U are equal to

$$D = \frac{V_a \sqrt{\gamma + 1}}{2}, \quad U = \frac{V_a}{\sqrt{\gamma + 1}}, \quad V_a = \frac{B_0}{\sqrt{\rho_0}}. \quad (1)$$

The propagation velocity of the CB is equal to the plasma velocity U, and the plasma pressure in the SW is equal to the magnetic field pressure, $p = B_0^2/2$. The specific internal energy in the SW is equal to the specific kinetic energy, $\varepsilon = U^2/2$. The magnetic field energy E_B is equal to the sum of the internal (E_I) and kinetic (E_K) energy of the plasma occupying the region

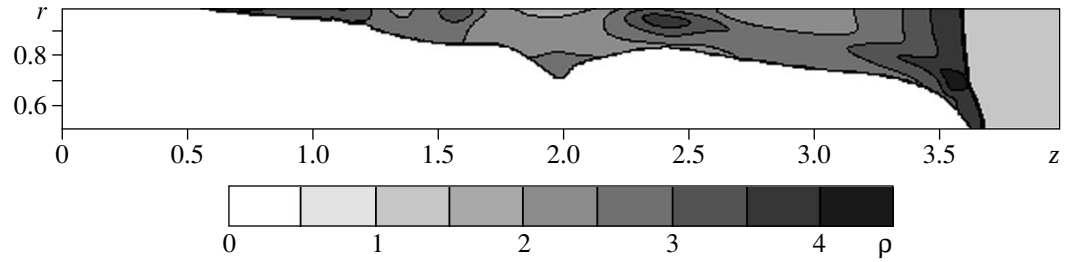

Fig. 1. Plasma density distribution in the interelectrode gap at the time $t = 2.4$ in an accelerator with a uniform initial plasma filling and an internal electrode of radius $R_2 = 0.5$.

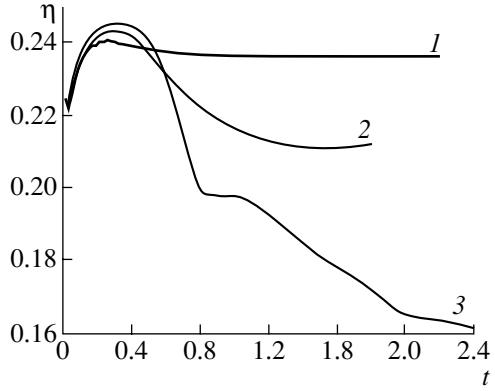

Fig. 2. Time evolutions of η for R_2 = (*1*) 0.9, (*2*) 0.75, and (*3*) 0.5 in an accelerator with a uniform initial plasma filling.

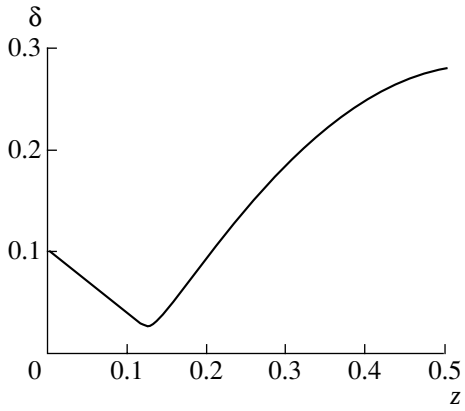

Fig. 3. Time evolution of the plasma shell thickness δ in an accelerator with a uniform initial plasma filling.

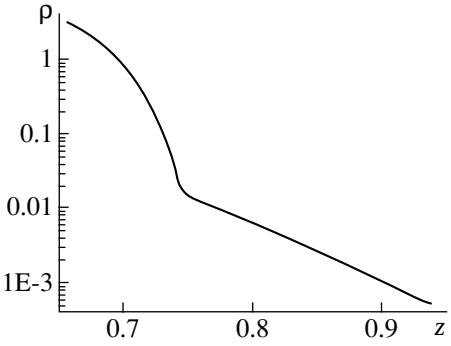

Fig. 4. Profile of the plasma density ρ along the *z*-axis at the time $t = 0.5$ in an accelerator with a uniform initial plasma filling.

between the CB and the shock front. Consequently, in a narrow interelectrode gap ($\Delta R/R_1 \ll 1$), the acceleration efficiency is equal to $\eta = 1/4$. In a finite-width gap, the plasma mass is redistributed as is shown in Fig. 1 and the acceleration efficiency is lower. A significant portion of the plasma is accumulated near the external electrode and has a low (in comparison with U) velocity. For $R_2 = 0.5$, the width of the plasma layer accelerated near the internal electrode by the time $t = 2.4$ is equal to 0.05, which is much smaller than $(D - U)t = 0.98$. This is attributed to both the inclination of the CB to the electrodes and the radial plasma flow toward the external electrode. Because of this flow, a smaller amount of the plasma is accelerated and, accordingly, the plasma velocity increases. By this time, the velocity v_c of the CB near the internal electrode is equal to $v_c = 1.6$, which is higher than the value $U = 1.22$ obtained from formula (1). Figure 2 shows time evolutions of the acceleration efficiency η for several values of R_2. For a relatively narrow interelectrode gap ($\Delta R/R_1 = 0.1$), the efficiency is close to that obtained in the one-dimensional model and is seen to decrease slowly with time. For $\Delta R/R_1 = 0.5$, the acceleration efficiency decreases rapidly as time elapses, because the plasma moving at a relatively low velocity is accumulated near the external electrode.

3.2. Accelerator with a Finite-Width Initial Plasma Density Distribution

All numerical results presented below were obtained for an internal electrode with the radius $R_2 = 0.9$ and for a plasma with a free right boundary (the corresponding boundary condition is $p = 0$), the width of the initial plasma density distribution being Δz. First, we describe the results obtained for a homogeneous plasma with the density $\rho = 1$. The results from one-dimensional simulations (the plasma moves only in the axial direction) are illustrated in Fig. 3, which shows how the plasma shell thickness δ evolves in time at the radius $r = 1$. Before the SW reaches the right plasma boundary (this occurs at the time $t = 0.12$), the plasma dynamics is the same as in an accelerator with a semi-infinite plasma filling. After the SW reaches the right plasma boundary, the velocity of the right boundary

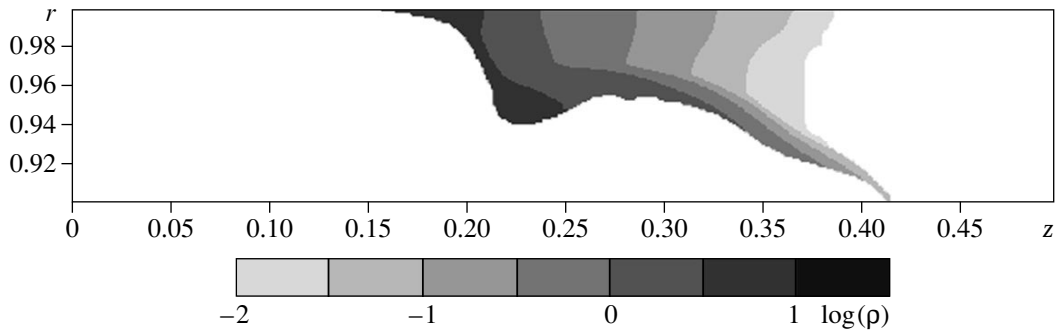

Fig. 5. Plasma density distribution in the interelectrode gap at the time $t = 0.259$ in an accelerator in which the width of the initial uniform plasma density distribution is $\Delta z = 0.1$.

becomes higher than that of the left boundary and the plasma shell thickness increases. This case is illustrated by Fig. 4, which shows the z-profile of the plasma density. The results of two-dimensional calculations also show that the plasma shell thickness increases after the SW reaches the right plasma boundary. However, after a certain time interval, the shell thickness stops increasing and starts decreasing. As a result, at a certain time, the plasma shell in the interelectrode gap becomes discontinuous: it detaches from the internal electrode (Fig. 5). This effect is caused by the radial plasma flow toward the external electrode. For the initial plasma density distribution with the width $\Delta z = 0.1$, the coordinate of the point of detachment is $z = 0.42$, and, for the initial distribution having two times that width, this coordinate is $z = 0.63$. For $\Delta z = 0.3$, we have $z = 0.92$. The time evolution of the acceleration efficiency η is shown in Fig. 6. Before the SW reaches the right (free) plasma boundary, the efficiency evolves in the same manner as in an accelerator with a semi-infinite plasma filling. After the SW reaches the right plasma boundary, the plasma heating terminates and the acceleration efficiency η starts to increase, reaching the value $\eta = 0.425$ (for the initial plasma density distribution with the width $\Delta z = 0.1$) by the time at which the plasma detaches from the internal electrode.

Also, we considered a plasma with the initial density distribution

$$\rho(z) = \begin{cases} \exp[-(z-2a)^2/a^2], & 0 \le z \le 4a \\ 0, & \text{in the remaining region,} \end{cases} \qquad (2)$$

with the parameter $a = 0.2$. The acceleration of such a plasma is different from what takes place in the previous case in that the specific internal energy in a propagating SW increases at the decreasing part of the plasma density distribution ($z > 2a$). After the SW reaches the right plasma boundary, the velocity of the right boundary becomes substantially higher than that of the left boundary and the plasma shell thickness increases to a much greater extent in comparison with that in the case of an accelerator filled uniformly with a plasma. As a result, the plasma shell in the interelectrode gap becomes discontinuous after a far longer time and the plasma passes a distance that is much larger than the width of its initial density distribution. The plasma shell becomes discontinuous at the point $z = 2.9$ at the time $t = 1.0$ (Fig. 7). It is of interest to note that a discontinuity occurs at the center of the interelectrode gap rather than at the internal electrode (as is the case in an accelerator filled uniformly with a plasma). For the problem at hand, the plasma dynamics is illustrated by Fig. 8 and the time evolution of η is shown in Fig. 9. A decrease in the acceleration efficiency in the initial stage is associated with the propagation of the CB in the direction in which the plasma density increases. After the CB passes through the region with the highest density, the acceleration efficiency starts to increase, reach-

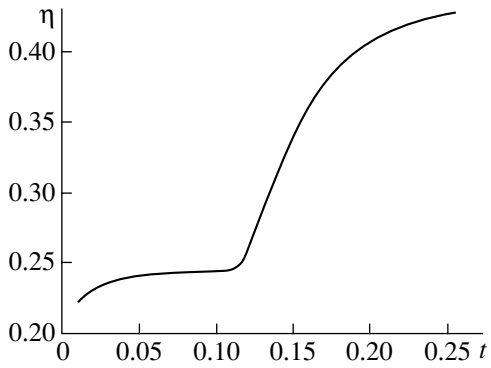

Fig. 6. Time evolution of the acceleration efficiency η in an accelerator in which the width of the initial uniform plasma density distribution is $\Delta z = 0.1$ and the radius of the internal electrode is $R_2 = 0.9$.

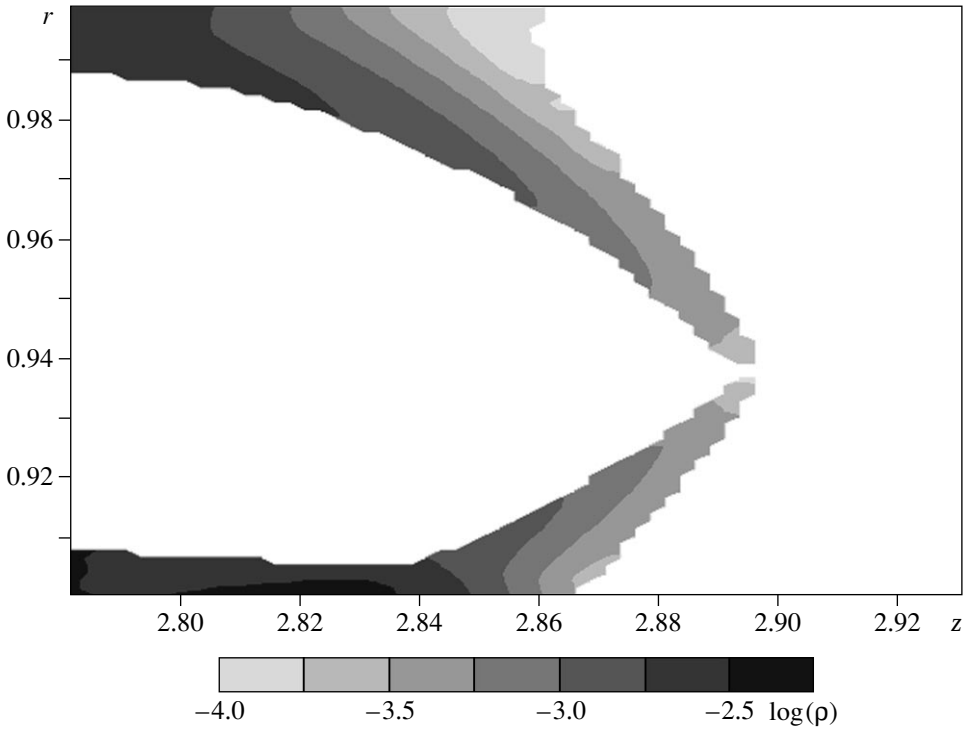

Fig. 7. Plasma density distribution in the interelectrode gap at the time $t = 1.0$ in an accelerator with the initial plasma density distribution (2).

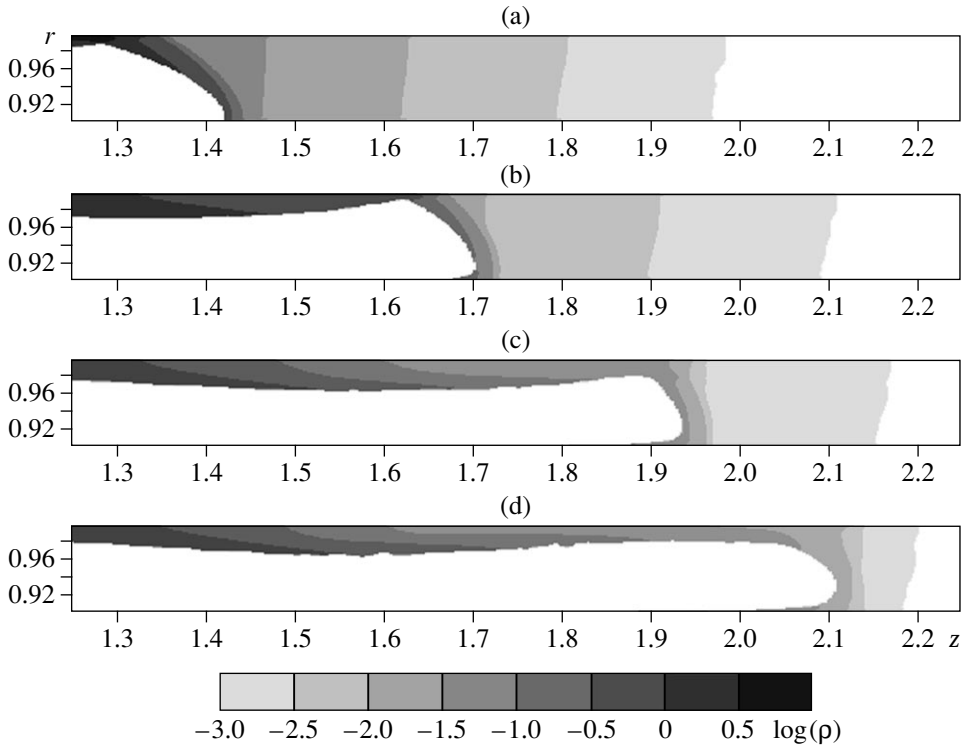

Fig. 8. Plasma dynamics in the interelectrode gap in an accelerator with the initial plasma density distribution (2): t = (a) 0.91, (b) 0.95, (c) 0.97, and (d) 0.98.

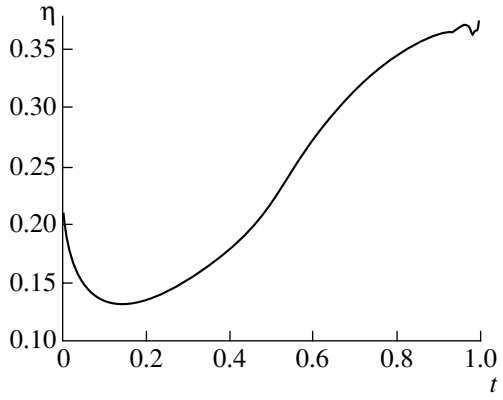

Fig. 9. Time evolution of the acceleration efficiency η in an accelerator with the initial plasma density distribution (2).

ing the value $\eta = 0.37$ by the time at which the plasma shell becomes discontinuous.

4. CONCLUSION

In an accelerator in which the interelectrode gap is continuously and uniformly filled with a plasma, the acceleration efficiency is lower than 25% because of the strong plasma heating by the SW. In accelerators with thicker interelectrode gaps, the acceleration efficiency is far lower because of the presence of radial plasma flow and the small thickness of the accelerated plasma. In an accelerator with a finite-width initial plasma density distribution, the acceleration efficiency can be as high as ~40%; however, the plasma shell becomes discontinuous at a certain distance from the initial CB position. The distance by which the initial plasma is displaced before the discontinuity occurs depends on the shape of the plasma density distribution and may be much larger than its initial width.

ACKNOWLEDGMENTS

This work was supported in part by the International Science and Technology Center, project no. 78.

REFERENCES

1. A. A. Kalmykov, in *Physics and Application of Plasma Accelerators* (Nauka i Tekhnika, Minsk, 1974), p. 48.
2. V. V. Sidnev, Yu. V. Skvortsov, N. M. Umrikhin, and F. R. Khamidullin, Vopr. At. Nauki Tekh., Ser. Termoyad. Sintez **2**, 12 (1983).
3. V. V. Sidnev, Yu. V. Skvortsov, V. G. Solov'eva, and N. M. Umrikhin, Fiz. Plazmy **10**, 392 (1984) [Sov. J. Plasma Phys. **10**, 230 (1984)].
4. R. Raman, J. C. Thomas, D. Q. Hwang, *et al.*, Fusion Technol. **24**, 239 (1993).
5. D. E. Potter, Phys. Fluids **14**, 1911 (1971).
6. S. Maxon and J. Eddleman, Phys. Fluids **21**, 1856 (1978).
7. A. A. Shanin and Yu. V. Yanilkin, Vopr. At. Nauki Tekh., Ser. Mat. Model. Fiz. Protses. **1**, 24 (1993).
8. A. A. Samarskiĭ and Yu. P. Popov, *Difference Methods for Solving Gas Dynamics Problems* (Nauka, Moscow, 1977).
9. O. M. Belotserkovskiĭ and Yu. M. Davydov, *Coarse Particle Method in Gas Dynamics* (Nauka, Moscow, 1982).

Translated by O. E. Khadin

Plasma Physics Reports, Vol. 28, No. 1, 2002, pp. 46–56. Translated from Fizika Plazmy, Vol. 28, No. 1, 2002, pp. 51–61.
Original Russian Text Copyright © 2002 by Shalashov, Suvorov.

PLASMA KINETICS

Modeling of Coulomb Collisions in a Kinetic Description of the Electron Cyclotron Resonance Plasma Heating

A. G. Shalashov and E. V. Suvorov

Institute of Applied Physics, Russian Academy of Sciences, ul. Ul'yanova 46, Nizhni Novgorod, 603600 Russia

Received March 1, 2001; in final form, August 20, 2001

Abstract—The electron distribution function is modeled numerically with allowance for Coulomb collisions and quasilinear effects under cyclotron resonance conditions by solving a two-dimensional kinetic equation containing the quasilinear diffusion operator and the Coulomb collision operator in the Landau form. Two simplified model collision integrals that make it possible to describe electron heating by microwave radiation are considered. The first model collision operator is obtained by introducing the parametric time dependence of the temperature of the background Maxwellian electrons into the linear collision integral. It is shown that the heating of the bulk electrons can be described in a noncontradictory way if the temperature dynamics of the background electrons is calculated from the equation of energy balance, which is governed by the amount of the microwave power absorbed by the resonant electrons with the distribution function modified due to quasilinear effects. This conclusion is confirmed in a more rigorous fashion by comparing the solutions obtained using the first model Coulomb collision integral with those obtained using the second model integral, namely, the nonlinear operator derived by averaging the distribution function of the scattering electrons over pitch angles. The time-dependent linear collision integral is used to obtain analytic solutions describing quasi-steady electron heating with allowance for the quasilinear degradation of microwave power absorption. © *2002 MAIK "Nauka/Interperiodica".*

1. INTRODUCTION

In present-day magnetic-confinement-fusion experiments on electron cyclotron resonance (ECR) heating of plasmas and ECR current drive, the microwave power can be so high that the deviation of the distribution function of resonant electrons from an equilibrium one leads to a significant change in the microwave power deposition profiles. Thus, the absorption of electron cyclotron waves in a collisionless plasma will eventually result in the formation of a quasilinear plateau in the electron distribution function (EDF) in the resonance region of the electron phase space, in which case the plasma becomes transparent to microwave radiation and the heating terminates [1]. In actual experiments, this is, of course, not the case because the quasi-steady distribution function of resonant electrons that forms under the action of their Coulomb collisions with nonresonant electrons has no plateaulike region, so that a certain amount of microwave power is always deposited in the plasma. Another effect of Coulomb collisions is that they cause the perturbations of the distribution function to expand from the local energy deposition region in velocity space into the entire phase space, thereby resulting in the heating of the bulk of electrons.

In most cases, the evolution of the EDF in phase space during intense heating can be described by a Fokker–Planck equation that contains the so-called quasilinear diffusion operator, which accounts for the interaction of resonant electrons with the microwave field, and the Coulomb collision operator (see, e.g., reviews [2, 3]). In most schemes for ECR plasma heating (e.g., those with a quasi-transverse low-field-side launching of a microwave beam into a toroidal device), the resonant cyclotron interaction is localized in the thermal region of the electrons velocity space, in which case it is necessary to use the exact nonlinear electron–electron (e–e) collision operator. However, the problem formulated in such a way is often too cumbersome for numerical analysis and, in some cases, is an unnecessary complication. Here, we consider two ways of simplifying the binary Coulomb collision integral in the Landau form [1–4]. We use as an example the spatially homogeneous kinetic equation describing the dynamics of the EDF during electron heating by a given packet of electron cyclotron waves propagating transverse to the magnetic field. We neglect possible mechanisms for energy and particle losses, including electron–ion (e–i) energy exchange, and assume that the plasma electrons are heated on a time scale much shorter than the energy confinement time.

2. FORMULATION OF THE PROBLEM

We consider a spatially homogeneous quasilinear kinetic equation describing the dynamics of the EDF averaged over the phase of gyration in a constant mag-

1063-780X/02/2801-0046$22.00 © 2002 MAIK "Nauka/Interperiodica"

netic field and over the "rapid" electron oscillations in a microwave field:

$$\frac{\partial f}{\partial t} = L_{\text{coll}} f + L_{ql} f, \tag{1}$$

where L_{coll} is the Coulomb collision operator and L_{ql} is the quasilinear diffusion operator. The operators are defined in the two-dimensional space of electron velocities (because of the averaging over the phase of the electron cyclotron gyration) and have the Fokker–Planck form. However, none of the coordinate systems provide a simultaneous separation of variables in both the quasilinear diffusion and Coulomb collision operators. In fact, the quasilinear diffusion operator is of a diagonal form in the "cylindrical" variables ($v_\perp$, $v_\parallel$), where $v_\perp$ and $v_\parallel$ are the electron velocity components perpendicular and parallel to the magnetic field, while the simplified collision operators (which will be analyzed below) are of a diagonal form in the "spherical" variables (v, θ), where v is the absolute value of the electron velocity and θ is the electron pitch angle (the angle between the electron velocity vector and the magnetic field direction). In this paper, the quasilinear diffusion operator often (but not always) plays the role of a small correction to the Coulomb collision operator, because the quasilinear diffusion occurs only in a limited region of electron phase space and it is assumed that the plasma is not too rarefied. For this reason, it is more convenient to write the kinetic equation in a spherical coordinate system, in which the collision operator takes the simplest form and the quasilinear diffusion operator contains mixed partial derivatives.

We are interested in such solutions to Eq. (1) that correspond to the initial Maxwellian EDF with temperature T_{e0} and density N_e. We assume that the EDF $f(t, u, \mu)$ normalized to $N_e(m_e/2\pi T_{e0})^{3/2}$ depends on the three variables: the time t; the absolute value $u = v/v_{e0}$ of the dimensionless electron velocity (normalized to the initial electron thermal velocity $v_{e0} = \sqrt{2T_{e0}/m_e}$); and the cosine of the electron pitch angle, $\mu = \cos\theta$. In dimensionless variables, the initial condition takes the form:

$$f|_{t=0} = \exp(-u^2). \tag{2}$$

If the heating radiation propagates strictly transverse to the external magnetic field, the EDF is even in the angular variable μ, so that it is sufficient to consider the EDF in the region ($0 < u < \infty$, $0 < \mu < 1$) and to impose the boundary conditions

$$f|_{u=\infty} = 0, \quad \partial f/\partial\mu|_{\mu=0} = 0. \tag{3}$$

The boundaries $u = 0$ and $\mu = 1$ are associated with the use of spherical coordinates rather than with the very nature of the problem. When the original problem is formulated in a natural way, it is sufficient to require that the derivatives of the EDF at these boundaries be finite.

As an example, we consider the following model problem. We assume that the plasma is heated by a given steady-state noise packet of electron cyclotron waves with the simplest possible distribution of the spectral intensity I_ω, which is assumed to be constant in a certain frequency range:

$$I_\omega = \begin{cases} I_0, & \omega \in (\omega_1, \omega_2) \\ 0, & \omega \notin (\omega_1, \omega_2) \end{cases}, \quad I_0 = \text{const}. \tag{4}$$

An analogous distribution can be used, in particular, to model ECR plasma heating by monochromatic microwave radiation at a certain magnetic surface inside the toroidal plasma column, in which case the effective broadening of the heating radiation spectrum is associated with the variation of the resonant electron gyrofrequency at the intersection of a quasi-optical microwave beam with the magnetic surface [5, 6]. We assume that all modes of the heating radiation propagate in the same direction, strictly transverse to the external magnetic field. In this case, the resonant cyclotron interaction gives rise to the electron diffusion over transverse velocities and the quasilinear diffusion operator is usually represented in cylindrical variables as [1–3, 5, 6]

$$L_{ql} f \equiv \frac{1}{u_\perp}\frac{\partial}{\partial u_\perp}\left\{ u_\perp D_{ql}\frac{\partial}{\partial u_\perp} f(u_\perp, u_\parallel)\right\}, \tag{5}$$

where $u_\perp = u\sqrt{1-\mu^2}$ and $u_\parallel = u\mu$. In spherical coordinates, expression (5) takes the form

$$L_{ql} f = \frac{1}{u^2}\left\{\frac{\partial}{\partial u}\left[u^2(1-\mu^2)D_{ql}\frac{\partial f}{\partial u}\right]\right.$$
$$-\frac{\partial}{\partial u}\left[u\mu(1-\mu^2)D_{ql}\frac{\partial f}{\partial \mu}\right] - \frac{\partial}{\partial \mu}\left[u\mu(1-\mu^2)D_{ql}\frac{\partial f}{\partial u}\right] \tag{6}$$
$$\left. + \frac{\partial}{\partial \mu}\left[\mu^2(1-\mu^2)D_{ql}\frac{\partial f}{\partial \mu}\right]\right\}.$$

In the lowest non-trivial order in an expansion in $v/c \ll 1$, the quasilinear diffusion coefficient is approximately equal to [1]

$$D_{ql} = \nu_{ql}\begin{cases} u^{m+n}\mu^m(1-\mu^2)^{n/2}, & |u-u_0| \le \Delta u \\ 0, & |u-u_0| > \Delta u. \end{cases} \tag{7}$$

Here, $\nu_{ql} \simeq \pi^2 e^2 c^{-3} m_e^{-2} \tilde{n} I_0$ is the "quasilinear" frequency, where $\tilde{n}$ is the refractive index multiplied by the polarization factor for the transversely propagating waves under consideration. The region in phase space $u \in (u_0 - \Delta u, u_0 + \Delta u)$, in which the quasilinear diffu-

sion operator is nonzero, is determined by the relativistic resonance condition

$$\omega_{\text{res}} = s\omega_H\sqrt{1-u^2v_{e0}^2/c^2} \in (\omega_1, \omega_2), \tag{8}$$

where s is the number of the cyclotron mode, ω_H is the nonrelativistic electron gyrofrequency, and c is the speed of light in free space. To be specific, in what follows, we assume that the plasma is heated by an extraordinary wave at the second harmonic of the electron cyclotron frequency; this corresponds to $m = 0$ and $n = 2$ (for an ordinary wave at the fundamental harmonic of the electron cyclotron frequency, we have $m = 2$ and $n = 0$).

Since the characteristic electron velocity is much higher than the ion velocity, the e–i part of the Coulomb collision operator contributes only to the pitch angle scattering and the Landau collision integral can be represented as [2, 7, 8]

$$L_{\text{coll}}f = L_{\text{coll}}^{ee}[f, f] + \frac{1}{2}Z_{\text{eff}}\nu_{ee}(u)\frac{\partial}{\partial\mu}(1-\mu^2)\frac{\partial f}{\partial\mu},$$
$$\nu_{ee}(u) = \frac{\nu_0}{u^3}, \quad \nu_0 = \frac{4\pi e^4 N_e \ln\Lambda_e}{m_e^2 v_{e0}^3}, \tag{9}$$

where $L_{\text{coll}}^{ee}[f, f]$ is the e–e part of the collision operator, $\nu_{ee}(u)$ is the transport rate of e–e collisions, the inverse time ν_0 of thermal collisions corresponds to the initial electron temperature, and $Z_{\text{eff}} = \sum Z_i^2 N_i/N_e$ is the effective ion charge number. The two methods that will be used below to provide a simplified description of electron heating by the quasilinear equation are based on the replacement of the exact e–e collision integral by a simpler operator that describes how the EDF is modified due to collisions between resonant electrons and an effective ensemble of the background electrons with a simplified velocity distribution function.

One of the most common and natural ways of simplifying the collision integral is to linearize it under the assumption that the perturbed EDF differs from the equilibrium Maxwellian function f_M only slightly:

$$L_{\text{coll}}^{ee}[f, f] \approx L_{\text{coll}}^{ee}[f_M, f - f_M] + L_{\text{coll}}^{ee}[f - f_M, f_M]. \tag{10}$$

Moreover, the perturbation $f - f_M$ in this formula can be replaced with the EDF f itself, because, for the equilibrium electron distribution, we have $L_{\text{coll}}^{ee}[f_M, f_M] = 0$. The first term on the right-hand side of formula (10) describes the modification of the EDF due to collisions of nonequilibrium electrons with Maxwellian electrons, and the second term accounts for the correction introduced by collisions of background electrons with nonequilibrium electrons. In fact, the second term is important only when an ordered macroscopic motion is driven in the plasma, in which case it describes the cancellation of the frictional force between the main and background components [2]:

$$\int L_{\text{coll}}^{ee}[f_M, f - f_M]\mathbf{v}d^3\mathbf{v} + \int L_{\text{coll}}^{ee}[f_M - f_M, f_M]\mathbf{v}d^3\mathbf{v} = 0. \tag{11}$$

In the case of transverse launching of microwaves into the plasma, when no currents are excited in the plasma, each of the terms in Eq. (11) equals zero, and the EDF is perturbed in a fairly localized resonance region. In this case, the change in the background electron collisions can be neglected, so that we arrive at the linear collision operator corresponding to the first term in expression (10) [2, 7, 8]. With the possible electron heating in mind, we represent the Maxwellian distribution function of the background electrons as

$$f_M = (T_{e0}/T_e)^{3/2}\exp(-u^2T_{e0}/T_e), \tag{12}$$

where the electron temperature T_e is time-dependent. Then, the operator describing collisions of electrons with the Maxwellian core takes the form

$$L_{\text{col}}^{ee}[f_M, f] = \frac{1}{u^2}\frac{\partial}{\partial u}u^2\left[D_{ee}(u)\frac{\partial f}{\partial u} + F_{ee}(u)f\right] + \nu_{ee}^{\mu}(u)\frac{\partial}{\partial\mu}(1-\mu^2)\frac{\partial f}{\partial\mu}, \tag{13}$$

where

$$D_{ee}(u) = \frac{T_e}{T_{e0}}\frac{F_{ee}(u)}{2u},$$
$$F_{ee}(u) = u\nu_{ee}(u)\frac{4}{\sqrt{\pi}}\int_0^w e^{-s^2}s^2 ds, \quad w = u\sqrt{T_{e0}/T_e}, \tag{14}$$

$$\nu_{ee}^{\mu}(u) = \nu_{ee}(u)\frac{1}{\sqrt{\pi}}\left[we^{-w^2} + (2-w^{-2})\int_0^w e^{-s^2}s^2 ds\right]. \tag{15}$$

In expressions (13)–(15), all of the coefficients also depend on the background electron temperature.

Omitting the second term in formula (10) also allows us to overcome additional numerical difficulties associated with the fact that the solutions to the kinetic equation cease to be positively defined [2]. However, when describing the heating processes by the linear collision integral (13), it is necessary to take into account the fact that this operator does not generally ensure the conservation of electron energy. Thus, if we assume that the temperature and density of the background plasma are both fixed, then the solutions to the kinetic equation will approach a steady state in which the absorbed microwave power is nonzero, while the *physical* energy sinks are absent. In order to avoid this situation, we refine the linear collision integral by introduc-

ing the parametric dependence of the temperature of the background Maxwellian EDF on time, $T_e = T_e(t)$. This parametric dependence is to be determined from the energy balance in the plasma–microwave field system. We assume that the total absorbed microwave power P_{abs} is eventually deposited in the background plasma; this assumption leads to the energy balance equation

$$\frac{3}{2}\frac{d}{dt}N_e T_e(t) = P_{\text{abs}}(t),$$
$$P_{\text{abs}}(t) = \int \frac{1}{2} m v^2 L_{ql} f d^3\mathbf{v}. \tag{16}$$

Using the explicit expression (6) for the quasilinear diffusion operator, we integrate Eq. (16) by parts to obtain

$$P_{\text{abs}}(t) = N_e T_{e0}\frac{8}{\sqrt{\pi}} \times \int_{u_0-\Delta u+0}^{u_0+\Delta u-0} du \int_0^1 d\mu u^2(1-\mu^2) D_{ql}(u,\mu)\left(-u\frac{\partial f}{\partial u} + \mu\frac{\partial f}{\partial \mu}\right). \tag{17}$$

The kinetic equation with the collision operator so defined has no steady-state solutions; instead, it has quasisteady solutions that describe an increase in the energy of the bulk electrons in the absence of energy losses.

Another way to derive an approximate e–e collision operator is to simplify the exact collision integral under the assumption that the distribution of the background electrons is isotropic in velocity space. Let us consider a reduced collision integral in which the distribution function of the scattering electrons is averaged over the pitch angles, $F(u) = \int_0^1 f(u,\mu)d\mu$. In explicit form, this operator can be deduced by the Rosenbluth potential technique [2, 7, 8]; as a result, we arrive at an operator differing from the linear operator only in that the coefficients in front of the derivatives are integral functions of the averaged EDF:

$$L_{\text{coll}}^{ee}[F, f] = \frac{1}{u^2}\frac{\partial}{\partial u}u^2\left[\tilde{D}_{ee}(u)\frac{\partial f}{\partial u} + \tilde{F}_{ee}(u) f\right] + \tilde{\nu}_{ee}^{\mu}(u)\frac{\partial}{\partial \mu}(1-\mu^2)\frac{\partial f}{\partial \mu}, \tag{18}$$

where

$$\tilde{D}_{ee}(u) = \nu_{ee}(u)\frac{4}{3\sqrt{\pi}}\left(\int_0^u u'^4 F(u')du' + u^3\int_u^\infty u' F(u')du'\right), \tag{19}$$

$$\tilde{F}_{ee}(u) = u\nu_{ee}(u)\frac{4}{\sqrt{\pi}}\int_0^u u'^2 F(u')du', \tag{20}$$

$$\tilde{\nu}_{ee}^{\mu}(u) = \nu_{ee}(u)\frac{4}{\sqrt{\pi}}\left[\frac{1}{2}\int_0^u u'^2 F(u')du' - \frac{1}{6u^2}\int_0^u u'^4 F(u')du' + \frac{u}{3}\int_u^\infty u' F(u')du'\right]. \tag{21}$$

This nonlinear operator can easily be incorporated in the existing computational schemes based on the linear collision integral. An obvious advantage of nonlinear operator (18) is that it automatically conserves the electron energy (this property is a consequence of the analogous property of the exact collision integral $L_{\text{coll}}^{ee}[F, F]$). For an isotropic EDF, operator (18) coincides with the exact Landau collision integral. Note that the dependence of the EDF on the pitch angle variable can be neglected for a plasma exhibiting a high degree of isotropy associated, e.g., with elastic collisions of electrons with multicharged ions (such that $Z_{\text{eff}} \gg 1$).

Below, we present the results of numerical investigation of the two-dimensional kinetic equation with the above collision integrals. The method for solving the kinetic equation numerically [9] is based on the results of [10, 11]. Note that, since it is impossible to simultaneously separate the variables in the quasilinear diffusion and Coulomb collision operators, the problem as formulated is somewhat more difficult to solve than the traditional diffusion problem.

3. FORMATION OF A QUASILINEAR PERTURBATION OF THE EQUILIBRIUM EDF

Numerical simulations show that, if the microwave field is strong enough for the quasilinear effects to be pronounced, then we can distinguish two stages of the interaction of microwaves with electrons. In the first stage, a plateaulike perturbation appears fairly rapidly in the EDF in the resonance region in phase space; during this process, the total electron energy increases insignificantly. In the second, slower, stage of "quasisteady" heating, the energy of the background electrons increases and qualitative changes in the shape of the EDF are insignificant.

In order to describe how the EDF deforms in the initial stage, it is sufficient to employ the kinetic equation with the simplest linear collision integral (13) and assume that the temperature of the background plasma is unchanged. The results of the relevant simulations carried out for a sufficiently strong microwave field are illustrated in Fig. 1a. The initial stage begins with a rapid equalization of the EDF over transverse electron energy throughout the resonance region. At the boundaries of this region, the gradients of the EDF become very steep, while, outside the resonance region, the EDF is perturbed only slightly. The steepening of the gradients of the EDF at the boundaries of the resonance region gives rise to a collisional electron flux, resulting

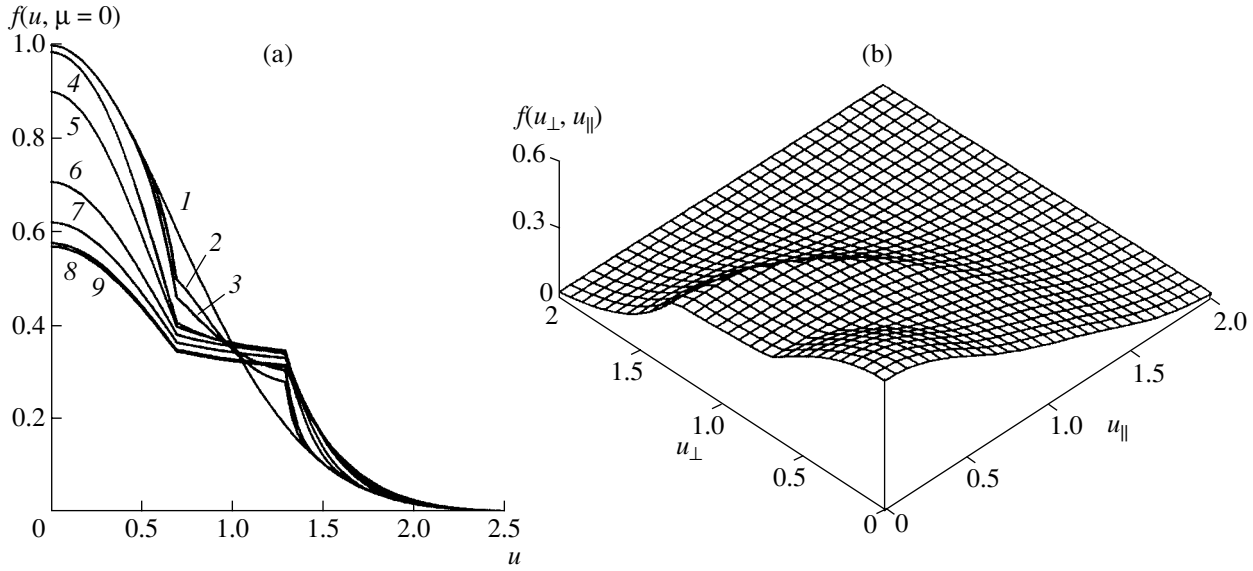

Fig. 1. Solutions to the kinetic equation with the linear collision integral at a fixed temperature of the background electrons: (a) plots of the function $f(t, u, \mu = 0)$ at successive times $\nu_0 t$ = (*1*) 0, (*2*) 0.01, (*3*) 0.02, (*4*) 0.1, (*5*) 0.2, (*6*) 0.5, (*7*) 1, (*8*) 3, and (*9*) 5 and (b) the relief of the steady-state EDF. The pump microwave field intensity corresponds to $\nu_{ql}/\nu_0 = 3$, the parameters of the resonance region are $u_0 = 1$ and $\Delta u = 0.3$, and the effective ion charge number is $Z_{\text{eff}} = 1$.

in a far slower process that leads to the increase in the electron energy. In this case, the quasilinear diffusion operator can be regarded as a kind of "pump," which initiates the electron flux through the resonance region from the low-velocity to the high-velocity range. This effect takes place in a wide range of microwave field intensities: if the microwave field is sufficiently strong to ensure the quasilinear deformation of the distribution function of the resonant electrons, then the electron flux from the nonresonant low-energy region becomes appreciable. As a result, the EDF relaxes to a steady state (Fig. 1b). The relaxation time is determined by the rate at which zero-energy electrons diffuse up to the resonance energy and is independent of the power of the quasilinear pump microwave field: $t_{\text{st}} \approx \nu_{ee}^{-1}(u_0)$. This estimate fails to hold when the resonance region approaches very low energies ($u_0 - \Delta u \ll u_0$) or when the microwave radiation intensity is too low ($\sqrt{D_{ql} t_{\text{st}}} \ll \Delta u$).

The approximate collision integral with a fixed temperature of the background plasma is valid if the total energy W_{st} of the electrons in the steady state is close to the initial energy W_0, i.e., the energy corresponding to the background electron distribution:

$$\eta \equiv \frac{W_{\text{st}} - W_0}{W_0} \ll 1. \tag{22}$$

The maximum electron energy can be estimated by assuming that the microwave field is sufficiently strong to neglect the effect of collisions on the formation of the quasilinear plateau in the EDF in the resonance region in velocity space. In the steady state, the EDF established outside the resonance region corresponds to an isotropic Maxwellian distribution; inside the resonance region, it is uniform over transverse electron velocity. Taking into account the continuity of the EDF at the boundaries of the resonance region, one can readily show that, inside the region, the EDF should also be isotropic and the steady-state distribution function should have the form

$$f_{\text{st}} = \begin{cases} n_0 \exp(-u^2) & \text{for} \quad 0 \le u < u_1 \\ n_0 \exp(-u_1^2) & \text{for} \quad u_1 \le u < u_2 \\ n_0 \exp(-u_1^2 + u_2^2 - u^2) & \text{for} \quad u_2 \le u < \infty, \end{cases} \tag{23}$$

where the constant n_0 is determined from the condition that the number of electrons is conserved. The expressions for the total energy corresponding to the EDF (23) and for the quantity η are fairly complicated:

$$\eta = \frac{16\Delta u(5u_0^4 + 10u_0^2\Delta u^2 + \Delta u^4)}{5\{4\Delta u(3 + 6u_0^2 + 2\Delta u^2) + 3\sqrt{\pi}[\exp(u_1^2)\text{erf}(u_1) + \exp(u_2^2)\text{erfc}(u_2)]\}}. \tag{24}$$

However, for $\Delta u \le 0.2$, it is sufficient to retain only the linear term in the expansion in Δu:

$$\eta \approx \left[\frac{16}{3\sqrt{\pi}} u_0^4 \exp(-u_0^2)\right]\Delta u. \qquad (25)$$

In the applicability range of expression (25), the factor in square brackets is close to unity. Consequently, the relative energy unbalance associated with the approximate character of the linear collision operator is equal to $\eta \approx \Delta u$ and the electron temperature in the collision integral can be assumed to be fixed under the condition $\Delta u \ll 1$. The time dependence of the temperature of the background electrons can be introduced correctly if an increase in the electron energy is markedly larger than the error associated with the difference in the energies corresponding to the perturbed and background electron distributions: $W - W_0 \gg \eta W_0$.

The kinetic equation with the linear collision integral in which the background electron temperature is time-dependent or with the nonlinear collision integral has no steady-state solutions; however, in other respects, the dynamics of the formation of the perturbed EDF in the initial stage is qualitatively the same. As an example, Fig. 2 illustrates the evolution of the EDF calculated using the energy balance equation (16) with the time-dependent temperature of the background electrons (the scales on the axes are chosen so that the Maxwellian distribution function is represented by a straight line). Solutions *1–6* in Fig. 2 are seen to be essentially the same as those in Fig. 1a. This indicates that, on time scales $t \le 0.5\nu_0^{-1}$, the EDF computed by different methods evolves in essentially the same way. On longer time scales (Fig. 2, curves *7–9*), the number of high-energy electrons increases because of the increase in the effective electron temperature. For comparison, the dashed curve in Fig. 2 represents the steady-state solution obtained for a fixed electron temperature (Fig. 1a, curve *9*).

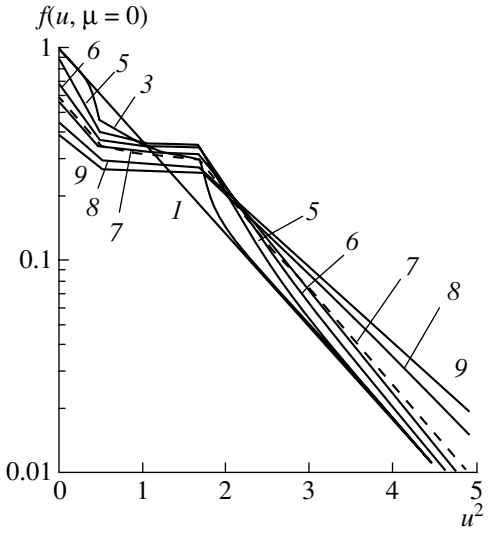

Fig. 2. Formation of the EDF $f(u, \mu = 0)$ according to the kinetic equation with the time-dependent linear collision integral for the same times and parameter values as those in Fig. 1. The ordinate is the EDF on a logarithmic scale, and the abscissa is the squared electron velocity. The dashed curve corresponds to curve *9* in Fig. 1a.

4. QUASI-STEADY ELECTRON HEATING

After the rapid stage, in which a quasilinear plateau appears in the EDF, the absorbed microwave power substantially decreases but remains finite, because the formation of a plateau is hindered by collisions. For this reason, the majority of electrons are heated on a longer time scale in comparison with that on which the quasilinear perturbations develop (the initial heating stage is illustrated in Fig. 2).

Figure 3 shows time evolutions of the total electron energy calculated from the kinetic equation with linear [see Eqs. (13)–16)] and nonlinear [see Eqs. (18)–(21)] collision integrals for two parameter sets differing in microwave intensity and position of the resonance region in velocity space. For the linear model, varia-

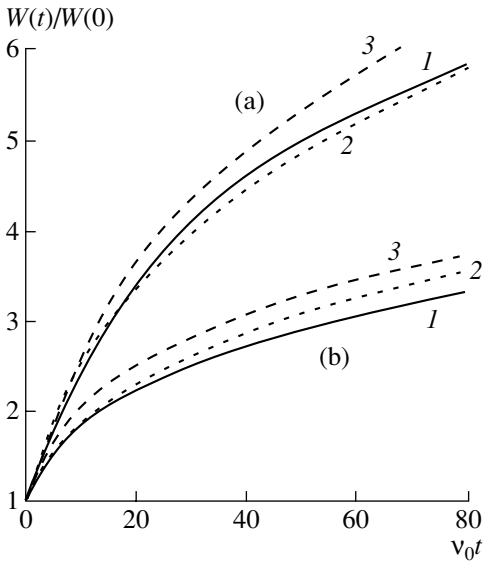

Fig. 3. Electron energy dynamics calculated by integrating the kinetic equation numerically. Curve *1* was obtained with the nonlinear collision integral, and curves *2* and *3* were obtained with the time-dependent linear collision integral. Curves *2* and *3* differ in the methods by which the energy was determined: curve *2* was computed by integrating the product of the electron energy and the time-dependent EDF [see relationship (26)], and curve *3* was computed from the energy balance equation [see relationship (27)]. The parameters of the family of curves (a) are $\nu_{ql}/\nu_0 = 0.5$, $u_0 = 2$, and $\Delta u = 0.3$, and the parameters of the family of curves (b) are $\nu_{ql}/\nu_0 = 1$, $u_0 = 1$, and $\Delta u = 0.3$. In both cases, the effective ion charge number is unity.

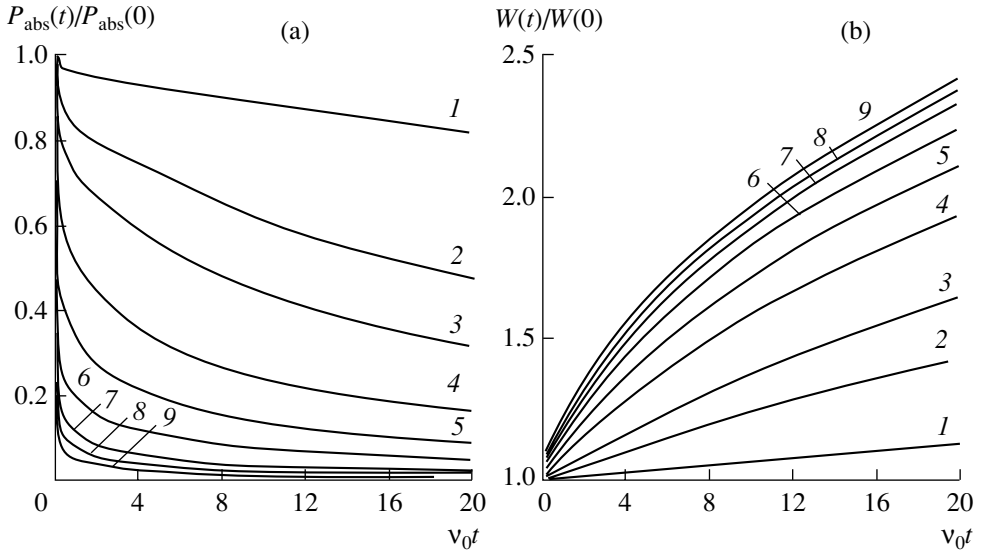

Fig. 4. Time evolutions of (a) the absorbed microwave power and (b) electron energy for $\nu_{ql}/\nu_0 =$ (*1*) 0.01, (*2*) 0.05, (*3*) 0.1, (*4*) 0.25, (*5*) 0.5, (*6*) 1.0, (*7*) 2.0, (*8*) 3.0, and (*9*) 5.0. The parameters of the resonance region are $u_0 = 1$ and $\Delta u = 0.3$, and the effective ion charge number is $Z_{eff} = 1$. The time evolutions were calculated using the linear collision integral in which the electron temperature was determined from the energy balance equation.

tions in the energy of the electron component were calculated in two ways: first, by integrating the electron energy with the time-dependent EDF,

$$W(t) = \int \frac{1}{2} m v^2 f d^3\mathbf{v}, \tag{26}$$

and, second, from the energy balance equation (16),

$$W_b(t) = \int_0^t P_{abs} dt. \tag{27}$$

We can see that, if the temperature of the background electrons in the linear collision integral is determined from the energy balance equation, then the solutions to the linear and nonlinear problems coincide fairly closely in a wide range of the parameters. Notably, in the model with the linear collision integral, the energy conservation law is satisfied only asymptotically: the rate at which the total electron energy increases on long time scales is equal to the absorbed microwave power, although the energy balance equation implies that this property is peculiar only to the background electrons, $\dot{W} \approx \dot{W}_b \equiv P_{abs}$.

Note that the parameters of the background electron distribution may be determined using the Chapman–Cowling approach [12], in which the density and temperature of the background electrons are incorporated into the linearized kinetic equation in such a way that the perturbed EDF $f_1 = f - f_M$ is assigned zero values of the electron density and energy. If the total number of electrons is conserved, this indicates that the time-dependent temperature of the background electrons in the linear collision integral is determined by the total electron energy:

$$\frac{3}{2} N_e T_e(t) = W(t), \tag{28}$$

where $W(t)$ is given by formula (26). For the collision integral that conserves the electron energy, this way of determining the time-dependent temperature of the background electrons is exactly equivalent to the method based on the energy balance equation (16); generally, formula (28) gives rise to the additional energy sink term $P_c = \int \frac{1}{2} m v^2 L_{coll} f d^3\mathbf{v}$ in the energy balance equation. Numerical calculations show that the solutions to the kinetic equation with the linear collision integral (13), in which the time-dependent temperature of the background electrons is determined from relationship (28), deviate substantially from the solutions to the kinetic equation with the reduced nonlinear collision integral (18). Relationship (28) implies that the sink term P_c always remains finite, thereby explaining this continuously increasing deviation, while the energy balance equation (16) implies that $P_c \longrightarrow 0$, which corresponds to the asymptotic conservation of electron energy in the quasisteady heating regime.

Figure 4 shows time evolutions of the total electron energy and absorbed microwave power (both normalized to their values corresponding to the initial Max-

wellian EDF) for different microwave field intensities. Figure 4a illustrates the effect of the quasilinear degradation of the absorbed power: the stronger the microwave field, the faster is the rate at which the relative (normalized to the equilibrium value) absorbed power decreases with time. As a result, for a sufficiently strong microwave, the absolute value of the absorbed microwave power no longer increases with the field intensity: the time dependence of the electron energy approaches a certain universal curve, which is independent of the microwave field intensity (see Fig. 4b), and the relative absorbed power becomes inversely proportional to the microwave field intensity, $P_{\rm abs}/P_{\rm abs}(0) \sim \nu_{ql}^{-1}$.

In order to qualitatively explain the above numerical results, we turn to the model one-dimensional kinetic equation with a linear collision integral, from which we can analytically obtain a qualitative estimate of the quasisteady electron heating rate. In the kinetic equation (1) with operators (6), (9), and (13), we represent the EDF as a sum of the isotropic part $F(u)$ and a small correction $\delta f(u, \mu)$. Then, we perform averaging over the pitch angle variable and omit small terms on the order of $\delta f(u, \mu)$ and the time derivatives, which are small in the quasisteady heating regime. The anisotropic part of the EDF can be neglected in one of two cases: when the rate of isotropization due to e–i elastic collisions is high ($Z_{\rm eff} \gg 1$) or when the resonance region in velocity space is sufficiently narrow ($2\Delta u \ll u_0$). As a result, we arrive at a one-dimensional quasisteady kinetic equation for the isotropic EDF component $F(u)$, which corresponds to the absence of electron fluxes in velocity space:

$$\begin{aligned}(D_{ee} + \bar{D}_{ql})\frac{dF}{du} + F_{ee}F &= 0,\\ \bar{D}_{ql}(u) &= \int_0^1 (1-\mu^2) D_{ql}(u,\mu)\,d\mu,\end{aligned} \tag{29}$$

where $\bar{D}_{ql}(u)$ is the quasilinear diffusion coefficient averaged over the electron pitch angle. The expression for the absorbed microwave power can be easily derived for a sufficiently narrow resonance region in velocity space, when the EDF changes only slightly during the formation of a quasilinear plateau and is close to the Maxwellian distribution function of the background electrons, while the derivative of the EDF in the resonance region can change substantially:

$$\frac{dF}{du} \approx \begin{cases} -\dfrac{F_{ee}(u_0)}{D_{ee}(u_0) + \bar{D}_{ql}(u_0)} f_M(u_0), & \text{for } |u-u_0| \le \Delta u \\ \dfrac{d}{du} f_M(u), & \text{for } |u-u_0| > \Delta u. \end{cases} \tag{30}$$

As a result, expression (17) for the absorbed microwave power becomes

$$P_{\rm abs}(T_e) \approx N_e T_{e0} \frac{16}{\sqrt{\pi}} \frac{F_{ee}(u_0) u_0^3 \Delta u}{D_{ee}(u_0)/\bar{D}_{ql}(u_0) + 1} f_M(u_0), \tag{31}$$

where $F_{ee}(u_0)$, $D_{ee}(u_0)$, and $f_M(u_0)$ are functions of the temperature of the background electrons. Expression (31) implies that, first, when the microwave field is sufficiently strong ($\bar{D}_{ql} \gg D_{ee}$), the maximum (for a given position of the resonance region in velocity space) microwave power absorbed in the quasisteady heating regime is independent of the microwave field intensity and, second, the electron energy as a function of time approaches a certain universal curve (Fig. 4b). Since D_{ee} is a bounded function of the electron temperature, there always exists a lower bound for the microwave field intensity at which the inequality $\bar{D}_{ql} \gg D_{ee}$ will be satisfied throughout the entire heating process (see the Appendix for details). This bound depends only on the initial conditions. In the approximation at hand, the electron heating rate is proportional to the width of the resonance region, while its dependence on the position of the resonance region is more complicated. From formula (31), we can see that the absorbed microwave power tends to zero in both limits $u_0 \longrightarrow 0$ and $u_0 \longrightarrow \infty$. Hence, we arrive at the following conclusion: in phase space, there may in principle exist an optimum position of the energy deposition region at which the electron heating is most efficient.[1] This may be proved by substituting relationship (31) into the energy balance equation (16) and finding the time dependence of the electron temperature in explicit form. In the Appendix, we carry out an analogous analysis for the case in which the absorbed microwave power reaches a steady level. In particular, it is shown that, if there is no need to heat the plasma to very high temperatures, then the heating is most efficient when the energy is pumped into thermal electrons ($u_0 \sim 1$). We also discuss there the applicability conditions for the validity of the above approximations.

5. CONCLUSION

We have considered two simplified model e–e collision integrals that make it possible to describe electron heating by microwave radiation under ECR conditions. With these model collision integrals, the kinetic equations have close solutions describing the perturbed distribution function of the resonant electrons and the quasisteady heating of all plasma electrons under the conditions of the quasilinear degradation of the absorbed microwave power. The model integrals have their own specific advantages and require almost the same expenditure of computational resources. The simplified non-

[1] Strictly speaking, expression (31) fails to hold in the range $u_0 \le \Delta u$, for which, however, the conclusion also remains valid.

linear collision integral is advantageous in that it automatically conserves the total electron energy. In turn, the model with the time-dependent linear collision integral can be generalized in a more natural way to a spatially inhomogeneous case in which the temperature and density profiles are prescribed and either their time evolutions or their steady-state shapes are known. As for the hydrodynamic parameters of the background plasma (primarily, electron temperature and density), they can be determined directly from the experimental data or found by solving the set of transport equations with allowance for energy and particle transport in real space. In the latter case, the kinetic model can be incorporated into transport equations as a means of determining the source describing the absorption of microwave power with allowance for the perturbations of the EDF.

ACKNOWLEDGMENTS

This work was supported in part by the Russian Foundation for Basic Research, project no. 00-02-17200.

APPENDIX

Electron Temperature Dynamics at a High Heating Power

Here, we solve the energy balance equation (16) analytically using relationship (31) for the absorbed microwave power and assuming that the absolute value of the absorbed power is maximum, i.e., that the saturation condition $\bar{D}_{ql} \gg D_{ee}$ is satisfied. The relationship between the coefficients $\bar{D}_{ql}$ and D_{ee} can change during plasma heating, because the latter coefficient depends on the temperature of the background electrons: being a function of temperature, the coefficient $D_{ee}(T_e)$ increases from zero to the maximum value (at a certain temperature) and then decreases monotonically to zero. It can be proved rigorously that, at the temperature at which the coefficient $D_{ee}(T_e)$ is maximum, the following equalities should hold:

$$T_e^* = \alpha u_0^2 T_{e0}, \quad D_{ee}^* = \frac{1}{\sqrt{\pi\alpha} e^{1/\alpha}} \nu_0 u_0, \qquad 2\alpha^{3/2} e^{1/\alpha} \int_0^{1/\sqrt{\alpha}} s^2 e^{-s^2} ds = 1. \tag{32}$$

Since the constant α, which is the root of the above transcendental equation, is close to unity, we set $\alpha = 1$. The inequality $\bar{D}_{ql} \gg D_{ee}$ is satisfied at unlimited heating of the plasma if one of the following two sufficient conditions holds: (i) this inequality is satisfied at the initial instant and the initial temperature corresponds to the decreasing part of the dependence $D_{ee}(T_e)$ (i.e., $\bar{D}_{ql} \gg D_{ee}(T_{e0})$ and $T_{e0} \geq T_e^*$, which is equivalent to $u_0 \leq 1$) or (ii) this inequality is satisfied at the most

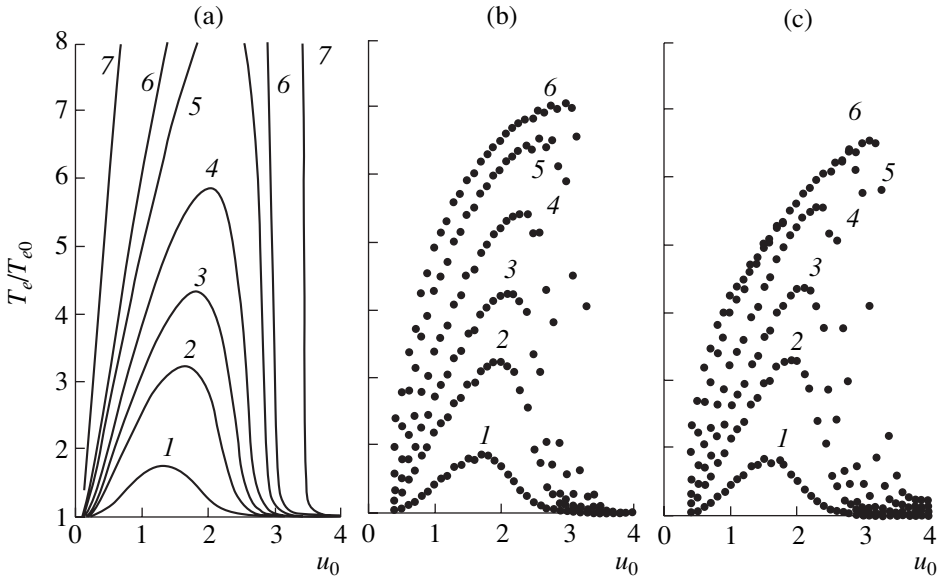

Fig. 5. Dependence of the electron temperature achieved at a certain time on the position of the resonance region. Plot (a) presents the result calculated by the analytic formula (35), and plots (b) and (c) are computed using the linear and nonlinear collision operators, respectively, for $\nu_{ql}/\nu_0 = 1$ and $\Delta u = 0.3$. Curves *1–7* are computed at different dimensionless times $\tau = \nu_0 \Delta u t$: (*1*) 1.0, (*2*) 5.0, (*3*) 10, (*4*) 20, (*5*) 50, (*6*) 100, and (*7*) 1000.

"unfavorable" instant, $\bar{D}_{ql} \gg D_{ee}^*$. As an example, we present the explicit form of condition (ii) for an extraordinary wave at the second harmonic of the electron cyclotron frequency:

$$\nu_{ql} \gg \frac{15}{8\sqrt{\pi}e}\nu_{ee}(u_0) \approx 0.4\nu_{ee}(u_0). \quad (33)$$

For the maximum absorbed microwave power, the desired energy balance equation has the form

$$\frac{3}{2}\frac{d}{dt}T_e(t) = T_{e0}\frac{16}{\sqrt{\pi}}F_{ee}(u_0)f_M(u_0)u_0^3\Delta u. \quad (34)$$

The solution to Eq. (34) with the initial condition $T_e(0) = T_{e0}$ can be represented implicitly as

$$\tau = u_0^4\left[G\left(\frac{\theta}{u_0^2}\right) - G\left(\frac{1}{u_0^2}\right)\right],$$
$$G(x) = \frac{3\pi}{128}\int_1^x y^{3/2}e^{1/y}\left(\int_0^{1/\sqrt{y}} s^2e^{-s^2}ds\right)^{-1}dy, \quad (35)$$

where $\theta = T_e/T_{e0}$ and $\tau = \nu_0\Delta u t$ are the dimensionless temperature and dimensionless time. From this expression, we can determine the characteristic time of the quasisteady heating: $t_h \approx \nu_{ee}^{-1}(u_0)u_0/\Delta u$.

In the narrow resonance region approximation, the width of the resonance region and the collision frequency determine only the normalizing factor for the dimensionless time τ; in dimensionless variables, the heating dynamics depends only on the resonant velocity u_0. As was noted in Section 4, this dependence is characterized by a certain optimum value of u_0 at which the electrons are heated to a given temperature at the highest rate. This is illustrated in Fig. 5a, which shows the family of solutions (35) describing how the electron temperature achieved at different instants of the dimensionless time τ depends on the position of the resonance region. At the extremes of the curves, the relationship between the temperature, the dimensionless time, and the position of the resonance region can be obtained by a numerical approximation. As an example, we have

$$u_0^{\text{opt}} \approx 1.131\Theta^{1/3},$$
$$\tau^{\text{opt}} \approx 0.844(\Theta - 1)^2 \quad (\text{for} \quad 1 \le \Theta \le 10), \quad (36)$$

$$u_0^{\text{opt}} \approx \sqrt{-1.778 + 3.342\ln\Theta},$$
$$\tau^{\text{opt}} \approx 31.531 + 0.042\Theta^3 \quad (\text{for} \quad 5 \le \Theta \le 100). \quad (37)$$

For comparison, Figs. 5b and 5c illustrate numerical results obtained with the above two model collision integrals for a resonance region of finite width and for a finite intensity of the pump microwave field. The microwave field strength was chosen to satisfy the inequality $\bar{D}_{ql} \gg D_{ee}$; the discrepancy between the analytical and numerical curves at high temperatures stems from the finite width of the resonance region and vanishes as Δu decreases.

Solution (35) can be examined analytically using the following asymptotic expressions for the function G:

$$G(x) = \frac{9\pi}{512}x^4\left\{1 + \frac{4}{3x} + \frac{1}{x^2} + \frac{2}{3x^2} + \frac{\ln x}{6x^4}\right\} + c_1 + O(1/x),$$
$$c_1 \approx 0.219 \quad (x \gg 1), \quad (38)$$

$$G(x) = -\frac{3\sqrt{\pi}}{32}e^{1/x}x^{7/2}\left\{1 + \frac{7}{2}x + \frac{63}{4}x^2 + \ldots\right\} + c_2,$$
$$c_2 \approx -0.283 \quad (x \ll 1). \quad (39)$$

For moderate heating ($1 \le \Theta \le 10$), the argument of the function G is on the order of unity, so that, instead of the asymptotic expressions (38) and (39), we can use the approximations of G in the transition region; e.g., in the region $0.1 \le x \le 2$, we have

$$G(x) \approx ax^4 - b/x^2 + c_3, \quad (40)$$

where $a \approx 0.166$, $b \approx 0.019$, and $c_3 \approx -0.185$. Thus, with expressions (38)–(40), the temperature dependences of the optimum heating conditions are close to those in formulas (36) and (37).

The sufficient conditions for the applicability of Eqs. (29), (31), (34), and (35) are that the EDF in the resonance region should change insignificantly ($|f_M(u_0 + \Delta u) - f_M(u_0)| \ll f_M(u_0)$) and the characteristic heating time t_h should be much longer than both the time of the plateau formation, $t_{ql} \approx \Delta u^2/\bar{D}_{ql}$, and the collisional relaxation time, $t_{\text{st}} \approx \nu_{ee}^{-1}(u_0)$; i.e.,

$$\Delta u \ll \max[\Theta/(2u_0), u_0^2(8/15\nu_{ql}/\nu_0)^{1/3}, u_0]. \quad (41)$$

Hence, all three conditions impose restrictions on the width of the resonance region.

REFERENCES

1. A. I. Akhiezer, I. A. Akhiezer, R. V. Polovin, *et al.*, *Plasma Electrodynamics* (Nauka, Moscow, 1974; Pergamon, Oxford, 1975).
2. C. F. F. Karney, Comput. Phys. Rep. **4**, 183 (1986).
3. E. Westerhof, in *Proceedings of the 9th Joint Workshop on Electron Cyclotron Emission and Electron Cyclotron Heating, Borrego Springs, CA, 1995*, p. 3.
4. L. D. Landau, Zh. Éksp. Teor. Fiz. **7**, 203 (1937).

5. E. V. Suvorov and M. D. Tokman, Plasma Phys. **25**, 723 (1983).

6. V. V. Alikaev, A. G. Litvak, E. V. Suvorov, and A. A. Fraĭman, in *Proceedings of the All-Union Conference on Radio Frequency Plasma Heating, Gorki, 1982*, Ed. by A. G. Litvak (Inst. of Applied Physics, SSSR Acad. Sci., Gorki, 1983), p. 6.

7. Yu. N. Dnestrovskij and D. P. Kostomarov, *Numerical Simulation of Plasmas* (Mir, Moscow, 1982; Springer-Verlag, New York, 1986).

8. B. A. Trubnikov, in *Reviews of Plasma Physics*, Ed. by M. A. Leontovich (Gosatomizdat, Moscow, 1963; Consultants Bureau, New York, 1963), Vol. 1.

9. E. V. Suvorov and A. G. Shalashov, Preprint No. 462 (Inst. of Applied Physics, Russian Acad. Sci., Nizhni Novgorod, 1998).

10. N. V. Karetkina, Vestn. Mosk. Univ., Ser. 15: Vychisl. Mat. Kibern., No. 3 (1978).

11. A. V. Bobylev, I. F. Potapenko, and V. A. Chuyanov, Preprint No. 76 (Inst. of Applied Mathematics, USSR Acad. Sci., Moscow, 1980).

12. S. Chapman and T. G. Cowling, *The Mathematical Theory of Nonuniform Gases* (Cambridge Univ. Press, Cambridge, 1970).

Translated by I. A. Kalabalyk

Plasma Physics Reports, Vol. 28, No. 1, 2002, pp. 57–62. Translated from Fizika Plazmy, Vol. 28, No. 1, 2002, pp. 62–67.
Original Russian Text Copyright © 2002 by D. Klochkov, A. Klochkov.

PLASMA INSTABILITY

Effect of the Plasma Electron Motion on the Development of Cherenkov Instability in a Waveguide

D. N. Klochkov* and A. N. Klochkov**

**Institute of General Physics, Russian Academy of Sciences, ul. Vavilova 38, Moscow, 117942 Russia*

***Tula State University, pr. Lenina 94, Tula, 300026 Russia*

Received April 3, 2001; in final form, July 10, 2001

Abstract—A linear theory of the Cherenkov amplification in a transversely nonuniform waveguide in an infinitely strong magnetic field is constructed with allowance for both ordered and thermal motions of plasma electrons. The effect of these electron motions on the threshold for the onset of Cherenkov instability is investigated. The amplification coefficients and the conditions for the onset of the instability are determined. © *2002 MAIK "Nauka/Interperiodica".*

1. At present, relativistic Cherenkov plasma masers (RCPMs) are the only devices in which the mean microwave frequency can be continuously tuned in a band with an upper-to-lower boundary frequency ratio of 7 at a power of 50 MW [1]. In an RCPM, this tuning range is achieved by changing the plasma density.

In this area of research, good agreement has been achieved between theory and experiment [2, 3]. Nevertheless, some of the effects that have not been incorporated into the RCPM theory can be important under certain conditions. In particular, these are the effects of thermal and ordered motions of plasma electrons on the threshold for the onset of Cherenkov instability.

Here, we construct a linear theory of the Cherenkov amplification in a transversely nonuniform waveguide in an infinitely strong magnetic field with allowance for, specifically, thermal and ordered motions of plasma electrons.

We start with the projection of the Maxwell equation onto the z-axis,

$$\left(\Delta_\perp + \partial_z^2 - \frac{1}{c^2}\partial_t^2\right)E_z = 4\pi\left(\partial_z\rho + \frac{1}{c^2}\partial_t j_z\right), \qquad (1)$$

and the Vlasov equation for beam and plasma electrons,

$$\frac{\partial f}{\partial t} + v\frac{\partial f}{\partial z} + eE_z\frac{\partial f}{\partial p} = 0. \qquad (2)$$

Since we are considering fast processes, we can neglect ion motion, assuming that the ions constitute an immobile positive background. We set $E_z = \tilde{E}(r)e^{-i\omega t + ikz}$ and $f = f_0 + f_1$ (where $f_1 \sim E_z$) and linearize Eqs. (1) and (2) in a standard way to obtain

$$\Delta_\perp\tilde{E} + \left(\frac{\omega^2}{c^2} - k^2\right) \times\left[1 - \frac{4\pi e^2}{m}\int\frac{\gamma^{-3}(v)f_0(r, p)dp}{(\omega - kv)^2}\right]\tilde{E} = 0, \qquad (3)$$

where $\gamma(v) = (1 - v^2/c^2)^{-1/2}$ is the relativistic factor. We supplement Eq. (3) with the following boundary condition at the waveguide wall: $\tilde{E}(R) = 0$, where R is the waveguide radius. The unperturbed distribution function describing a plasma and a cold beam can be represented as

$$f_0(r, p) = f_p(p)P_{\perp p}(r) + n_b\delta(p - m\gamma u)P_{\perp b}(r). \qquad (4)$$

Here, $f_p(p)$ is the distribution function of the plasma electrons, n_b is the density of the beam electrons, u is their unperturbed velocity, $\gamma = \gamma(u)$, and $P_{\perp\alpha}(r)$ are the beam ($\alpha = b$) and plasma ($\alpha = p$) profiles. As a result, we arrive at the equation

$$\Delta_\perp\tilde{E} + \left(\frac{\omega^2}{c^2} - k^2\right) \times\left[1 - \omega_p^2K(\omega, k)P_{\perp p}(r) - \frac{\omega_b^2\gamma^{-3}}{(\omega - ku)^2}P_{\perp b}(r)\right]\tilde{E} = 0. \qquad (5)$$

Here, $\omega_\alpha = (4\pi e^2 n_\alpha/m)^{1/2}$ is the Langmuir frequency of the plasma electrons ($\alpha = p$) or the beam electrons ($\alpha = b$), and the following notation is introduced:

$$K(\omega, k) = \frac{1}{n_p}\int\frac{\gamma^{-3}(v)f_p(p)}{(\omega - kv)^2}dp. \qquad (6)$$

1063-780X/02/2801-0057$22.00 © 2002 MAIK "Nauka/Interperiodica"

For an immobile hot plasma, for which $f_p(p)$ is a Maxwellian distribution function, we have

$$K(\omega, k) = \frac{1}{\omega^2} F\left(\frac{\omega}{k v_T}\right). \tag{7}$$

Here, v_T is the thermal velocity of the plasma electrons and $F(x) = x^2[J_+(x) - 1]$, where $J_+(x)$ is the familiar function [4], satisfying the asymptotic expressions

$$J_+(x) = \begin{cases} 1 + \frac{1}{x^2} + \frac{3}{x^4} + \ldots - i\sqrt{\frac{\pi}{2}} x e^{-x^2/2}, & x \gg 1, \\ i\sqrt{\frac{\pi}{2}} x, & |x| \ll 1. \end{cases} \tag{8}$$

When the directed motion of plasma electrons is taken into account, we can represent the distribution function of the cold plasma electrons as $f_p(p) = n_p \delta(p + m v_p)$ and obtain

$$K(\omega, k) = \frac{1}{(\omega + k v_p)^2}. \tag{9}$$

If the plasma electrons move from the collector toward the cathode, we have $v_p > 0$; otherwise, we have $v_p < 0$. Note that passing over to the frame of reference with respect to which the plasma electrons are at rest reduces our problem to the familiar problem of an immobile cold plasma [5]. Nevertheless, it is expedient to carry out the analysis in the laboratory frame. The reason for this is twofold. First, the experimental data are usually recorded in the laboratory frame. Second, in actual experiments, the beam–plasma interaction region is bounded in the longitudinal direction by cavity boundaries, which are fixed in the laboratory frame.

In experiments carried out by Strelkov and Ul'yanov [1], only axisymmetric field harmonics were excited. Consequently, in what follows, we restrict ourselves to considering the axisymmetric case, in which the transverse Laplacian operator has the form $\Delta_\perp = \frac{1}{r}\partial_r(r\partial_r)$.

We consider a cable wave–based version of a plasma amplifier. Specifically, we assume that an annular beam and an annular plasma are separated in space and are infinitely thin, so that their profiles can be represented as

$$P_{\perp\alpha}(r) = \Delta_\alpha \delta(r - r_\alpha); \tag{10}$$

where Δ_α is the plasma thickness ($\alpha = p$) or the beam thickness ($\alpha = b$). Equation (5) implies that the radial derivative of the longitudinal component of the electromagnetic field undergoes a jump at both the plasma and the beam:

$$\tilde{E}'(r_p + 0) - \tilde{E}'(r_p - 0) = -\left(k^2 - \frac{\omega^2}{c^2}\right)\omega_p^2 K(\omega, k)\Delta_p \tilde{E}(r_p), \tag{11a}$$

$$\tilde{E}'(r_b + 0) - \tilde{E}'(r_b - 0) = -\left(k^2 - \frac{\omega^2}{c^2}\right)\frac{\omega_b^2 \gamma^{-3}}{(\omega - ku)^2}\Delta_b \tilde{E}(r_b). \tag{11b}$$

In turn, the field $\tilde{E}(r)$ is continuous.

We consider the case in which the plasma and the beam are separated only slightly, so that, in formula (6), the integral over the region where the plasma and beam fields overlap is not small. To be specific, we also set $0 < r_b \le r_p < R$. As will be clear later, the case in which the beam and the plasma have the same radius (i.e., $r_b = r_p$) is a particular case; generally, the form of the resulting dispersion relation is independent of the sign of the inequality $r_b < r_p$. In a plasma waveguide, the only waves that can propagate in the frequency range $\omega < \omega_p$ are surface waves (in this range, the internal waves are damped). Under the above assumptions, the longitudinal component of the field of the surface waves has the form

$$\tilde{E}(r) = \begin{cases} I_0(k_\perp r), & 0 \le r \le r_b \\ \frac{I_0(k_\perp r_b)}{Z_0(k_\perp r_b)} Z_0(k_\perp r), & r_b \le r \le r_p \\ \frac{I_0(k_\perp r_b)}{Z_0(k_\perp r_b)} \frac{Z_0(k_\perp r_p)}{H_0(k_\perp r_p)} H_0(k_\perp r), & r_p \le r \le R, \end{cases} \tag{12}$$

where

$$Z_n(x) = I_n(x) + (-1)^n C K_n(x), \tag{13a}$$

$$H_n(\alpha r) = I_n(\alpha r) - (-1)^n \frac{I_0(\alpha R)}{K_0(\alpha R)} K_n(\alpha r), \tag{13b}$$

$I_n(x)$ and $K_n(x)$ are modified Bessel functions, and C is a constant.

The matching conditions (11) yield the dispersion relation

$$\left(k - \frac{\omega}{u}\right)^2 - \left(k^2 - \frac{\omega^2}{c^2}\right)\frac{\omega_b^2 \gamma^{-3}}{\kappa_b^2(\alpha, \zeta) u^2} = \left(k^2 - \frac{\omega^2}{c^2}\right)\frac{\omega_p^2}{\kappa_\perp^2} \times K(\omega, k)\left[\left(k - \frac{\omega}{u}\right)^2 - \left(k^2 - \frac{\omega^2}{c^2}\right)\frac{\omega_b^2 \gamma^{-3}}{\kappa_b^2(\alpha, \beta) u^2}\right], \tag{14}$$

where

$$\kappa_b^{-2}(a, b) = r_b\Delta_b I_0^2(a)\left[\frac{K_0(a)}{I_0(a)} - \frac{K_0(b)}{I_0(b)}\right], \quad (15)$$

$\alpha = k_\perp r_b$, $\beta = k_\perp r_p$, and $\zeta = k_\perp R$. The parameter $\kappa_\perp$ satisfies the equation [2]

$$\kappa_\perp^2 = \left\{r_p\Delta_p I_0^2(k_\perp r_p)\left[\frac{K_0(k_\perp r_p)}{I_0(k_\perp r)} - \frac{K_0(k_\perp R_p)}{I_0(k_\perp R)}\right]\right\}^{-1}. \quad (16)$$

In the long-wavelength limit $k_\perp R \ll 1$, we have

$$\kappa_\perp^2 = \frac{1}{r_p\Delta_p \ln\left(\frac{R}{r_p}\right)}. \quad (17)$$

2. First, we consider the case when an infinitely thin, annular plasma and beam have the same radius ($r_p = r_b$), i.e., when the beam slips along the plasma surface. In this case, the dispersion relation (14) becomes

$$\left(k - \frac{\omega}{u}\right)^2\left[\left(k^2 - \frac{\omega^2}{c^2}\right)K(\omega, k) - \frac{\kappa_\perp^2}{\omega_p^2}\right] = -\left(k^2 - \frac{\omega^2}{c^2}\right)\frac{\omega_b^2}{\omega_p^2}\frac{\gamma^{-3}}{u^2}\frac{\Delta_b}{\Delta_p}. \quad (18)$$

Now, we turn to the immobile hot plasma model, in which the quantity $K(\omega, k)$ is described by expression (7). We represent the solution to Eq. (18) in the form

$$k = \frac{\omega}{u}(1 + \delta x) \quad (19)$$

and assume that the inequality

$$2\gamma^2|\delta x| \ll 1 \quad (20)$$

is satisfied. In this case, Eq. (18) reduces to the cubic equation

$$(\delta x)^2\left[\delta x + \frac{F(\xi) - \frac{\kappa_\perp^2 u^2\gamma^2}{\omega_p^2}}{2\gamma^2 F(\xi) - \xi F'(\xi)}\right] = -\frac{\omega_b^2}{\omega_p^2}\gamma^{-3}\frac{\Delta_b}{\Delta_p}\frac{1}{2\gamma^2 F(\xi) - \xi F'(\xi)}, \quad (21)$$

where $\xi = u/v_T$ is the reciprocal of the dimensionless thermal velocity of the plasma electrons. In the asymptotic limit $\xi \gg 1$, Eq. (21) can be written as

$$(\delta x)^2(\delta x + A + iB) = -\frac{1}{2}\frac{\omega_b^2}{\omega_p^2}\gamma^{-5}\frac{\Delta_b}{\Delta_p}(C + iD), \quad (22)$$

where

$$A = \frac{1}{2\gamma^2}\left[1 + 3\xi^{-2} - \frac{\kappa_\perp^2 u^2\gamma^2}{\omega_p^2}\right]C, \quad (23a)$$

$$B = \frac{1}{2\gamma^2}\sqrt{\frac{\pi}{2}} \times \left[\frac{\xi^2}{2\gamma^2}\left(1 + 3\xi^{-2} - \frac{\kappa_\perp^2 u^2\gamma^2}{\omega_p^2}\right) - 1\right]\xi^3 e^{-\xi^2/2}, \quad (23b)$$

$$C = 1 - 3(1 + \gamma^{-2})\xi^{-2}, \quad (23c)$$

$$D = \sqrt{\frac{\pi}{2}}\frac{1}{2\gamma^2}(\xi^2 + 2\gamma^2 - 3)\xi^3 e^{-\xi^2/2}. \quad (23d)$$

For $A = 0$, the solution to Eq. (22) corresponds to the single-particle Cherenkov resonance, which occurs under the condition

$$\kappa_\perp^2 u^2\gamma^2 = \omega_p^2\left(1 + 3\frac{v_T^2}{u^2}\right). \quad (24)$$

As the thermal velocity v_T of the plasma electrons increases, their resonant Langmuir frequency ω_p decreases because of the increase in the phase velocity of the plasma wave. In fact, in the absence of an electron beam, the wave dispersion law in a plasma cavity has the form

$$\omega^2 = k^2c^2\frac{\omega_p^2}{\omega_p^2 + \kappa_\perp^2 c^2}\left(1 + 3\frac{\kappa_\perp^2 v_T^2}{\omega_p^2}\right). \quad (25)$$

The Cherenkov resonance condition (24) implies that, for nonrelativistic beams, the shift in the resonant frequency is the largest.

Under the resonance condition (24), the instability of a hot plasma may develop in two different ways. The case $|\delta x| \ll |B|$ corresponds to a dissipative instability with the amplification coefficient

$$\delta x = \frac{1 - i}{2}\frac{\omega_b}{\omega_p}\gamma^{-5/2}\sqrt{\frac{\Delta_b}{\Delta_p}}\sqrt{\frac{C}{-B}}, \quad (26)$$

in which case, under condition (24), we have

$$B = -\frac{1}{2}\sqrt{\frac{\pi}{2}}\gamma^{-2}\xi^3 e^{-\xi^2/2}. \quad (27)$$

Consequently, in terms of the Langmuir frequency of the beam electrons, the inequality $|\delta x| \ll |B|$ takes the form

$$\frac{\omega_b}{\omega_p}\sqrt{\frac{\Delta_b}{\Delta_p}} \ll \gamma^{-1/2}\xi^{9/2}e^{-\frac{3}{4}\xi^2}. \quad (28)$$

We can see that the dissipative instability in the system is triggered by an electron beam with a very low density (lower than the density of plasma electrons whose velocities lie in a narrow interval around the velocity u). In the opposite asymptotic limit, the maximum amplification coefficient is equal to

$$\delta x = \frac{1-i\sqrt{3}}{2}\left(\frac{1}{2}\frac{\omega_b^2}{\omega_p^2}\gamma^{-5}\frac{\Delta_b}{\Delta_p}C\right)^{1/3}. \quad (29)$$

As the resonant frequency ω_p shifts toward lower frequencies, the amplification coefficient (29) in a hot plasma decreases only by a factor of $(1 - 3\gamma^{-2}\xi^{-2})^{1/3}$ rather than $C^{1/3}$. Solution (29) is valid under the conditions

$$2\left(\frac{\pi}{6}\right)^{3/2}\gamma^{-1}\xi^9 e^{-\frac{3}{2}\xi^2} \ll \frac{\omega_b^2}{\omega_p^2}\frac{\Delta_b}{\Delta_p} \ll \frac{1}{\sqrt{3}\gamma}. \quad (30)$$

Let us consider the case $B = 0$, which corresponds to the condition

$$\kappa_\perp^2 u^2\gamma^2 = [1-(2\gamma^2-3)\xi^{-2}]\omega_p^2. \quad (31)$$

This condition gives $A = \xi^{-2}$. In the asymptotic limit $|\delta x| \ll A$, the amplification coefficient has the form

$$\delta x = -\frac{i}{\sqrt{2}}\frac{\omega_b}{\omega_p}\xi\gamma^{-5/2}\sqrt{\frac{\Delta_b}{\Delta_p}C}. \quad (32)$$

Solution (32) applies to low-current beams such that

$$\frac{\omega_b}{\omega_p}\sqrt{\frac{\Delta_b}{\Delta_p}} \ll \sqrt{2}\gamma^{5/2}\xi^{-3}. \quad (33)$$

In the opposite asymptotic limit, we arrive at the maximum amplification coefficient (29).

If we neglect exponentially small terms that account for Landau damping by fast plasma electrons, then we find that Eq. (22) has real coefficients and immediately obtain the threshold for the onset of instability in a hot plasma:

$$1-\frac{\kappa_\perp^2 u^2\gamma^2}{\omega_p^2} \geq -3\left[\frac{\omega_b^2}{\omega_p^2}\gamma\frac{\Delta_b}{\Delta_p}C^{-2}\right]^{1/3} - 3\xi^{-2}. \quad (34)$$

The threshold plasma density n_p decreases with increasing thermal velocity v_T, whose value turns out to be somewhat underestimated because energy transfer from the wave to the plasma is ignored.

Now, we turn to a model in which the cold electron plasma component moves as a single entity with velocity v_p. Since we are interested only in the Cherenkov instability (as in the case of an immobile hot plasma), we again represent the desired solution to the dispersion relation in form (19). Under condition (20), we arrive at the cubic equation

$$(\delta x)^2\left[\delta x + \frac{1}{2\gamma^2}\frac{1-\frac{\kappa_\perp^2 u^2\gamma^2}{\omega_p^2}\left(1+\frac{v_p}{u}\right)^2}{1-\frac{\kappa_\perp^2 u^2}{\omega_p^2}\left(1+\frac{v_p}{u}\right)\frac{v_p}{u}}\right] = -\frac{1}{2}\frac{\left(1+\frac{v_p}{u}\right)^2}{1-\frac{\kappa_\perp^2 u^2}{\omega_p^2}\left(1+\frac{v_p}{u}\right)\frac{v_p}{u}}\frac{\omega_b^2}{\omega_p^2}\gamma^{-5}\frac{\Delta_b}{\Delta_p}. \quad (35)$$

which leads to the single-particle Cherenkov resonance condition

$$\omega_p^2 = \kappa_\perp^2 u^2\gamma^2\left(1+\frac{v_p}{u}\right)^2, \quad (36)$$

and the maximum amplification coefficient

$$\delta x = \frac{1-i\sqrt{3}}{2}\left[\frac{1}{2}\frac{\left(1+\frac{v_p}{u}\right)^3}{1+\frac{uv_p}{c^2}}\frac{\omega_b^2}{\omega_p^2}\gamma^{-5}\frac{\Delta_b}{\Delta_p}\right]^{\frac{1}{3}}. \quad (37)$$

The condition for wave amplification in a plasma, or, equivalently, the condition for the dispersion relation (35) to have complex roots, takes the form

$$\frac{1-\frac{\kappa_\perp^2 u^2\gamma^2}{\omega_p^2}\left(1+\frac{v_p}{u}\right)^2}{\left[1-\frac{\kappa_\perp^2 u^2}{\omega_p^2}\left(1+\frac{v_p}{u}\right)\frac{v_p}{u}\right]^{\frac{2}{3}}} \geq -3\gamma^2\left[\left(1+\frac{v_p}{u}\right)^2\frac{\omega_b^2}{\omega_p^2}\gamma^{-5}\frac{\Delta_b}{\Delta_p}\right]^{\frac{1}{3}}. \quad (38)$$

If the plasma electrons move from the collector toward the cathode, then the instability threshold in terms of ω_p increases; in contrast, if the plasma electrons move from the cathode toward the collector, then the instability threshold in terms of ω_p decreases. The resonant plasma frequency ω_p shifts in an analogous manner.

3. Here, we consider a spatially separated beam and plasma in the long-wavelength limit $k_\perp R \ll 1$. In this case, we have

$$\begin{aligned} \kappa_b^{-2}(\alpha, \zeta) &= \frac{S_b}{S_p}\kappa_\perp^{-2}\tilde{G}, \\ \kappa_b^{-2}(\alpha, \beta) &= \frac{S_b}{S_p}\kappa_\perp^{-2}(\tilde{G}-1), \end{aligned} \tag{39}$$

where $S_\alpha = 2\pi r_\alpha \Delta_\alpha$ is the cross-sectional area of the beam ($\alpha = b$) or the plasma ($\alpha = p$). The integral over the region where the plasma and beam fields overlap is equal to

$$\tilde{G} = \frac{\ln(R/r_b)}{\ln(R/r_p)}. \tag{40}$$

We write Eq. (14) in terms of δx and then reduce it to the cubic equation

$$\begin{aligned} (\delta x)^3 + \Delta(\delta x)^2 + \varepsilon\left[\frac{4\gamma^2 + G}{2\gamma^2 + G} - (2\gamma^2\Delta + 1)\tilde{G}\right]\delta x \\ + \varepsilon\left(-\tilde{G}\Delta + \frac{1}{2\gamma^2 + G}\right) = 0. \end{aligned} \tag{41}$$

Here, we have introduced the notation

$$\varepsilon = \frac{\omega_b^2\gamma^{-5}}{\kappa_\perp^2 u^2}\frac{S_b}{S_p}, \tag{42a}$$

$$\nu^{-1} = \frac{\omega_p^2}{\kappa_\perp^2 u^2}\omega^2(2Q + \gamma^{-2}Q'), \tag{42b}$$

where $Q = K(\omega, \omega/u)$, $Q' = (\omega/u)K_k'(\omega, \omega/u)$, $G = Q'/Q$, and the prime denotes the derivative with respect to k (d/dk). We also denote the frequency detuning by

$$\Delta = \frac{1}{2\gamma^2 + G} - \nu. \tag{43}$$

Under the assumption that the coefficients of Eq. (41) are real, we arrive at the following condition for the existence of complex roots:

$$\Delta \geq -3\left[\frac{\varepsilon}{4}\left(-\tilde{G}\Delta + \frac{1}{2\gamma^2 + G}\right)\right]^{1/3}. \tag{44}$$

For $\tilde{G} > 1$, the threshold value of ω_p decreases. However, the threshold value of ω_p cannot be made arbitrarily small by increasing $\tilde{G}$. The reason is that our approximation fails to describe the case in which $\tilde{G}$ values are large, i.e., in which the plasma is close to the waveguide wall and interacts with the beam only slightly. For a low-density beam such that

$$\varepsilon \ll \frac{4}{27}\frac{\tilde{G}^{-3}}{(2\gamma^2 + G)^2}, \tag{45}$$

condition (44) becomes

$$\Delta \geq -3\left[\frac{\varepsilon}{4}\frac{1}{2\gamma^2 + G}\right]^{1/3}. \tag{46}$$

As in the case when the beam and plasma have the same radius, the effect of the beam on the threshold plasma density is described by the law $\omega_b^{3/2}$ [5]. For $G = 0$, $\tilde{G} = 1.58$ (which corresponds to $R = 1.8$ cm, $r_b = 0.6$ cm, and $r_p = 0.9$ cm), and $\gamma = 2$, we obtain $\varepsilon \ll 5.87 \times 10^{-4}$. When

$$\frac{4}{27}\frac{\tilde{G}^{-3}}{(2\gamma^2 + G)^2} \ll \varepsilon \ll 1, \tag{47}$$

we arrive at a condition other than condition (44):

$$\Delta \geq -\frac{3}{2}\sqrt{3\varepsilon\tilde{G}}. \tag{48}$$

In this case, the effect of the beam on the threshold plasma density is described by a linear law. For the experimental conditions of [1], we have $\varepsilon = 7 \times 10^{-3}$; this indicates that the threshold plasma density satisfies condition (48).

4. In conclusion, we compare our results with the experimental data of [1]. In those experiments, the plasma was created by exciting xenon discharges in a device operated with a hot cathode. The plasma temperature was about 3 eV, and the maximum electron energy spread, according to different estimates, did not exceed 10 eV. The corresponding velocity spread of the plasma electrons is $\Delta v = 1.9 \times 10^5$ m/s, the correction being $\Delta v/u = 7 \times 10^{-4}$. Consequently, in the linear stage of development of an instability in such a plasma, kinetic effects play an insignificant role. The stochastic motion of plasma electrons can manifest itself only in the nonlinear instability stage. When the excited radiation is broadband, the plasma is "heated" due to the stochastization of electron trajectories in the field of many waves; as a result, the resonance condition (24) changes.

In finite-length systems (cavities), the instabilities may also change their nature. The reason for this is that, in a plasma cavity, the only instability that may develop in a plasma whose density is just below the threshold is a nonresonant instability, which cannot be used to accelerate charged particles and occurs regardless of whether the Cherenkov resonance conditions are satisfied or not [6, 7]. The onset of this instability at the plasma branch of the natural waves of the cavity leads to a strong plasma heating due to the stochastization of electron trajectories in the field of many waves [8, 9]. As was shown in [8, 9], such plasma heating is very

efficient and may trigger the Cherenkov instability. However, it should be recognized that the nonresonant instability develops on long time scales, so that this heating effect can be observed only when the beam duration is sufficiently long.

In actual experiments, the plasma current from the cathode toward the collector is about $I_p = 100$ A. For the plasma density $n_p = 3 \times 10^{13}$ cm^{-3}, plasma thickness $\Delta_p = 0.1$ cm, and plasma radius $r_p = 1$ cm, this current is carried by the plasma electrons moving with the directed velocity $v_p = 3.5 \times 10^5$ m/s. Nevertheless, the plasma electron velocity may be substantially higher, because the front of the beam injected into the cavity pushes the plasma toward the collector. The effect of the acceleration of plasma electrons in the field of a beam with an unneutralized charge may become important when the plasma density is low, i.e., when the plasma frequency ω_p is close to the threshold. In this case, the Cherenkov instability can occur due to Doppler shift even when the plasma density is below the threshold. The Cherenkov instability continues to grow until the beam front reaches the collector and causes secondary emission, which leads to the current neutralization of the beam. Because of this, the plasma current induced by secondary emission is carried by the electrons moving from the collector toward the cathode with the directed velocity

$$v_p \approx \frac{n_b S_b}{n_p S_p} u. \tag{49}$$

Under the experimental conditions of [1], specifically, $n_b = 1.2 \times 10^{12}$ cm^{-3}, $\Delta_b = 0.1$ cm, $r_b = 0.6$ cm (which corresponds to $I_b = 2.3$ kA), $n_p = 4 \times 10^{12}$ cm^{-3}, $\Delta_p = 0.1$ cm, and $r_p = 0.9$ cm, this directed velocity is about $v_p \approx 0.2u$. As a result, the electron plasma density turns out to be below the threshold, so that the time scale on which the instability develops is equal in order of magnitude to the electron transit time L/u and, therefore, depends on the cavity length. Hence, when the plasma frequency ω_p is close to the threshold, it is only in long systems that the instability has enough time to develop. For long cavities, this effect leads to a decreasing dependence of the threshold value of ω_p on the cavity length L, thereby explaining the corresponding dependence revealed in the experiments of [1].

REFERENCES

1. P. S. Strelkov and D. K. Ul'yanov, Fiz. Plazmy **26**, 329 (2000) [Plasma Phys. Rep. **26**, 303 (2000)].
2. M. V. Kuzelev, O. V. Lazutchenko, and A. A. Rukhadze, Izv. Vyssh. Uchebn. Zaved., Radiofiz. **42**, 958 (1999).
3. I. N. Kartashov, M. A. Krasil'nikov, M. V. Kuzelev, and A. A. Rukhadze, in *Proceedings of the XXVIII Zvenigorod Conference on Plasma Physics and Controlled Nuclear Fusion, 2001*, p. 245.
4. A. F. Alexandrov, L. S. Bogdankevich, and A. A. Rukhadze, *Principles of Plasma Electrocdynamics* (Vysshaya Shkola, Moscow, 1978; Springer-Verlag, Berlin, 1984).
5. M. V. Kuzelev and A. A. Rukhadze, in *Electrodynamics of Dense Electron Beams in a Plasma* (Nauka, Moscow, 1990), p. 336.
6. D. N. Klochkov and M. Yu. Pekar, Fiz. Plazmy **23**, 650 (1997) [Plasma Phys. Rep. **23**, 602 (1997)].
7. D. N. Klochkov, M. Yu. Pekar, and A. A. Rukhadze, Kratk. Soobshch. Fiz., No. 4, 7 (1999).
8. V. A. Buts, O. V. Manuĭlenko, K. N. Stepanov, and A. P. Tolstoluzhskiĭ, Fiz. Plazmy **20**, 794 (1994) [Plasma Phys. Rep. **20**, 714 (1994)].
9. V. A. Buts, A. N. Kupriyanov, O. V. Manuĭlenko, and A. P. Tolstoluzhskiĭ, Izv. Vyssh. Uchebn. Zaved., Prikl. Nelineĭnaya Din. **1**, 57 (1993).

Translated by I. A. Kalabalyk

Plasma Physics Reports, Vol. 28, No. 1, 2002, pp. 63–70. Translated from Fizika Plazmy, Vol. 28, No. 1, 2002, pp. 68–76.
Original Russian Text Copyright © 2002 by Starostin, Boller, Peters, Udalov, Kochetov, Napartovich.

LOW-TEMPERATURE PLASMA

RF Discharge in CO_2 Laser Mixtures at Moderate Pressures

S. A. Starostin*, K. J. Boller*, P. J. M. Peters*, Yu. B. Udalov, I. V. Kochetov***, and A. P. Napartovich*****

**University of Twente, 7500 AE Enschede, The Netherlands*

***Nederlands Center for Laser Research, 7500 CK Enschede, The Netherlands*

****Troitsk Institute for Innovation and Fusion Research, Troitsk, Moscow oblast, 142190 Russia*

Received August 2, 2001

Abstract—The voltage–power characteristics and spatial structure of an RF discharge in the mixtures of CO_2 and N_2 molecular gases with He at total pressures of tens of torr are studied. One-dimensional numerical simulations of an RF discharge are carried out within two approaches: (i) the distribution function and the related kinetic coefficients are assumed to be functions of the local reduced field, and (ii) the kinetic coefficients are functions of the electron mean energy, which is calculated with allowance for both electron heat conduction and diffusion. The latter approach is shown to better describe the existing experimental dependence of the discharge voltage and the phase shift between the discharge current and voltage on the driving power. © *2002 MAIK "Nauka/Interperiodica".*

1. INTRODUCTION

Recently, great progress has been achieved in creating CO_2 and CO capillary and slab lasers excited by a capacitive transverse RF discharge (see, e.g., [1–3]). In these lasers, the gas mixtures are cooled via electrodes, to which an RF driving voltage is applied. The properties of this type of discharge were investigated experimentally in [4–8]. The discharge operated in capillaries (used in laser devices [4]), plasma slabs [5, 8], and specially designed cells [6, 7]. In particular, the dependences of the discharge voltage and the phase shift between the discharge voltage and current on the discharge current and the driving power were studied in [6, 7]. To attain a high lasing power and efficiency, it is necessary that the gas mixture pressure p be tens of torr, the driving field frequency f be in the range from tens to hundreds of megahertz, and the interelectrode spacing be d = 0.1–0.25 cm [1, 2]. Under these conditions, numerical simulations of an RF discharge are rather complicated because of the large value of the pd parameter. Early studies on numerical simulations of an RF discharge are reviewed in [9]. Analytical models describe an RF discharge only qualitatively [10]. In a number of papers, the characteristics of an RF discharge were calculated numerically (see, e.g., [5, 11, 12] and review [9]). However, no comparative studies of the results of numerical simulations and available experimental data have been made.

It is generally believed that, at elevated gas pressures, the nonlocal character of the electron energy distribution function can be neglected throughout the entire volume, including the sheaths. However, a true threshold pressure for the applicability of the local model, as well as the dependence of this pressure on various parameters (gas composition, discharge power, etc.), is still unknown.

The aim of this study is to investigate this problem under conditions typical of the active medium of a slab CO_2 laser.

To this end, numerical simulations are performed using two different one-dimensional models of an RF discharge. Both of them include Poisson's equation for the electric field, transport equations for electrons and positive and negative ions, and the heat conduction equation for the gas temperature in the discharge gap. In the first model (referred to as local), the rates of electron production and loss and the electron transport coefficients are assumed to be functions of the local value of the reduced electric field E/N (where E is the electric field and N is the density of neutral particles). The local model is identical to the model of [11]. In the second model (referred to as nonlocal), described in detail in [9], the rates of electron production and loss and the transport coefficients are assumed to be functions of the electron mean energy. To determine this energy, the balance equation with allowance for electron heat conduction and diffusion is solved. Hence, possible deviations of the electron mean energy and the accompanying plasma characteristics from those determined by the local electric field are taken into account.

2. EXPERIMENTAL SETUP

The rms voltage is measured directly at the CO_2 laser electrodes, which are the same as those used in experiments on optimizing the laser parameters (see [13] and references therein). The discharge gap dimensions are d = 0.2 cm, a = 1.5 cm, and L = 37 cm. A slab is formed by gold-coated copper electrodes and side

1063-780X/02/2801-0063$22.00 © 2002 MAIK "Nauka/Interperiodica"

walls made from aluminum oxide. A set of matching coils is connected in parallel to the electrodes to ensure both a homogeneous electric field along the electrodes and the resonant matching to the power supply. One electrode is grounded, whereas the other is connected to a 100-MHz voltage source. A $CO_2 : N_2 : He$ (1 : 1.5 : 12) + 5% Xe gas mixture is used.

The measurements were carried out using a Textronics TDS 640A oscillograph with a bandwidth of 500 MHz and a high-voltage probe with an input impedance of 20 MΩ, 2 pF and an output impedance of 1 MΩ. To measure the RF voltage, the probe was calibrated in the frequency range of interest by measuring the voltage drop across a 50-Ω load resistor connected to the RF generator. In the absence of the reflected signal (the incident and reflected RF powers were measured with a Werlatone C2310 directional coupler), all the power is dissipated in the load and the voltage is $V = \sqrt{wR}$, where w is the power dissipated in the load and R is the load resistance. Based on these measurements, the voltage calibration factor was determined.

3. DISCHARGE MODEL

Following [11], when simulating an RF discharge, we took into account one positive and one negative ion species. The continuity equations for these components were solved together with the continuity equation for the electron density and Poisson's equation for the electric field. The continuity equations took into account both drift and diffusion. The gas temperature was determined from the time-independent heat conduction equation.

Note that the results of numerical simulations of the discharge parameters (especially the phase shift between the discharge current and voltage) are sensitive to the exact value of the thermal conductivity of the gas mixture, which was determined from the thermal conductivities of the individual components by the procedure described in [14]. The thermal conductivities of the individual components and their temperature dependences were taken from [15].

When simulating an RF discharge, we used the local and nonlocal models. In the local model, the rates of ionization and electron attachment, the electron mobility, and the coefficients of electron recombination and diffusion depend only on the local E/N value, which is the case of [11].

Under the conditions of interest, the rate of electron momentum relaxation in the plasma of an RF discharge in a $CO_2 : N_2 : He$ mixture is two orders of magnitude higher than the frequency of the driving field. Near the electrodes, the rate of electron energy relaxation is also higher than the frequency of the driving field; however, in the middle of the discharge gap, they can be of the same order of magnitude. Generally, the electron energy relaxation length is 10^{-3} cm. It will be shown below that the thickness of the sheaths (where the electric field sharply increases, whereas the electron density decreases) is $\sim 10^{-2}$ cm. Taking into account the nonsteady and nonlocal character of the kinetic coefficients requires solving the space- and time-dependent Boltzmann equation, which is a rather complicated problem (in [16], such a problem was solved for the case of pure He). Although the electron energy distribution function is different from the Maxwellian one, it is possible to introduce the electron mean energy, regarding it as the main characteristic of the distribution function. We assume that all the coefficients depend only on this mean energy, as was done in [9]. In this case, in order to find the electron mean energy, it is necessary to solve the equation for this energy with allowance for electron heat conduction. At every instant, the electron mean energy is determined at any point of the interelectrode gap. Then, the ionization and attachment rate constants are calculated as functions of this energy (these functions were determined beforehand by numerically solving the Boltzmann equation for the electron energy distribution function). The transport coefficients, which are used to solve the time-dependent equation for the electron mean energy and the continuity equations, are also found. This nonlocal model was previously used in modeling an RF discharge in a He : Ar : Xe mixture [17].

The equations are supplemented with the relevant boundary and initial conditions. The discharge voltage is derived from a given RF power. To solve the set of equations numerically, the finite-difference scheme, which was proposed in [18] for describing processes in semiconductor devices and first used in [19] for simulating an RF discharge, is applied.

In numerical simulations, we used a spatial mesh with a nonuniform cell size, which decreased when approaching the electrodes. In general, the number of such spatial cells was about 100. A steady state was reached after several thousands of RF cycles, which took about 10 h of processing time of an IBM-compatible PC with a Pentium III-733 processor.

4. RESULTS AND DISCUSSION

Only a few experimental studies of a planar RF discharge in CO_2-containing mixtures used in CO_2 lasers are available in the literature.

In [8], measurements of the rms discharge voltage were carried out at lower specific driving powers and in a gas mixture ($CO_2 : N_2 : He : Xe = 1 : 1 : 3 : 0.25$) with a higher content of molecular gases than in our study. The results of numerical simulations with the use of the above two models together with the experimental data from [8] are shown in Fig. 1. At low specific powers, both models provide similar results. As the driving power increases, the nonlocal model shows a more rapid increase in the rms discharge voltage and better matches the experimental data than the local model.

In [6, 7], an RF discharge ran in the specially designed cells—discs with diameters D = 3 and 1.7 cm and interelectrode spacing of 0.25 and 0.175 cm, respectively. In addition to the rms discharge voltage, the phase shift between the discharge current and voltage as a function of the discharge input power was also measured. The measurements were performed in a wide pressure range p = 20–130 torr in the gas mixture $CO_2 : N_2 : He : Xe = 19 : 19 : 57 : 5$. Note that, in [7], the measurements were carried out with a refined technique and the measured phase shift was lower than in [6].

To find the phase shift between the discharge current and voltage, two methods for processing simulation results were used: spectral decomposition and the least squares method. Since, in simulations, the voltage at the electrodes was specified as sinusoid (its amplitude was determined by the given driving power), there were high-frequency harmonics in the calculated discharge current. An example of the simulated discharge current is shown in Fig. 2. The spectral decomposition was carried out with the help of the fast Fourier transform [20] and a numerical code kindly provided by N.N. Elkin. Based on the spectral decomposition results, the phase shift between the discharge voltage and the fundamental harmonic of the current was determined. The nonlinear distortion factor, which was determined as the ratio of the sum of the squared amplitudes of higher current harmonics to the squared amplitude of the fundamental harmonic, is ~1%. In the least squares method, the discharge current was approximated by the function $J_d = J_{d0}\sin(2\pi ft + \phi)$, where f is the known frequency of the driving field. As a result, the amplitude of the discharge current density J_{d0} and the phase shift ϕ were determined. The difference between the phase shifts determined by the two different methods did not exceed one-tenth of a degree.

Figure 3a presents the measured [7] and simulated rms discharge voltages versus the driving power for different gas mixture pressures. The solid and dashed lines show the simulation results obtained with the nonlocal and local models, respectively. It is seen that the nonlocal model better describes the experimental data, especially at reduced pressures. The difference between the results of the alternative models is largest at a pressure of 20 torr and, then, decreases with increasing pressure. Figure 3b presents the phase shift between the discharge voltage and current. The symbols show the experimental data from [7], and the curves show the simulation results obtained with the nonlocal (solid line) and local (dashed line) models. With the exception of the lowest pressure range (near 20 torr), the nonlocal model describes fairly well the experimental data from [7]. The local model predicts a phase shift much lower than the measured one.

We measured the rms discharge voltage as a function of the discharge input power in the $CO_2 : N_2 : He = 1 : 1.5 : 12 + 5\%$ Xe gas mixture with a higher helium content at two mixture pressures: 50 and 120 torr. The experimental and simulation results are shown in Fig. 4. As was expected, the difference between the rms discharge voltages calculated using the local (curves *1*, *2*) and nonlocal (*1*', *2*') models decreases as the gas mixture pressure increases. It is notable that, under the given conditions, the local model predicts an increase in the rms discharge voltage with gas pressure (cf. curves *1*', *2*') at a constant driving power, which disagrees with the experimental data. The nonlocal model predicts a decrease in the rms discharge voltage with increasing gas mixture pressure (cf. curves *1*, *2*), which is in agreement with the experiment (see, e.g., review

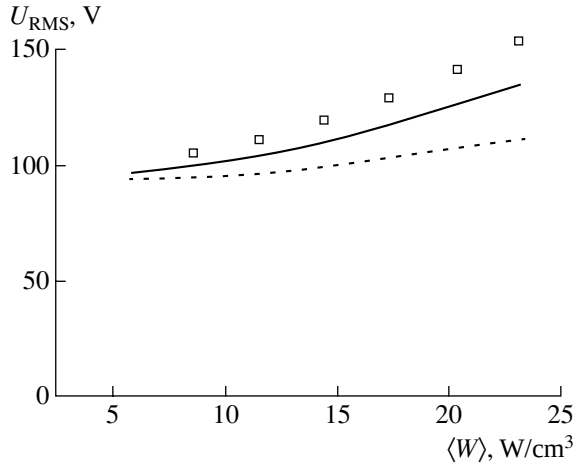

Fig. 1. Discharge voltage U_{RMS} vs. discharge power density for the mixture $CO_2 : N_2 : He : Xe = 1 : 1 : 3 : 0.25$ at p = 50 torr, d = 0.25 cm, L = 23 cm, a = 3 cm, and f = 81 MHz. The symbols show the experimental data from [8]; the curves show the simulation results obtained with the nonlocal (solid line) and local (dashed line) models.

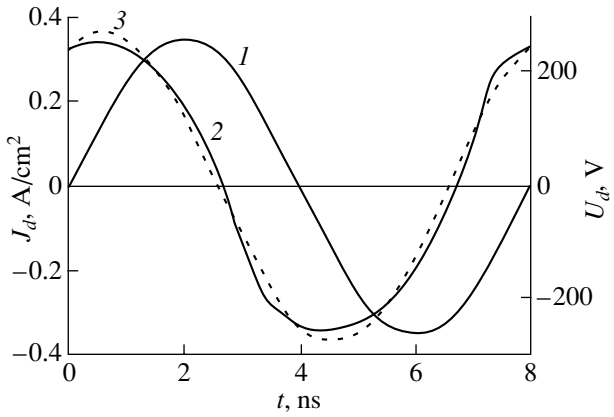

Fig. 2. Time evolution of (*1*) the discharge voltage, (*2*) calculated current, and (*3*) current approximated by $J_d = J_{d0}\sin(2\pi ft + \phi)$ for the mixture $CO_2 : N_2 : He : Xe = 19 : 19 : 57 : 5$ at p = 130 torr, d = 0.175 cm, D = 1.7 cm, f = 125 MHz, and $\langle W \rangle$ = 123 W/cm^3.

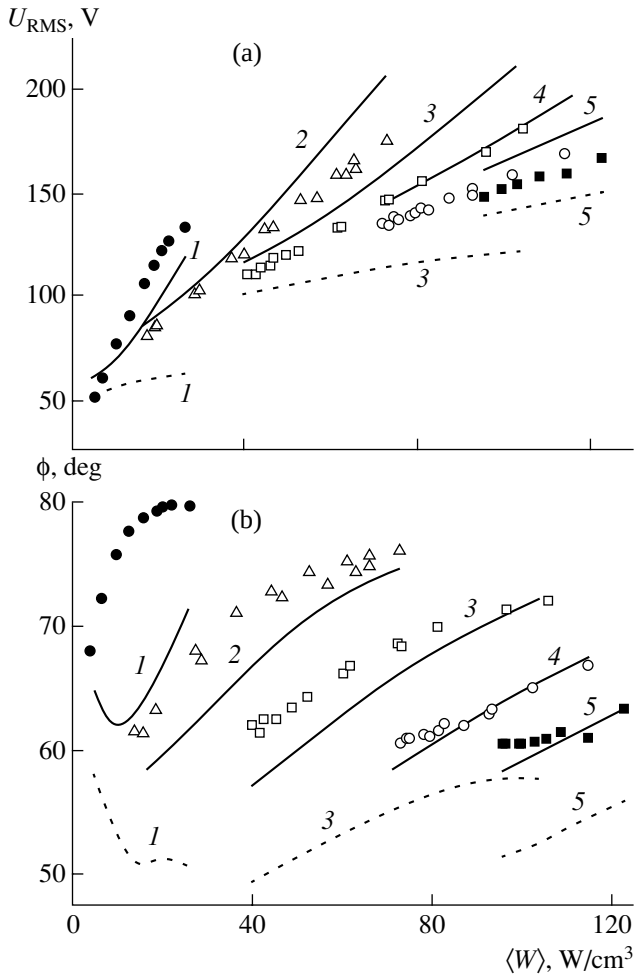

Fig. 3. (a) Discharge voltage U_{RMS} and (b) phase shift between the discharge current and voltage vs. discharge power density for the mixture $CO_2 : N_2 : He : Xe = 19 : 19 : 57 : 5$ at $d = 0.175$ cm, $D = 1.7$ cm, and $f = 125$ MHz. The symbols show the experimental data from [7] for $p = 20$ (closed circles), 40 (triangles), 70 (open squares), 100 (open circles), and 130 (closed squares) torr. The curves show the computation results obtained with the nonlocal (solid line) and local (dashed line) models for $p =$ (*1*) 20, (*2*) 40, (*3*) 70, (*4*) 100, and (*5*) 130 torr.

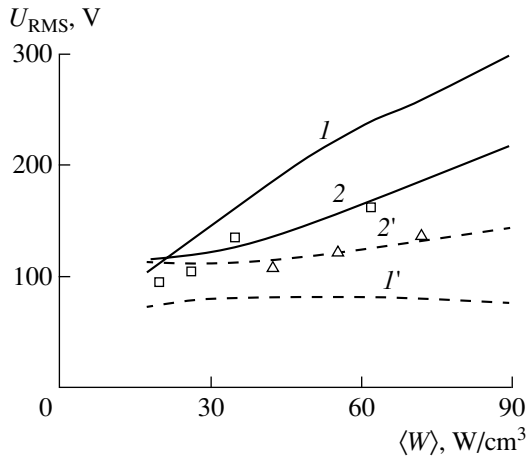

Fig. 4. Discharge voltage U_{RMS} vs. the discharge power density for the mixture $CO_2 : N_2 : He = 1 : 1.5 : 12 + 0.5\%$ Xe at $d = 0.2$ cm, $L = 37$ cm, $a = 1.5$ cm, and $f = 100$ MHz. The symbols show the experimental data for $p = 50$ (squares) and 120 (triangles) torr. The curves show the computation results obtained with the (*1*, *2*) nonlocal and (*1*', *2*') local models for $p =$ (*1*, *1*') 50 and (*2*, *2*') 120 torr.

[4]). This decrease is related to the fact that the rms discharge voltage is combined from the voltage drops across the positive column and electrode sheaths [10]. The rms reduced field $(E/N)_{RMS}$ in the middle of the discharge gap is determined by the balance between the electron production and loss and, according to numerical simulations (Fig. 6), depends slightly on the pressure and specific driving power; therefore, E increases with pressure p. Consequently, at a constant specific driving power $W = JE$, the discharge current density J decreases. Since the continuity of the total discharge current at the electrodes is ensured by the displacement current, the decrease in J leads to a reduction in $\partial E_{el}/\partial t \sim J$ and a subsequent decrease in both the electric field E_{el} in the sheath and voltage drop across the sheath. Hence, the quantity $U_{RMS} \simeq \sqrt{(E_{el}d)^2 + (E(d - d_{el}))^2}$ decreases with pressure if the second term in the radicand dominates. In the opposite case, U_{RMS} increases with pressure. Our calculations confirm this consideration.

In experiments [6, 7], the data processing made it possible to separate the voltage drops across the plasma and the sheaths; for this reason, further numerical simulations are carried out for the conditions of [7].

The reduced electric field E/N is an important parameter that determines both the energy fraction spent on the excitation of vibrational levels and the related efficiency of the lasers based on vibrational–rotational transitions. The profiles of the rms E/N are shown in Figs. 5a–5d for different driving powers and gas pressures. It is seen that, at a pressure of 20 torr, the local model (Fig. 5a) predicts narrower sheaths and a less pronounced sheath shrinking with increasing driving power than the nonlocal model (Fig. 5b). At a pressure of 130 torr, both models show similar E/N profiles (Figs. 5c, 5d).

As was discussed above and is seen in Fig. 5, the value of E/N in the middle of the discharge gap changes slightly with increasing driving power. The increase in the discharge input power leads to an increase in the electron density. As the gas mixture pressure decreases, the electron losses due to ambipolar diffusion start to dominate in the electron balance in the middle of the discharge gap. The dependence of the rms reduced electric field in the middle of the discharge gap on the electron density is shown in Fig. 6. At pressures of 70–130 torr, the difference between the E/N values calcu-

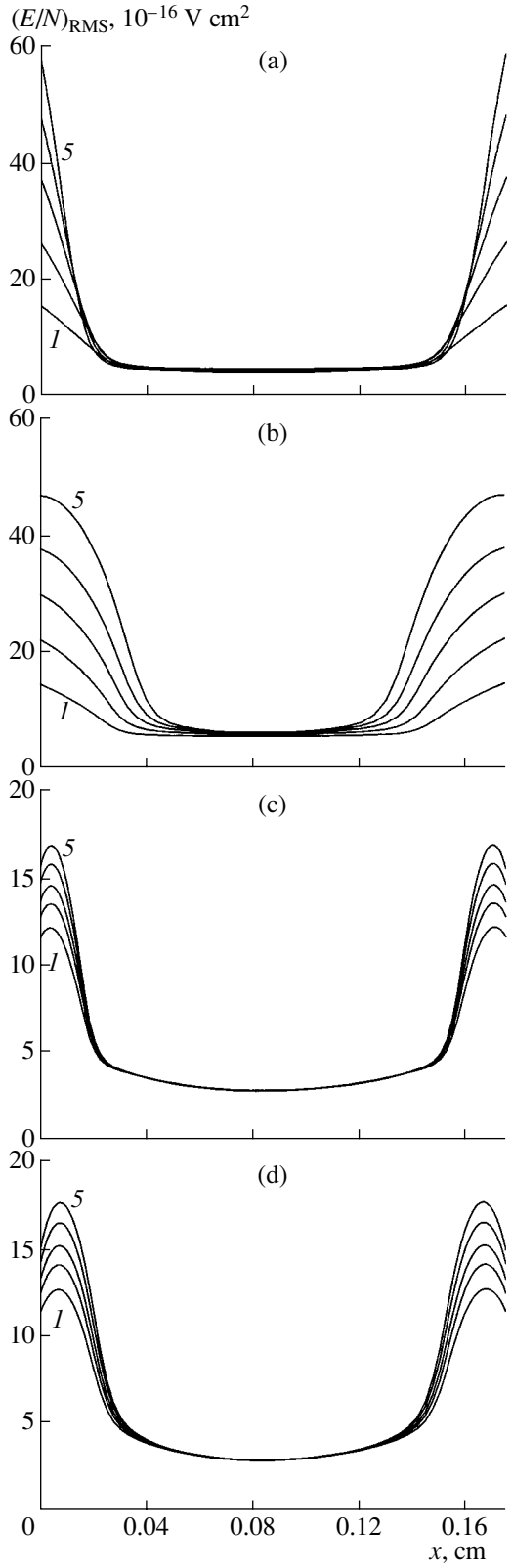

Fig. 5. Profiles of the rms reduced electric field $(E/N)_{RMS}$ within the (a, c) local and (b, d) nonlocal models: (a, b) p = 20 torr and $\langle W\rangle$ = (*1*) 5, (*2*) 10, (*3*) 15, (*4*) 20, and (*5*) 26 W/cm^3 and (c, d) p = 130 torr and $\langle W\rangle$ = (*1*) 96, (*2*) 104, (*3*) 110, (*4*) 117, and (*5*) 123 W/cm^3.

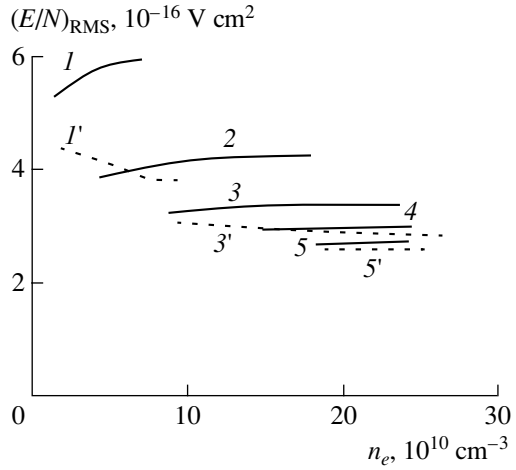

Fig. 6. Reduced electric field $(E/N)_{RMS}$ vs. electron density n_e (both in the middle of the discharge gap) calculated using the (*1–5*) nonlocal and (*1'*, *3'*, *5'*) local models for p = (*1*, *1'*) 20, (*2*) 40, (*3*, *3'*) 70, (*4*) 100, and (*5*, *5'*) 130 torr.

lated using the alternative models is small. As the pressure decreases to 20 torr, this difference becomes significant. As the pressure increases from 20 to 130 torr, the E/N value in the middle of the discharge gap decreases from 6×10^{-16} to 2.6×10^{-16} V cm^2. The local model predicts that E/N decreases with increasing electron density, whereas, according to the nonlocal model, the reduced field increases and this increase becomes less pronounced with increasing gas pressure.

The small signal gain profiles in molecular lasers depend on the profiles of the specific driving power. Figure 7 shows the profiles of the specific driving power W_{total} for different averaged specific driving powers $\langle W\rangle$ and gas mixture pressures p. As is the case of the reduced electric field, the W_{total} profiles calculated using the local and nonlocal models differ greatly at a gas mixture pressure of 20 torr (Figs. 7a, 7b) and are similar at a pressure of 130 torr (Figs. 7c, 7d). Simulations show that the corresponding sheaths occur in the profiles of the electron, positive ion, and negative ion densities. Note that, at a pressure of 20 torr and an average specific driving power of $\langle W\rangle$ = 26 W/cm^3, the local model predicts a significant increase in the specific driving power near the electrodes (Fig. 7a, curve *5*). This increase is related to the increase in the positive ion current. The profiles of the rms densities of the conduction current, positive and negative ion currents, and displacement current calculated using the local and nonlocal models for a pressure of 20 torr and $\langle W\rangle$ = 26 W/cm^3 are shown in Figs. 8a and 8b, respectively. In the middle of the discharge gap, the main contribution to the total current is provided by the electrons (Figs. 8a, 8b, curves *1*), whereas near the electrodes, the displacement current prevails (Figs. 8a, 8b, curves *2*). As the driving power increases, the electric field near

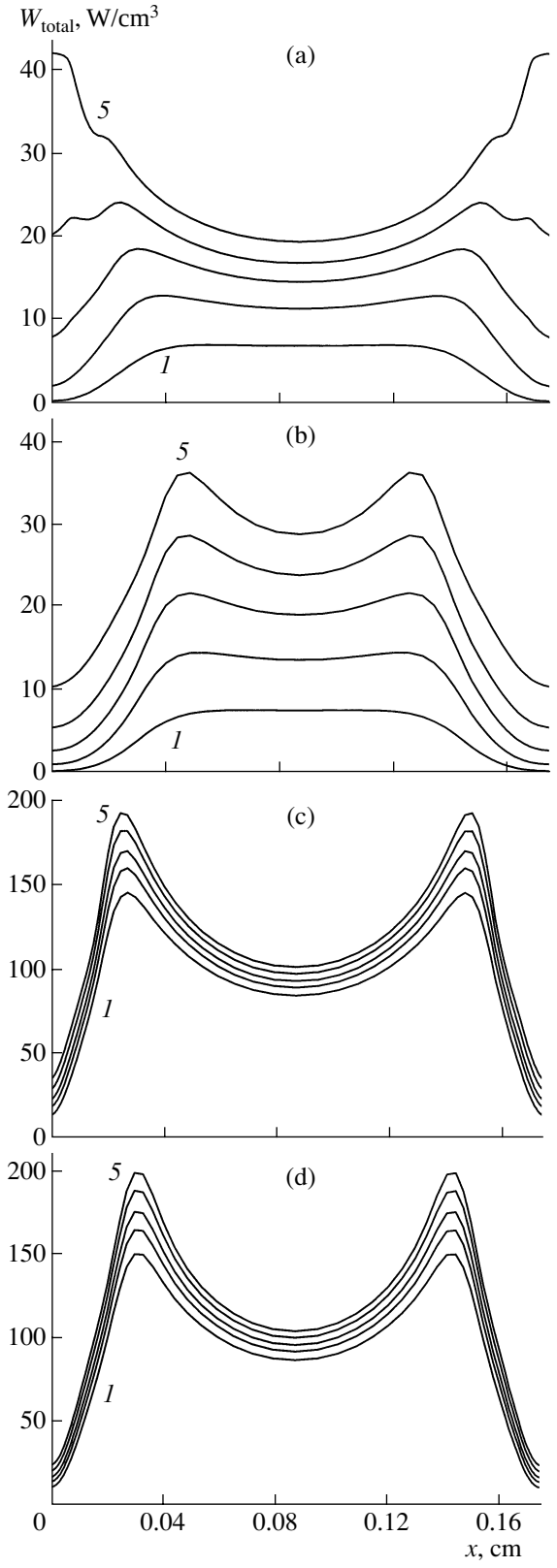

Fig. 7. Profiles of the discharge power density calculated using the (a, c) local and (b, d) nonlocal models: (a, b) p = 20 torr and $\langle W \rangle$ = (*1*) 5, (*2*) 10, (*3*) 15, (*4*) 20, and (*5*) 26 W/cm^3 and (c, d) p = 130 torr and $\langle W \rangle$ = (*1*) 96, (*2*) 104, (*3*) 110, (*4*) 117, and (*5*) 123 W/cm^3.

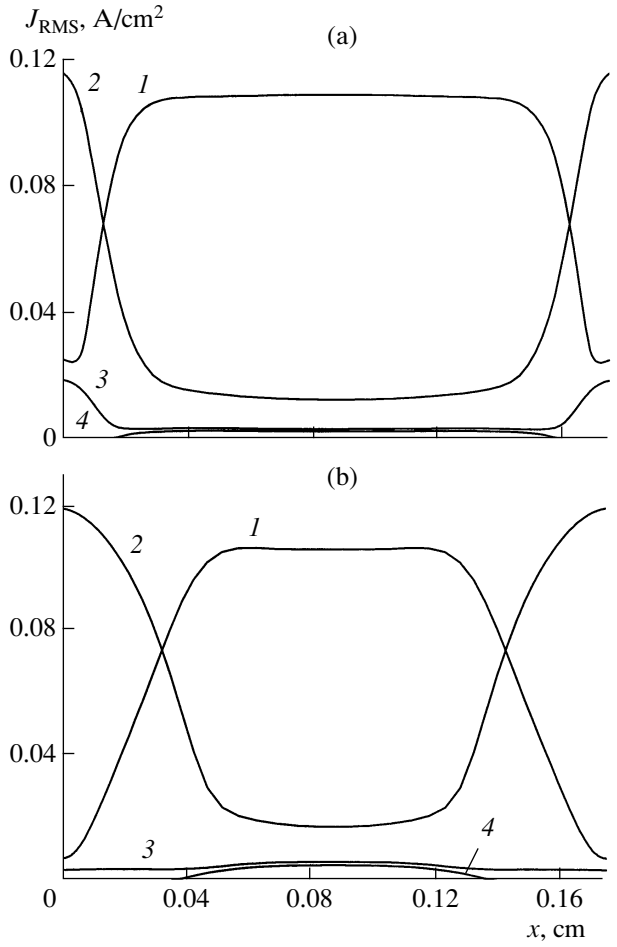

Fig. 8. Profiles of the rms current densities within the (a) local and (b) nonlocal models for p = 20 torr and $\langle W \rangle$ = 26 W/cm^3: (*1*) electron current, (*2*) displacement current, (*3*) positive ion current, and (*4*) negative ion current.

the electrodes also increases, thus ensuring a higher displacement current, which is proportional to $\partial E/\partial t$. The increase in the E/N near the electrodes leads to an increase in the ionization rate and the positive ion density; as a result, the fraction of the positive ion current in the total current becomes higher (Fig. 8a, curve *3*). Simulations predict that the fraction of the negative ion current is small (Figs. 8a, 8b, curves *4*).

In [6], a method for separating out the voltage drops across the plasma and sheaths from the discharge voltage was proposed. The method is based on the equivalent circuit of an RF discharge, including the sheath capacitance connected in series with the parallel connection of the plasma active resistance and the discharge gap capacitance, which is determined by the discharge geometry. Given the driving power, the discharge voltage, and the phase shift between the current and voltage, we can determine the rms voltage drops across the sheaths and plasma [6]. Using that procedure and based on the results of simulations, we determined

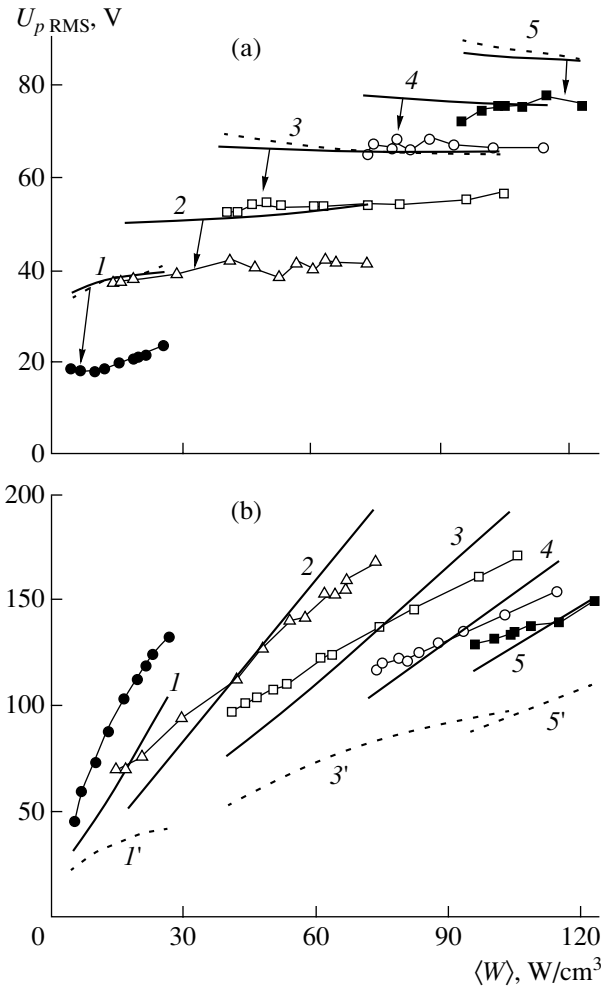

Fig. 9. Voltage drops (a) across the plasma, $U_{p\mathrm{RMS}}$, and (b) across the sheath, $U_{s\mathrm{RMS}}$, vs. discharge power density for the mixture $CO_2 : N_2 : He : Xe = 19 : 19 : 57 : 5$ at d = 0.175 cm and f = 125 MHz. The symbols show the experimental data from [7] for p = 20 (closed circles), 40 (triangles), 70 (open squares), 100 (open circles), and 130 (closed squares) torr. The curves show the simulation results obtained with the (solid line) nonlocal and (dashed line) local models for p = (*1*, *1*') 20, (*2*) 40, (*3*, *3*') 70, (*4*) 100, and (*5*, *5*') 130 torr.

these voltage drops, which are shown in Fig. 9 together with the experimental data (symbols) from [7]. In both the experiment and simulations, the voltage drop across the plasma slightly depends on the discharge input power (Fig. 9a). Both the local and nonlocal models give close results; however, the experimental data are somewhat lower. The sheath voltages calculated using the nonlocal model (Fig. 9b, solid lines) agree better with the experimental data than those obtained with the local model (Fig. 9b, dashed lines). Based on these results, the capacitance and thickness of the sheaths can be determined. This method for determining the sheath thickness is more suitable than the techniques based on the profiles of the rms reduced electric field, the profiles of the electron density averaged over the RF period, etc., because it does not require any extra criteria. The sheath thickness determined from the results of simulations by the nonlocal model agrees satisfactorily with the experimental data from [7]. Note that the local model underestimates the sheath thickness by a factor of 1.5–2.

5. CONCLUSION

A comparison of the results of numerical simulations by the local and nonlocal models with the experimental data from both the present study and the literature has shown that the nonlocal model better describes the dependences of the discharge voltage and the phase shift between the discharge current and voltage on the driving power in a wide pressure range. In particular, the nonlocal model predicts a decrease in the discharge voltage with increasing gas pressure at a constant driving power, which agrees with the experimental data, whereas the local model predicts the opposite behavior.

On the whole, the nonlocal model satisfactorily describes the dependences of the discharge voltage, the phase shift between the current and voltage, and the voltage drops across the plasma and electrode sheaths on the discharge input power.

ACKNOWLEDGMENTS

This study was supported in part by the Russian Foundation for Basic Research, project no. 01-02-17136.

REFERENCES

1. A. D. Colley, F. Villarreal, A. A. Cameron, *et al.*, in *Gas Laser: Recent Developments and Future Prospects*, Ed. by W. J. Witteman and V. N. Ochkin, NATO ASI Ser., Ser. 3 **10**, 89 (1995).
2. Yu. B. Udalov, S. N. Tskhai, P. J. M. Peters, *et al.*, in *Gas Laser: Recent Developments and Future Prospects*, Ed. by W. J. Witteman and V. N. Ochkin, NATO ASI Ser., Ser. 3 **10**, 73 (1995).
3. Jianguo Xin, Wang Zhang, and Wentao Jiao, Appl. Phys. Lett. **75**, 1369 (1999).
4. N. I. Lipatov, P. P. Pashinin, A. M. Prokhorov, and V. Yu. Yurov, Tr. Inst. Obshch. Fiz. Akad. Nauk SSSR **17**, 115 (1989).
5. R. Wester and S. Seiwert, J. Phys. D **24**, 1371 (1991).
6. P. P. Vitruk, H. J. Baker, and D. R. Hall, J. Phys. D **25**, 1767 (1992).
7. H. J. Baker, Meas. Sci. Technol. **7**, 1631 (1996).
8. V. V. Kun, V. G. Leont'ev, M. Z. Novgorodov, *et al.*, in *Proceedings of the XXII International Conference on Phenomena in Ionized Gases, Hoboken, 1995*, Vol. 3, p. 67.
9. J. P. Boeuf and Ph. Belenguer, in *Nonequilibrium Processes in Partially Ionized Gases*, Ed. by M. Capitelli and J. N. Bardsley (Plenum, New York, 1990), p. 155.

10. Yu. P. Raizer, M. N. Shneider, and N. A. Yatsenko, *High-Frequency Capacitive Discharge*, (Nauka, Moscow, 1995; CRC, London, 1995).
11. B. I. Ilukhin, Yu. B. Udalov, I. V. Kochetov, *et al.*, Appl. Phys. B: Lasers Opt. **B62**, 113 (1996).
12. V. N. Ochkin, W. J. Witteman, B. I. Ilukhin, *et al.*, Appl. Phys. B: Lasers Opt. **B63**, 575 (1996).
13. S. A. Starostin, Yu. B. Udalov, P. J. M. Peters, and W. J. Witteman, Appl. Phys. Lett. **77**, 21 (2000).
14. M. S. Syed Wahid and C. V. Madhusudana, Int. J. Heat Mass Transf. **43**, 4483 (2000).
15. *Handbook of Physical Quantities*, Ed. by I. S. Grigoriev and E. Z. Meilikhov (Énergoizdat, Moscow, 1991; CRC, Boca Raton, 1997).
16. V. A. Feoktistov, A. M. Popov, O. B. Popovicheva, *et al.*, IEEE Trans. Plasma Sci. **19**, 163 (1991).
17. S. A. Starostin, P. J. M. Peters, G. Van der Poel, *et al.*, Fiz. Plazmy **27**, 458 (2001) [Plasma Phys. Rep. **27**, 432 (2001)].
18. D. L. Sharfetter and H. K. Gummel, IEEE Trans. Electron Devices **ED-16**, 64 (1969).
19. J.-B. Boeuf, Phys. Rev. A **36**, 2782 (1987).
20. N. N. Elkin and A. P. Napartovich, *Applied Laser Optics* (TsNIIatominform, Moscow, 1989).

Translated by N. N. Ustinovskiĭ

Plasma Physics Reports, Vol. 28, No. 1, 2002, pp. 7–11. Translated from Fizika Plazmy, Vol. 28, No. 1, 2002, pp. 9–13.
Original Russian Text Copyright © 2002 by Akulina, Batanov, Berezhetskiĭ, Voronov, Gladkov, Grebenshchikov, Donskaya, Kolik, Larionova, Meshcheryakov, Sarksyan, Fedyanin, Kharchev, Khol'nov, Shchepetov.

MAGNETIC CONFINEMENT SYSTEMS

Measurements of the Microwave Power Absorbed by a Plasma during Second Harmonic ECR Heating in the L-2M Stellarator

D. K. Akulina, G. M. Batanov, M. S. Berezhetskiĭ, G. S. Voronov, G. A. Gladkov, S. E. Grebenshchikov, N. P. Donskaya, L. V. Kolik, N. F. Larionova, A. I. Meshcheryakov, K. A. Sarksyan, O. I. Fedyanin, N. K. Kharchev, Yu. V. Khol'nov, and S. V. Shchepetov

Institute of General Physics, Russian Academy of Sciences, ul. Vavilova 38, Moscow, 119991 Russia

Received May 24, 2001; in final form, July 19, 2001

Abstract—Comparative measurements of the absorbed microwave power are performed using the diamagnetic diagnostics and a multichannel diagnostics receiving the second harmonic electron cyclotron emission from the plasma. The specific features of the experiments and the results obtained are discussed. © *2002 MAIK "Nauka/Interperiodica".*

1. INTRODUCTION

Until the present time, the determination of the absorbed power, power deposition region, and plasma energy in experiments with high-power gyrotron complexes for electron heating has been one of the most challenging problems in high-temperature plasma research. The complexity of the problem of the power deposition in a plasma and heat transport in closed magnetic confinement systems is related to the variety of processes occurring in a high-temperature plasma when high-power microwave beams interact resonantly with electrons. These processes lead to the appearance of runaway electron beams ("tails") and electrons trapped in magnetic ripples, whose motion is unaffected by the rotational transform of magnetic lines. A more rapid loss of trapped electrons from the plasma leads to the generation of an electric field, which affects the electron ambipolar diffusion and, accordingly, the plasma thermal conductivity [1–4]. The study of these effects requires knowledge of the power deposition profiles.

In this paper, we present the results of comparative measurements of the plasma energy and the absorbed power from diamagnetic signals (at the instant when the microwave power is switched off) and from the temperature decay at different radii inside the plasma column. The temperature was measured with the help of multichannel superheterodyne detectors receiving the second harmonic X-mode electron cyclotron emission (ECE) from the plasma.

2. DESCRIPTION OF THE EXPERIMENT

The L-2M stellarator has two helical windings of different polarities ($l = 2$) and toroidal-field coils. The number of field periods is $N = 14$, the major radius of the torus is $R = 1$ m, and the mean plasma radius is $a_p = 0.11$ m. The plasma cross section is elliptical in configuration. In the cross sections of the stellarator (that will be referred to as "standard"), the ellipse is inclined to the major radius at an angle of $\alpha = 45°$, and it is inclined at an angle of $\alpha = 90°$ in the "nonstandard" cross section. A 75-GHz gyrotron with a power up to 300 kW was positioned in the standard section at the low-field side (LFS). Eight channels of a superheterodyne receiver [four channels in the range 68–74 GHz at the LFS and four channels in the range 76–81 GHz at the high-field side (HFS)] were located nearly 1.57 m from the gyrotron in a similar standard section, whereas the 71- and 77-GHz channels were positioned in the nonstandard section and received signals from the HFS. Band-pass filters were used to prevent the detectors from gyrotron radiation, so that the radiation within the band $\Delta f = 75.3 \pm 1.5$ GHz did not penetrate into the detector inputs.

The Shafranov (outward) shift of the magnetic axis ($R_{ax}(0) = 0.97$ m) during plasma heating amounts to $\Delta r = 1.8$–3.3 cm; i.e., the magnetic axis comes close to the center of the vacuum chamber ($R = 1$ m). The magnetic system produces a field configuration such that the resonance microwave-heating region lies in the middle of the slope of a local magnetic well. According to calculations, this leads to the appearance of stellarator magnetic "traps" asymmetrically profiled along the minor radius. The depth of the outer (with respect to the magnetic axis) traps is one order of magnitude greater than that for the inner traps. We may assume that the population of trapped electrons on the outside of the magnetic axis is greater than on the inside. As is known, the trapped electrons can give rise to a radial electric

1063-780X/02/2801-0007$22.00 © 2002 MAIK "Nauka/Interperiodica"

field and, thereby, can change the ambipolar neoclassical diffusion of the plasma. As the magnetic field $B(0)$ increases, the electron-temperature distribution across the plasma column becomes asymmetric because of the Shafranov shift [5].

The time evolutions of the plasma energy and its derivative (W and dW/dt) were determined from diamagnetic measurements [6–9].

We write the plasma-energy balance equation in the form [7]

$$\frac{dW}{dt} = P_{\text{abs}} - P_{\text{loss}}, \tag{1}$$

where P_{abs} is the heating microwave power and P_{loss} is the total loss power, including heat conduction, convection, charge exchange, and radiation and anomalous losses. For the steady state, we have $P_{\text{abs}} = P_{\text{loss}}$.

It is known that a jump in the diamagnetic-signal derivative after the microwave power is switched off determines the total absorbed power P_{abs} (provided that the loss power does not change during the jump):

$$P_{\text{abs}} = \frac{dW_e^{(t = t_0-)}}{dt} - \frac{dW_e^{(t = t_0+)}}{dt}, \tag{2}$$

where t_0 is the instant when the microwave power is switched off and W_e is the plasma energy. Assuming the heat flux to be continuous, the power deposition profile can be obtained from the local energy balance equation for electrons. At the instant when the microwave power is switched off, we have

$$P_{\text{abs}}(r) = \frac{\partial}{\partial t}\left(\frac{3}{2}n_e(r,t)T_e(r,t)\right)^{(t = t_0-)} - \frac{\partial}{\partial t}\left(\frac{3}{2}n_e(r,t)T_e(r,t)\right)^{(t = t_0+)}, \tag{3}$$

where n_e and T_e are the plasma density and the electron temperature, respectively. Integrating over the plasma volume, we can determine the value of the absorbed microwave power (P_{abs}).

When measuring the local temperature variations after the microwave power is switched off, it is important to appropriately choose the time interval Δt during which ΔT_e is measured in order to correctly determine $\partial T_e/\partial t$. If the observation time interval is too long, then other processes can affect the measurements of the power deposition profile. It is known that, in the power deposition region, the temperature decay curve shows a knee (the derivative jump) at the instant when the heating power is switched off (Fig. 1), whereas there is no

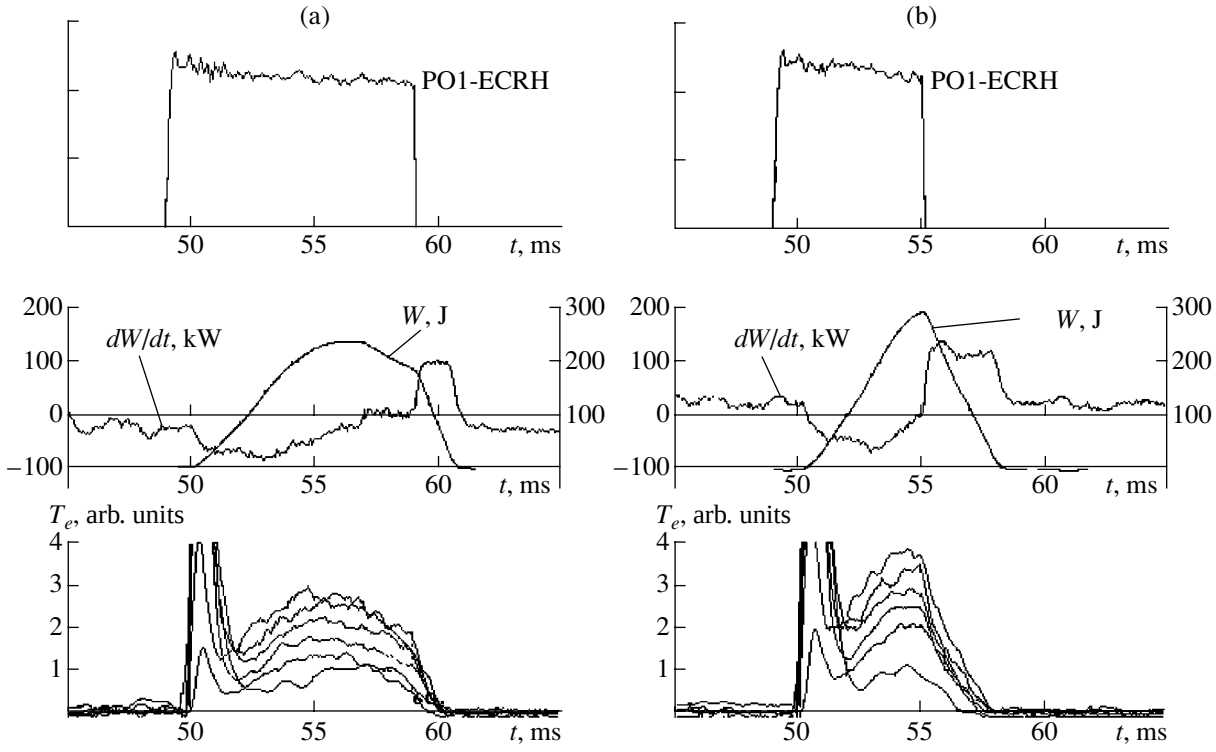

Fig. 1. Experimental time dependences of the heating power (PO1-ECRH), diamagnetic signal (W), diamagnetic-signal derivative (dW/dt), and electron temperature $T_e(f)$ for typical microwave pulses with Δt_{MW} = (a) 10 and (b) 6 ms.

such knee in the temperature decay curve at the plasma radii where heat is transferred via heat conduction and the maximum of the phase signal in power-modulation experiments is markedly delayed. In our previous experiments with amplitude microwave-power modulation [4], it was found that the characteristic modulation frequency of signals intended for determining the power deposition region in the L-2M stellarator should be no less than 4 kHz; consequently, the chosen time interval Δt in our experiments should be $\lesssim 250$ μs. With this modulation frequency, the measured profile of the absorbed power became consistent with the absorption parameters calculated for L-2M by ray tracing and with a kinetic model [10, 11]. The plasma density did not vary substantially over such a short observation interval.

3. EXPERIMENTAL RESULTS

Figures 1a and 1b show the curves describing the time behavior of the microwave power (PO1-ECRH), the diamagnetic signal (W), the diamagnetic-signal derivative (dW/dt), and the electron temperature (T_e) measured at different frequencies in the range $f = 68$–81 GHz for two pulses with different values of microwave pulse duration and plasma density: (a) $\Delta t_{MW} = 10$ ms, $n_e = 1.7 \times 10^{19}$ m^{-3}, and $P_{rad} > 40$ kW and (b) $\Delta t_{MW} = 6$ ms, $n_e = 1.1 \times 10^{19}$ m^{-3}, and $P_{rad} = 20$ kW. The jump in the diamagnetic-signal derivative measured at the time when the microwave pulse is switched off gives the value of the absorbed power [see formula (2)]. Previously, in [6–8], we discussed in detail the efficiency of plasma heating determined with the help of a "fast" (<100 μs) diamagnetic diagnostics.

With the available multichannel ECE detector system, it was reasonable to perform comparative measurements of the absorbed power by another diagnostic. Figures 2a and 2b show the signals of local measurements of the decrease ΔT_e in the electron temperature after the microwave power is switched off. Analyzing these signals, we can obtain the local and integral data on the absorbed power. As was stated above, the time interval chosen to measure the electron temperature decay time is of crucial importance. For example, points in Fig. 2a were obtained with $\Delta t = 200$ μs (which is typical of our experiments), whereas points in Fig. 2b were obtained with $\Delta t = 700$ μs. The time interval 700 μs results in a nearly flat profile of the power deposition (probably, because of the effect of heat conduction influencing the local variations in ΔT_e). Note that the chosen time interval, which is appropriate for determining the power deposition region, is more than one order of magnitude shorter than the plasma energy confinement time defined by the formula $\tau_e = W/P$ and is shorter than τ_{incr} ($\tau_{incr} = dW/dP$). This was also demonstrated in other stellarators [12, 13]. In this paper, we do not concern ourselves with the factors influencing the time behavior of the temperature decay.

It was found that the experimental points for pulses typical of the experiment can be fitted well by a Gaussian profile: $\Delta T_e = y_0 + A\exp(-x^2/w^2)$, where $x = r/a$. Figures 3a and 3b illustrate typical radial distributions of ΔT_e obtained from experimental data processing. Assuming that the plasma density profile is shaped as

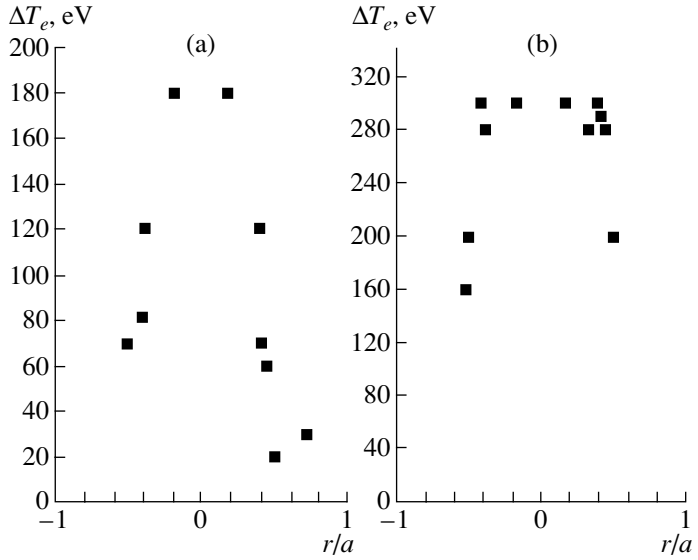

Fig. 2. Local temperature decay for an averaging time equal to (a) 200 and (b) 700 μs.

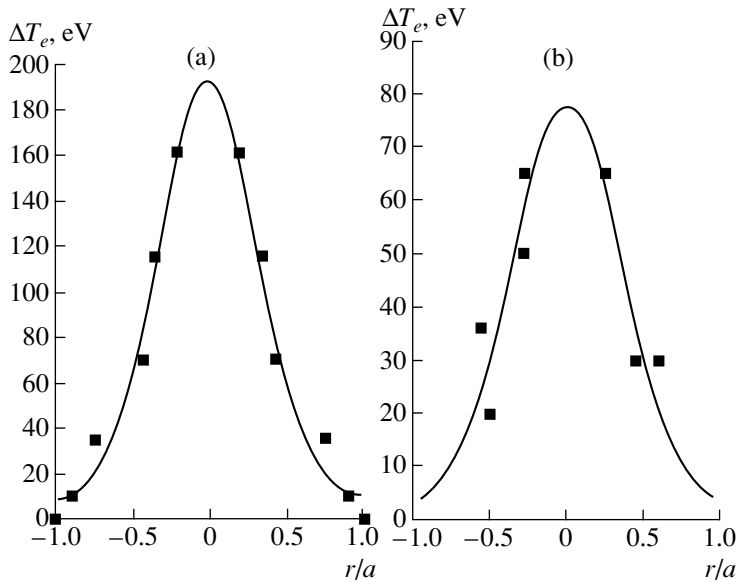

Fig. 3. Radial distribution of ΔT_e fitted with a Gaussian profile for (a) a microwave pulse duration of 6 ms and an average plasma density of 1.12×10^{19} m^{-3} (shot no. 50770) and (b) a microwave pulse duration of 10 ms and an average plasma density of 1.7×10^{19} m^{-3} (shot no. 50766).

$n(x) = n_0(1 - x^4)$ (which is typical of L-2M), for a microwave pulse duration of 6 ms, an average plasma density of 1.12×10^{19} m^{-3}, and an observation time interval of Δt = 200 μs, we obtain from Fig. 3a that the integral absorbed power is P_{abs} = 155 kW. The value of the absorbed power deduced from diamagnetic measurements is 140 kW. In the second case (Fig. 3b), for a microwave pulse duration of 10 ms and an average plasma density of 1.7×10^{19} m^{-3}, we have P_{abs} = 120 kW, whereas diamagnetic measurements yield 95 kW. A satisfactory agreement between the results from the two diagnostics confirms the reliability of the fast diamagnetic diagnostics and the correctness of the choice of the time interval for measuring the temperature variations by the ECE diagnostics.

The heating efficiency $\eta = P_{abs}/P_{in}$ in these experiments was no less than 0.75. The question as to the "missing microwave power" remains unclear.

It should be noted that diamagnetic measurements, which are actually insensitive to the temperature profile, also require a very short observation time (<100 μs) [7]. The agreement between the results from the measurements of P_{abs} by both diagnostics indicate that there exist relatively fast processes carrying energy away from the plasma.

Note also that, in many pulses at an average plasma density of $<10^{19}$ m^{-3}, we observed a more intense ECE (as compared to the thermal ECE) at frequencies below the gyrotron frequency (72–70 GHz) from the LFS (these data are not shown in the figures). This effect may be attributed to electrons emitting at lower frequencies due to the relativistic increase in their mass. In this case, we may speak about the radiative temperature (T_{rad}). When constructing the distributions $\Delta T_e(r)$, T_{rad} was substituted for the data obtained from the ECE measurements at frequencies above the gyrotron frequency (at the same magnetic surface), because it was previously shown that an increase in T_{rad} does not lead immediately to a substantial increase in the diamagnetic signal [14].

4. CONCLUSION

The experiments performed have shown a good agreement between the data on the absorbed microwave power measured by the diamagnetic diagnostics and the local measurements of ΔT_e from the plasma ECE after the microwave power is switched off. The optimum time intervals required to correctly measure the absorbed power have been determined experimentally. However, it remains unclear how to predict this time theoretically.

REFERENCES

1. H. Hartfuss, V. Erckmann, A. Kechrinitis, *et al.*, in *Proceedings of the 9th Joint Workshop on Electron Cyclotron Emission and Electron Cyclotron Heating, Borrego Springs, CA, 1995*, p. 445.
2. H. Maassberg, C. Beidler, V. Erckmann, *et al.*, J. Plasma Fusion Res. **1**, 103 (1998).
3. A. Fujisawa, H. Iguchi, Y. Yoshimura, *et al.*, Phys. Rev. Lett. **82**, 2669 (1999).
4. D. Akulina, G. Batanov, M. Berezhetskii, *et al.*, in *Proceedings of the Joint Meeting of the IAEA TCM on ECRH Physics and Technology for Fusion Devices and*

11th Joint Workshop on Electron Cyclotron Emission and Electron Cyclotron Heating, Oharai, Japan, 1999, Fusion Eng. Des. **53**, 321 (2001).

5. D. K. Akulina, G. M. Batanov, M. S. Berezhetskiĭ, *et al.*, Fiz. Plazmy **26**, 3 (2000) [Plasma Phys. Rep. **26**, 1 (2000)].
6. É. Andryukhina, K. Dyabilin, and O. Fedyanin, Tr. Inst. Obshch. Fiz. Akad. Nauk SSSR **31**, 186 (1991).
7. O. Fedyanin, D. Akulina, E. Andrukhina, *et al.*, J. Plasma Fusion Res. **1**, 235 (1998).
8. O. Fedyanin and E. Andryukhina, in *Proceedings of the 10th International Conference on Stellarators, Madrid, 1995*, p. 128.
9. V. Abrakov, D. Akulina, E. Andryukhina, *et al.*, Nucl. Fusion **37**, 233 (1997).
10. K. M. Likin and B. D. Ochirov, Fiz. Plazmy **18**, 81 (1992) [Sov. J. Plasma Phys. **18**, 42 (1992)].
11. M. Tereshchenko and A. Sakharov, in *Proceedings of the 1998 ICPP and 25th EPS Conference on Controlled Fusion and Plasma Physics, Prague, 1998*, p. 1374; ECA **22C**, 1374 (1998).
12. S. Kubo, H. Idei, T. Shimozuma, *et al.*, in *Annual Report of National Institute for Fusion Science* (NIFS, Toki, 1999), p. 16.
13. S. Kubo, R. Kumazawa, T. Shimozuma, *et al.*, in *Proceedings of 13th Topical Conference on Application of RF Power to Plasma, Annapolis, Maryland, 1999*, p. 237.
14. D. Akulina, G. Gladkov, and Yu. Netchaev, in *Proceedings of the 10th International Conference on Stellarators, Madrid, 1995*, p. 136.

Translated by N. F. Larionova

Plasma Physics Reports, Vol. 28, No. 1, 2002, pp. 71–77. Translated from Fizika Plazmy, Vol. 28, No. 1, 2002, pp. 77–83.
Original Russian Text Copyright © 2002 by Baranov.

LOW-TEMPERATURE PLASMA

Low-Current Moderate-Pressure RF Discharge with Secondary Electron Photoemission

I. Ya. Baranov

Ustinov Baltic State Technical University, St. Petersburg, 198005 Russia

Received April 11, 2001; in final form, June 25, 2001

Abstract—A model is proposed for a low-current RF discharge with secondary electron photoemission from the electrode surface caused by photons originating in the electrode sheath. The low-current state of RF discharges at moderate pressures is peculiar in that the electrons and ions produced during the preceding periods of the RF field promote the development of the discharge during subsequent periods. Since the ion space charge is induced during many periods of the RF field, even comparatively moderate fields in the electrode sheath are sufficient to ensure the conditions under which the current is self-sustaining, in which case the electron photoemission dominates over the remaining secondary processes at the electrode surface. In a low-current RF discharge, the ion–electron emission has essentially no impact on the formation of the electrode sheath because the half-period of the RF field is much shorter than the ion transit time through the sheath. The sheath results from the overlap of the secondary electron avalanches triggered by electron photoemission from the electrode surface. The sheath parameters are determined by the conditions under which the current in the sheath is self-sustaining due to the secondary electron photoemission from the electrode surface. The capacitive susceptance of the electrode sheath is substantially higher than its electrical conductance. Low-current RF discharges can only exist when the time required for the ions to drift through the sheath and reach the electrode is much longer than the half-period of the RF field. © *2002 MAIK "Nauka/Interperiodica"*.

1. INTRODUCTION

At present, RF discharges have many practical applications in plasma chemistry and plasmochemical technologies, as well as in displays and lasers, so that the investigation of RF discharges plays an increasingly important role in modern-day gas-discharge physics.

It was established experimentally that moderate-pressure RF discharges may exist in two states: one in which the current density is significantly lower than the normal current density in a glow discharge and another in which the current density is close to the normal current density. The RF discharges in these states were called, respectively, low-current and high-current RF discharges [1] or α- and γ-discharges [2].

Although different criteria for transitions from one discharge state to another are widely discussed in the literature, a complete understanding of the mechanism for these transitions has not yet been attained.

In [3, 4], the low-current and high-current states of RF discharges were distinguished by the extent to which the displacement and ion currents in the electrode sheath differ from one another. In [5, 6], these states were distinguished by the difference in the rates of gas ionization by plasma electrons and fast electrons that are produced through secondary emission and are accelerated in the sheath. Raizer *et al.* [7] proposed that the sheath breakdown condition be regarded as a criterion for the transition from the low-current to the high-current discharge state.

This paper is devoted to investigating the process of secondary electron photoemission from the electrode surface caused by photons originating in the electrode sheath in a low-current RF discharge. The sheath results from the overlap of the secondary electron avalanches triggered by electron photoemission from the electrode surface and is completely formed on a time scale equal to the electron transit time through the sheath. At moderate pressures, the parameters of the electrode sheath in a low-current RF discharge are governed by the conditions under which the current in the sheath is self-sustaining due to the photon-driven secondary electron emission from the electrode surface, but the capacitive susceptance of the sheath is substantially higher than its electrical conductance. In turn, the high-current state of an RF discharge results from the conditions under which the current is self-sustaining due to the secondary electron emission caused by the bombardment of the electrode surface by the ions, the time scale on which the high-current discharge state is established being equal to the ion transit time through the sheath. The existence of the low-current state of an RF discharge is governed by the value of the ratio of the time required for the ions to drift through the sheath and reach the electrode to the half-period of the RF field. This ratio depends on the current density, which in turn depends on the slope of the current–voltage (*I–V*) characteristic of the sheath. If this ratio is much larger than unity, we are dealing with a low-current RF discharge, and, if this ratio is $\lesssim 1$, the discharge is in the high-current state.

1063-780X/02/2801-0071$22.00 © 2002 MAIK "Nauka/Interperiodica"

As will be shown below, in a low-current RF discharge, the effective coefficient of the secondary electron photoemission from dielectric-coated electrode surfaces may be as large as about unity. In this case, the voltage across the sheath is such that the Faraday dark space is absent and, accordingly, the sheath evolves into a positive column in a uniform fashion.

In addition, a study will be made of the mechanism for filling the positive column with the electrons that originate in the sheath over many RF field periods. Because of these electrons, a low-current RF discharge acquires the nature of a non-self-sustained discharge, thereby becoming stable against the displacement caused by a high-speed gas flow.

2. DISTINGUISHING FEATURES OF A LOW-CURRENT RF DISCHARGE

An RF discharge is in the low-current state if the ions originating in the sheath drift toward the electrode surface over many RF field periods. The low-current state of an RF discharge at a moderate pressure is peculiar in that the electrons and ions produced during the preceding periods of the RF field promote the development of the discharge during subsequent periods. Since the ion space charge is induced during a number of RF field periods, the sheath field should only compensate for a small loss of drifting ions at the electrode surface. For this reason, even a comparatively moderate field in the sheath is sufficient for the current to be self-sustaining, in which case the electron photoemission dominates over the remaining secondary effects at the electrode surface.

During the formation of the electrode sheath in a low-current discharge, the ion-driven secondary electron emission plays a negligible role, because the half-period of the RF field is much shorter than the ion transit time through the sheath. The sheath forms as a result of secondary electron photoemission from the electrode surface. The time scale on which the electrode sheath develops is equal to the electron transit time through the sheath. The sheaths with oscillating boundaries appear at both electrodes simultaneously. As the sheath thickness at one of the electrons increases, the sheath thickness at the other electrode decreases (Fig. 1).

In a low-current RF discharge, the capacitive susceptance of the sheaths is considerably higher than their electrical conductance. The voltage across the sheaths and the current in them become shifted in phase, the phase shift being approximately equal to $\pi/2$. When the current reaches its maximum value, the voltage drops across the sheaths cancel one another [8]. At the times $\omega t = \pi/2$ and $3\pi/2$, the thicknesses of the sheaths are the same and are equal to d, the field in the positive column is the strongest (because of the active current flowing through the column), and there is no phase shift between the voltage and the current (Fig. 1). At the instant when the field in one of the electrode sheaths is the strongest, the thickness of the other sheath is maximum and is equal to $2d$ (the field in the positive column passes through zero at the times $\omega t = 0$, π, and 2π).

Because of the nonlocal effects, the electrons originate near the exit from the sheath. Since the ionization rate depends exponentially on the field strength, the electrons are produced primarily at the time at which the field in the sheath is maximum and the voltage passes through zero and reverses polarity. During the period with this field direction, the electrons do not drift from the electrode toward the center of the discharge gap (Fig. 1). Just after the production of a group of electrons, the sheath starts to shrink toward the electrode. The electrons move in the same direction and at the same speed as the sheath boundary. The fields in the electrode sheaths of a low-current discharge prevent the electrons from reaching the electrode surfaces.

Since the field near the electrode is nonzero over essentially the entire RF field period, the electrons can arrive at the electrode only when the sheath boundary reaches the electrode surface. The potential barrier near the electrode reflects a fraction of the electrons. The reflection coefficient of a metal electrode in the presence of a thin layer of an adsorbed electropositive gas or a gas of dipolar molecules is much larger than that in the absence of such layer, especially for slow electrons, whose energy is insufficient for them to overcome the potential barrier [9]. For slow electrons, the reflection coefficients of metals are 0.1–0.4, while those of dielectrics are 0.5–0.8 [10].

When the electrons are reflected back into the discharge gap, the field in the gap is directed from the reflecting electrode. The sheath forms after the electrons have flown away from the electrode, in which case the electrons move in the weak field of the positive column. Behind the electrons, the field is stronger. As the sheath forms, the excited gas particles produce photons on return to the ground state. When the electrodes initiating low-current RF discharges are coated with dielectric, the nonreflected electrons are captured by surface defects (traps) and fill the surface quantum levels in an energetically forbidden zone [11]. It is precisely these electrons that take part directly in photoemission from the electrode surface during the subsequent RF field period, because the photon energy required to knock them out of a dielectric is lower than that for a metal (it is approximately the excitation energy). The filling of the surface quantum levels by the nonreflected electrons and the presence of the photon-producing electrons that originated during the preceding RF field period and were reflected from the electrode surface govern the evolution of a low-current RF discharge during the subsequent field period: the discharge develops at the expense of the photoemission of electrons from the electrode surface. In this case, during one field period, the ion loss at the electrode surface is small, so that the ion–electron emission is insignificant.

In the mean field of the sheath in a low-current RF discharge, the ions drift slowly toward the electrode. The ions adsorbed on the dielectric surface charge it over many periods of the RF field. In contrast to the ions, the electrons are reflected well from the dielectric surface; therefore, the ion-induced surface charge will remain unchanged. One photon of energy γ_v is capable of knocking many electrons out of the dielectric surface, especially the electropositive coatings [12] and dielectric coatings whose surface quantum levels are prefilled with electrons [11].

In turn, the value of the effective coefficient of the secondary electron photoemission from the electrode surface depends on both the ratio of the number of photons to the number of ions originating in the sheath, α_v/α, and on the mean probability for the ions to reach the electrode surface, $\zeta \sim 0.5$ [13]:

$$\gamma = (\alpha_v/\alpha)\zeta\gamma_v.$$

In moderate sheath fields in a low-current RF discharge, collisions involving electrons make excitation far more probable than ionization. The reason for this is that the excitation probability curves have relatively narrow peaks at low electron energies, while the ionization probability curves have wide peaks at high electron energies [11]. As a result, for moderate fields, the ratio α_v/α is large [14]. In turn, large values of γ_v and α_v/α ensure large values of the effective coefficient of the secondary electron photoemission from the dielectric-coated electrode surface.

3. CALCULATION MODEL

The parameters of a low-current RF discharge were calculated using the approximate model that was developed by Smirnov [3] in order to determine the parameters of the electrode sheath with allowance for the adsorption of ions on the electrode surface. Since the ion space charge in the electrode sheath in a low-current RF discharge is induced over many RF field periods and the ion loss from the sheath per period is small, the ion density in the sheath can be assumed to be approximately constant. That this assumption is valid for a low-current RF discharge was confirmed by comparing it with the results from numerical modeling carried out in [3, 7]. On the other hand, this assumption fails to hold for high-current RF discharges, in which the ion density cannot be constant, because the ions are produced and adsorbed during one half-period of the RF field, so that the sheath alternately appears and disappears at the electrodes. Unlike the conventional numerical methods, our calculation model does not require that the applied voltage be specified and yields correct values of the electrode sheath thickness and the electric field distribution, which are close to those computed from simulation.

During one field period in a low-current RF discharge, the number of ions adsorbed on the electrode surface should be equal, on average, to the number of ionization-produced ions [3]:

$$\langle E(0,t)n_i\mu_i\rangle = \left\langle \gamma E(0,t)n_i\mu_i\left[\exp\int_0^{d(t)}\alpha dx - 1\right]\right\rangle, \quad (1)$$

where α is the ionization rate constant, γ is the secondary photoemission coefficient, $E(0, t)$ is the electric field at the electrode surface, $d(t)$ is the sheath thick-

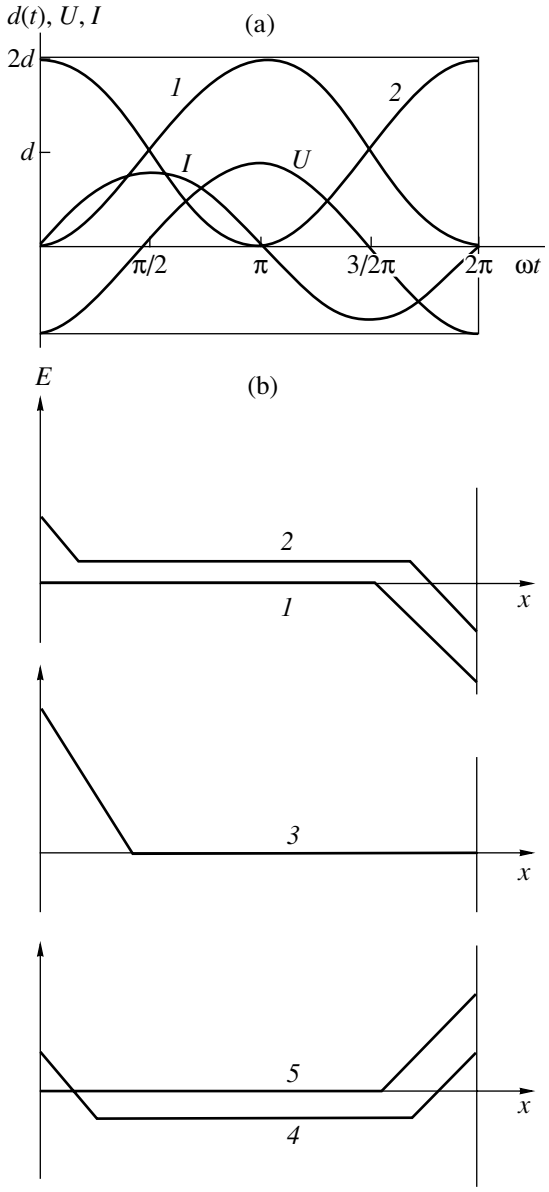

Fig. 1. (a) Time evolutions of the sheath thickness $d(t)$ (curves *1* and *2* refer to the left and right electrodes, respectively), current I, and the total voltage U across the sheaths. (b) Profiles of the field strength E along the discharge gap at different times ωt = (*1*) 0, (*2*) $\pi/2$, (*3*) π, (*4*) $3\pi/2$, and (*5*) 2π.

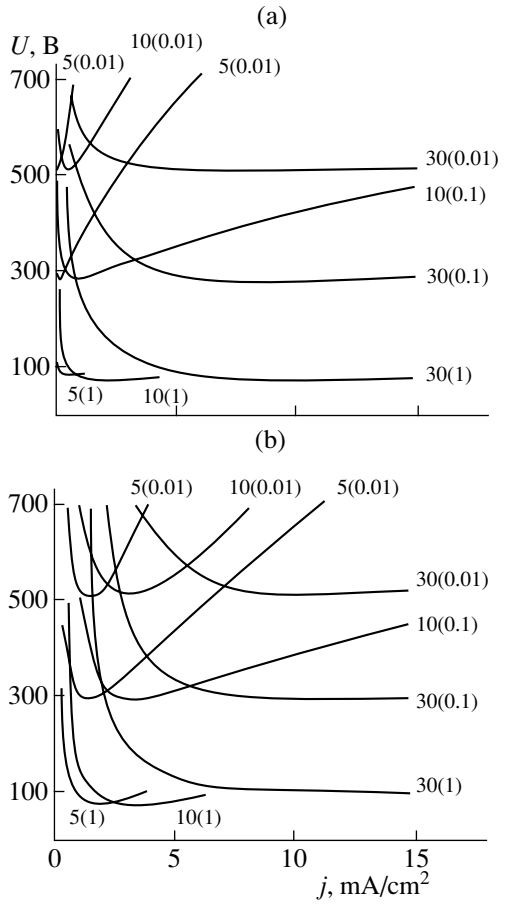

Fig. 2. Dependence of the maximum voltage across the sheath on the current density for the pressures p = 5, 10, and 30 torr; secondary emission coefficients γ = 0.01, 0.1, and 1; and frequencies $\omega/2\pi$ = (a) 1.76 MHz and (b) 13.6 MHz.

ness, n_i is the ion density, μ_i is the ion mobility, and the angular brackets $\langle \ldots \rangle$ indicate time average.

Under the assumption that the ion density in the sheath is constant and that the electric field in the positive column can be neglected, Eq. (1) (which is a generalization of the Townsend condition for the current in the sheath to be self-sustaining), the equations for field oscillations and the thickness of the sheath near the right electrode ($x = x_r$), and Poisson's equation,

$$E(x, t) = E(1 + \cos\omega t - (x_r - x)/d),$$
$$0 < x_r - x < d(t),$$
$$d(t) = d(1 + \cos\omega t),$$
$$n_i = E/4\pi ed$$

determine the period-averaged quantities E and d, which are the same for both electrodes. The ionization rate constant α is described by the dependence

$$\alpha(x, t) = Ap\exp(-Bp/E(x, t)),$$

where the constants A and B depend on the type of gas, p is the gas pressure, and E is the field strength at the electrode surface at the instant when the sheaths near both electrodes are of equal thickness d.

The parameters of a low-current RF discharge in air were calculated by Smirnov [3] for a frequency of 13.6 MHz and $\gamma = 0.1$ and also in my earlier paper [15] for a frequency of 1.76 MHz and $\gamma = 0.3$–1. Although the model developed here does not take into account the production of negative ions, it nevertheless can be applied to air, which is known to be an electronegative gas. The reason for this is the following: experience gained in research on glow discharges in air shows that negative ions are destroyed by the produced active particles. Free electrons originate presumably under the action of nitrogen and oxygen metastable molecules [13].

4. CALCULATED RESULTS AND COMPARISON WITH EXPERIMENT

The results presented below were calculated for different values of the pressure, frequency, and secondary photoemission coefficient γ. For metal electrodes, γ values are appreciably smaller than those for dielectric-coated electrodes because no charge is induced at the metal electrode surface and the surface quantum levels are not filled with electrons. Figure 2 illustrates the dependence of the maximum voltage across the sheath in RF discharges in air on the current density. The curves were calculated for A = 8.61/(cm torr) and B = 254 V/(cm torr) at pressures of p = 5, 10, and 30 torr; frequencies of 1.76 and 13.6 MHz; and γ values of 0.01, 0.1, and 1. The calculated results are correct only for current densities such that the ratio of the ion transit time through the sheath to the half-period of the RF field is much larger than unity, in which case the ion density in the sheath is approximately constant and the discharge is in the low-current state. The dependence of this ratio on the current density is illustrated in Fig. 3. In the case at hand, the current in the sheath is dominated by the displacement current, but the parameters of the sheath are determined by the processes of electron production in it, i.e., by the active current. At the point at which the I–V characteristic of the sheath is minimum, the current density calculated from the total current magnitude (equal to the square root of the sum of the squared amplitudes of the displacement and active currents) is much lower than the normal current density in a glow discharge (Fig. 2).

At a pressure of 5 torr, the I–V characteristic of the sheath has a pronounced minimum in the current density range in which the ions are adsorbed on the electrode surface over many RF field periods for all γ values under consideration. The calculated current density (Fig. 2) agrees fairly well with the density value 0.5 mA/cm^2, measured in experiments with RF discharges initiated by metal (brass) electrodes in air (Fig. 4a), the experimental parameters being the following: the frequency is 1.76 MHz, the distance

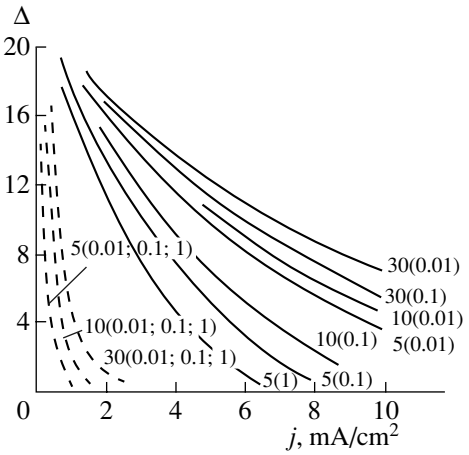

Fig. 3. Dependence of the ratio Δ of the ion transit time through the sheath to the half-period of the RF field on the current density for the pressures p = 5, 10, and 30 torr; secondary emission coefficients γ = 0.01, 0.1, and 1; and frequencies $\omega/2\pi$ = 1.76 MHz (dashed curve) and 13.6 MHz (solid curve).

between the electrodes is 30 mm, the voltage is 500 V, the current is 0.24 A, the area of the electrode surface is 48 cm^2, and the gas flow velocity is 100 m/s. As the pressure increases, the minimum in the *I–V* characteristic becomes less pronounced and shifts toward higher current densities, for which the ratio of the ion transit time through the sheath to the half-period of the RF field decreases to a considerable extent (Fig. 3). It is for this reason that, in experiments with uncoated metal electrodes, the low-current state of an RF discharge at a frequency of 1.76 MHz was not achievable at pressures higher than 5 torr.

The calculated results show that, in a low-current RF discharge, the current density depends weakly on γ, because the current in the sheath is dominated by the displacement current. However, for large values of the effective secondary photoemission coefficient γ, which are characteristic of dielectric-coated electrodes, the voltage across the sheath in a low-current RF discharge is strongly sensitive to the γ value. In a low-current RF discharge in air, the voltage across the sheath for $\gamma = 1$ is lower than that for $\gamma = 0.01$ by an amount greater than 400 V (Fig. 2). Such a large amount explains the absence of the Faraday dark space in discharges initiated by electrodes with a 10-mm-thick dielectric quartz ceramic coating (the remaining parameters are the following: the pressure is 30 torr, the voltage is 4.2 kV, the current is 1.3 A, the area of the electrode surface is 128 cm^2, and the gas flow velocity is 100 m/s) and its presence in discharges initiated by uncoated metal electrodes (Fig. 4). A decrease in the voltage across the

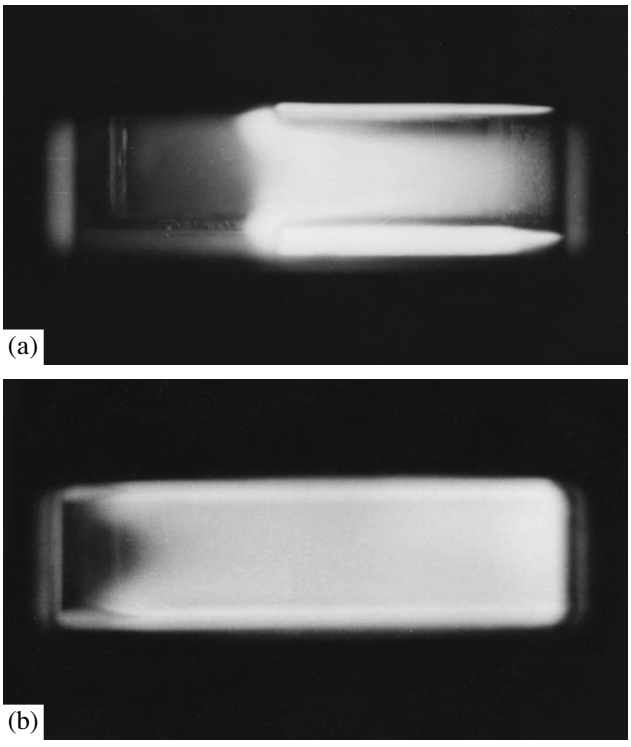

Fig. 4. Photographs of low-current RF discharges at the frequency $\omega/2\pi$ = 1.76 MHz in an air flow with a velocity of 100 m/s between the electrodes with a spacing of 30 mm. Photograph (a) was taken in experiments with brass electrodes at p = 5 torr and j = 0.5 mA/cm^2, and photograph (b) was taken in experiments with dielectric-coated electrodes at p = 30 torr and j = 1 mA/cm^2. The air flow is directed from right to left.

sheath results in the disappearance of the electron flux from the sheath, thereby explaining the absence of the Faraday dark space, which is associated precisely with this flux [13]. In addition, large γ values change the slope of the left (descending) part of the *I–V* characteristic of the sheath: this part shifts toward lower current densities (toward the ordinate axis) (Fig. 2). When the slope is sufficiently gentle, the electrode sheath can be sustained in a steady state at the left part the *I–V* characteristic at a negative gradient of the voltage [16], as is the case in experiments with 1.76-MHz RF discharges initiated by dielectric-coated electrodes (with a spacing of 30 mm) in air at a pressure of 60 torr. At higher pressures, the discharge develops in the form of many filaments; such discharge evolution is characteristic of the case when the density of the secondary electrons is insufficiently high for their avalanches, triggered by photoemission from the electrode surface, to overlap [17]. Moreover, Seguin *et al.* [17] succeeded in initiating RF discharges in the low-current state using electrodes with a 10-mm dielectric coating and with a 0.5-mm dielectric coating, in which case the ballast resistance of the discharge plays a far lesser role. However, such discharge states were achieved at pressures lower than 15 torr.

For RF discharges in gases other than air, the position of the minimum point of the *I–V* characteristic changes. Thus, owing to the constants $A = 31$/(cm torr) and $B = 34$ V/(cm torr), the *I–V* characteristic for discharges in helium is minimum at lower current densities in comparison with those for discharges in air. That is why the pressure range in which low-current RF discharges can be initiated in helium is wider than that for discharges in air. This same conclusion was reached in the experiments of [1].

5. FILLING OF THE DISCHARGE GAP WITH THE ELECTRONS PRODUCED IN THE SHEATH

The electrons that are produced near the sheath boundary in the preceding period of the RF field and are reflected from the electrode at the instant when the sheath boundary reaches the electrode surface during the subsequent RF field period can fill the discharge gap until the field in the gap pushes them away from the electrode. Since the electrons that have been reflected from the electrodes fill the discharge gap and are trapped in the positive column by the sheath fields, which point toward the electrodes and prevent them from reaching the electrode surfaces, the electron density in the positive column can become elevated, as is the case in non-self-sustained discharges. It is because of this effect in a low-current RF discharge and because the currents in the sheaths are closed primarily by the displacement current that the discharge region is not displaced under the action of high-speed gas flows like those in experiments with air [18, 19].

In high-speed flows of electronegative gases (e.g., air), electron losses increase with flow velocity if the electron transit time through the discharge region in the longitudinal direction is shorter than the time required for the density of active molecules (which give rise to electron attachment [13]) to reach a steady level. When the electron density in the positive column is elevated, the loss of active molecules is compensated for by an increase in the field strength in the column, leading to the strong dependence of the voltage on the gas flow velocity, as is the case in the experiments of [20] and experiments with non-self-sustained discharges. In this case, the current in the electrode sheaths in a low-current RF discharge is dominated by the displacement current.

The effect of the filling of the discharge gap with the electrons from the electrode sheath depends on the gap length, the duration of the half-period of the RF field, and the electron drift velocity. If the half-period is long enough for the electrons to fill the entire discharge gap, then the *I–V* characteristic of the positive column is increasing and the column plays the role of the ballast for the sheath. The longer the discharge gap, the lesser is the extent to which the sheath is ballasted by the column. The reason for this is that the half-period of the RF field is too short for the electrons reflected from the electrode to fill the entire discharge gap. As a result, the current density increases and the ratio of the ion transit time through the sheath to the half-period of the RF field changes (Fig. 3). This circumstance may explain the dependence of the state of an RF discharge on the electrode spacing [1].

6. CONCLUSION

A physical model is constructed in which the existence of the low-current state of an RF discharge at moderate pressures is attributed to the mechanism implying that the current in the electrode sheath is self-sustained due to the secondary electron photoemission from the electrode surface. A low-current RF discharge can be initiated when the ions originating in the electrode sheath are adsorbed on the electrode surface over many RF field periods. Since the ion space charge is also induced over many RF field periods, even comparatively moderate fields are sufficient to ensure the conditions under which the secondary processes at the electrode surface are self-sustaining.

The parameters of the electrode sheath are determined by the conditions for the current in the sheath to be self-sustained due to the secondary electron photoemission from the electrode surface, in which case the capacitive susceptance of the sheath is substantially higher than its electrical conductance.

The electrons generated owing to ionization in the sheath and reflected from the electrode during the preceding RF field period produce photons during the subsequent RF field period. In turn, these photons knock

the new electrons out of the electrode surface. A low-current RF discharge develops as a result of the secondary electron photoemission and the overlap of the secondary electron avalanches.

The moderate field strength in the sheath, the charging of the dielectric-coated electrode surface by the ions, and the filling of the surface quantum levels by electrons ensure the high photoemission yield γ_v and the high effective value of the secondary electron photoemission coefficient γ during the corresponding RF field periods.

The current density in a low-current RF discharge is weakly sensitive to the γ value, because the total current in the electrode sheath is dominated by the displacement current. On the other hand, large γ values strongly affect the voltage across the sheath. In turn, the value of the voltage across the sheath is also responsible for the appearance of both an electron flux at the sheath boundary and the Faraday dark space, which are absent in a low-current RF discharge initiated by dielectric-coated electrodes.

The effect of large γ values is such that the descending part of the *I–V* characteristic of the sheath shifts toward lower current densities (toward the ordinate axis) and the slope of this part changes. It is because of this effect that low-current RF discharges can be initiated by dielectric-coated electrodes at elevated pressures. The development of a low-current discharge is promoted by an increasing *I–V* characteristic of the positive column (provided that the electrons from the sheath fill the entire discharge gap) and the ballasting effect of the dielectric coating reactance.

The existence of the low-current state of an RF discharge is governed by the value of the ratio between the time required for the ions to drift through the sheath toward the electrode and the half-period of the RF field. For the high-current state of an RF discharge, this ratio is $\leqslant 1$, whereas, for the low-current state, it is much larger than unity. Although the capacitive current in the electrode sheath of a low-current RF discharge is substantially higher than the active current, the sheath parameters are determined by the conditions under which the current is self-sustained due to the secondary electron photoemission (with the effective coefficient γ) from the electrode surface.

The physical model proposed here for describing low-current moderate-pressure RF discharges made it possible to explain the normal value of the current density and the dependence of the discharge shape on pressure, electrode spacing, the type of gas, and the coating of the electrodes with a dielectric, as well as such effects as the absence of the Faraday dark space in discharges initiated by dielectric-coated electrodes and the stability of the discharge region against the displacement caused by a high-speed gas flow.

REFERENCES

1. N. A. Yatsenko, Zh. Tekh. Fiz. **51**, 1195 (1981) [Sov. Phys. Tech. Phys. **26**, 678 (1981)].
2. S. M. Levitskiĭ, Zh. Tekh. Fiz. **27**, 1001 (1957) [Sov. Phys. Tech. Phys. **2**, 913 (1958)].
3. A. S. Smirnov, Zh. Tekh. Fiz. **54**, 61 (1984) [Sov. Phys. Tech. Phys. **29**, 34 (1984)].
4. A. S. Kovalev, A. I. Nazarov, A. T. Rakhimov, *et al.*, Fiz. Plazmy **12**, 1264 (1986) [Sov. J. Plasma Phys. **12**, 731 (1986)].
5. V. A. Godyak and A. S. Khanneh, IEEE Trans. Plasma Sci. **14**, 112 (1986).
6. Ph. Belenguer and J. P. Boeuf, Phys. Rev. A **41**, 4447 (1990).
7. Yu. P. Raizer, M. N. Shneĭder, and N. A. Yatsenko, *High-Frequency Capacitive Discharge: Physics. Experimental Technique. Applications* (Nauka, Moscow, 1995).
8. A. S. Kovalev, A. T. Rakhimov, and V. A. Feoktistov, Fiz. Plazmy **7**, 1411 (1981) [Sov. J. Plasma Phys. **7**, 779 (1981)].
9. V. L. Granovskiĭ, in *Electric Current in a Gas* (Gostekhizdat, Moscow, 1952), p. 209.
10. L. N. Dobretsov and M. V. Gomoyunova, in *Emission Electronics* (Nauka, Moscow, 1966), p. 330.
11. A. N. Arsen'eva-Geĭl', *Outer Photoemissive Effect from Semiconductors and Dielectrics* (Gostekhizdat, Moscow, 1957).
12. A. von Engel, *Ionized Gases* (Claredon Press, Oxford, 1955; Fizmatgiz, Moscow, 1959).
13. Yu. P. Raizer, *Gas Discharge Physics* (Nauka, Moscow, 1987; Springer-Verlag, Berlin, 1991).
14. G. Francis, *Ionization Phenomena in Gases* (Butterworths, London, 1960; Atomizdat, Moscow, 1964).
15. I. Ya. Baranov, Fiz. Plazmy **21**, 456 (1995) [Plasma Phys. Rep. **21**, 431 (1995)].
16. Yu. D. Korolev and G. A. Mesyats, in *The Physics of Pulsed Breakdown of Gases* (Nauka, Moscow, 1991), p. 128.
17. H. J. Seguin, J. Tulip, and D. KcKen, Appl. Phys. Lett. **28**, 487 (1976).
18. N. A. Yatsenko, Teplofiz. Vys. Temp. **20**, 1044 (1982).
19. I. Ya. Baranov, Fiz. Plazmy **22**, 1062 (1996) [Plasma Phys. Rep. **22**, 964 (1996)].
20. I. Ya. Baranov, Fiz. Plazmy **21**, 554 (1995) [Plasma Phys. Rep. **21**, 522 (1995)].

Translated by G. V. Shepekina

Plasma Physics Reports, Vol. 28, No. 1, 2002, pp. 78–81. Translated from Fizika Plazmy, Vol. 28, No. 1, 2002, pp. 84–87.
Original Russian Text Copyright © 2002 by Kvitsinskiĭ, Mudretskaya, Pavlov, Perevoznikov.

LOW-TEMPERATURE PLASMA

Characteristic Features of Energy Transfer in the Wall Region of a Lithium Vapor Discharge

V. A. Kvitsinskiĭ*, E. V. Mudretskaya*, S. N. Pavlov*, and S. A. Perevoznikov**

**Eleĭ-2 Research and Production Corporation, Kiev, Ukraine*

***Associated Institute for High Temperatures, Russian Academy of Sciences, Izhorskaya ul. 13/19, Moscow, 127412 Russia*

Received June 21, 2001; in final form, July 18, 2001

Abstract—A series of experiments with a fully ionized turbulent lithium plasma is described. Discharges with a heat flux density onto the wall of 1–3 kW/cm^2 and an electron density of ~10^{15} cm^{-3} are obtained. The energy can be transferred to the wall by both Li^+ and Li^{++} ions. The measurements show that the photon flux corresponding to the main resonant transition of lithium atoms is a factor of 10^4–10^5 less than it could be if all the ions arriving at the wall recombined there. A mechanism is proposed for energy transfer onto the wall via the recombination of Li^{++} ions to Li^+ ions in the cold wall region of the discharge and the subsequent energy emission by Li^+ ions. © *2002 MAIK "Nauka/Interperiodica".*

1. INTRODUCTION

Increasing the fraction of radiative energy flux in the total energy flux onto the wall of a thermonuclear device is a promising method for protecting the first wall from sputtering [1]. At present, the efficiency of energy reemission at the periphery of a tokamak with the use of special additives can attain 90%. A further increase in the fraction of the reradiated energy can be achieved using lithium vapor.

The evaporation and ionization of lithium films can also be used to protect the surface of divertor plates from ultra-high-power fluxes arising during current disruptions.

2. DESCRIPTION OF THE EXPERIMENT

Experiments were carried out in the Robotron device intended for producing a dense, strongly ionized metal vapor plasma. A schematic of the experimental setup is shown in Fig. 1. An initial plasma was produced by a vacuum arc discharge between cathode *12* and anode *11*, shaped as a diaphragm. Solid lithium was loaded into the cathode. Electrode *5* was used to initiate the vacuum arc. The injector was supplied from a capacitor bank with a stored energy of up to 700 J. The injector discharge current was limited by a ballast resistor. A lithium plasma flowed into a quartz tube with an inner diameter of 26 mm, in which the cathode and anode of the main discharge were placed. The main discharge was powered by two capacitor banks that could be switched on independently with a controlled time delay. The maximum energy of the two charged banks was 2.5 kJ. The discharge current (up to 2.5 kA) was limited by a ballast resistor. The cathode of the main discharge was also equipped with an ignition electrode (which is not shown in the figure). All the electrodes were made from fine-grained vanadium.

Unlike in [2], the injector was placed inside a pulsed solenoid with a magnetic-field induction of up to 0.05 T. The solenoid served to improve the transportation of the lithium plasma from the injector to the main discharge. Both the injection and the solenoid current durations were on the order of 1 ms, and the main discharge duration was 4–5 ms.

Typically, the delay time between the start of injection and the beginning of the main discharge was 0.3–0.5 ms. In discharges, we observed voltage spikes with

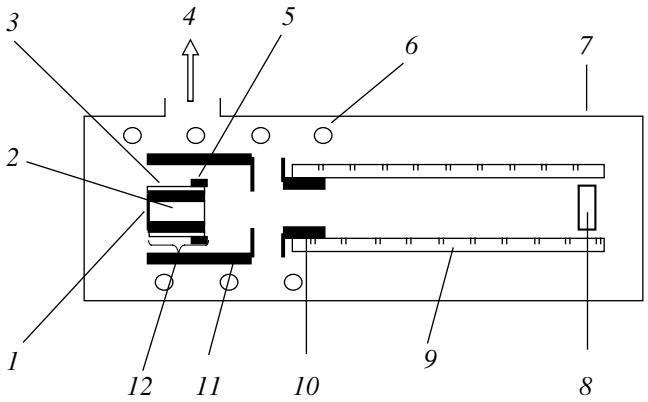

Fig. 1. Experimental setup: (*1*) metal cylinder, (*2*) Li, (*3*) insulator, (*4*) pumping-out, (*5*) ignition electrode, (*6*) solenoid winding, (*7*) vacuum chamber, (*8*) main discharge cathode, (*9*) quartz tube, (*10*) main discharge anode, (*11*) injector anode, and (*12*) injector cathode.

1063-780X/02/2801-0078$22.00 © 2002 MAIK "Nauka/Interperiodica"

a duration of about 1ms. In some shots, the spike amplitude exceeded the initially applied voltage.

The current was measured by Rogowski coils. The electrode voltage was determined from the current flowing through a resistor by using a galvanically decoupled pair of a photodiode and an LED. The discharge operated in a repetitive mode with a repetition rate of 0.2 Hz.

The optical measurements were performed in the visible spectral region with the help of a monochromator with a linear dispersion of 1.3 nm/mm or interference filters. Radiation was observed either across the discharge tube (in the mid-perpendicular plane) or along the system axis through the aperture in the cathode of the main discharge. The radiation was detected by photomultipliers equipped with broadband amplifiers. The spectral complex was calibrated with a reference source. The discharge spectrum contained the lines of atomic and ionized lithium and vanadium, as well as the lines of the Balmer series of impurity hydrogen.

The experimental data were recorded with the help of a multichannel ADC with a maximum sampling frequency of 500 kHz.

3. RESULTS OF MEASUREMENTS

The electron plasma density was measured from the Stark broadening of the H_β line. The line profile was scanned by readjusting the monochromator slit after every shot. The scanning step was 0.025 nm. Simultaneously, the second photomultiplier traced the integral line intensity, which was then used to normalize the measured line intensity at a fixed wavelength. When processing the line profiles, both the instrumental function and the Doppler broadening profile were assumed to be Gaussian. Their relative contributions were taken into account by using a Voigt function. The measurements were performed for three different values of the discharge current. It turned out that, under our experimental conditions, the Doppler broadening could be neglected. Results of these measurements are shown in Fig. 2.

The profile of the electron temperature and its absolute value were not measured. The evaluation of the average temperature from the Spitzer conductivity of the plasma seems to be incorrect because of strong plasma turbulence. In [3], the following relationship was obtained for a steady-state discharge (assuming that heat loss is governed by heat conduction): $eaE/T_0 \approx 1$, where a is the tube radius, E is the applied field, and T_0 is the temperature at the axis. According to this formula, the temperature T_0 in our discharges is on the order of 10 eV. Because of the convective heat exchange caused by turbulence, this formula gives an overestimated value of the temperature.

The typical intensity of the 670.7-nm resonant atomic lithium radiation at a discharge current of 2.1–2.5 kA was 5×10^{14}–2×10^{15} photon/(cm^2 s sr). In repetitive discharges, this intensity initially grows from shot to shot and, then, is stabilized at a certain level.

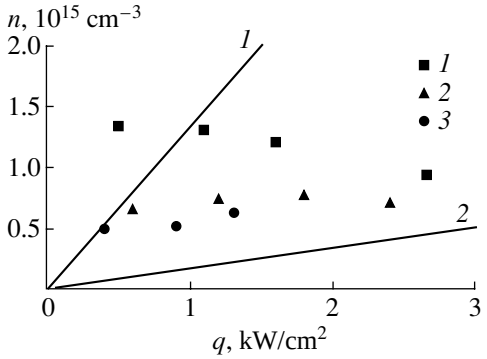

Fig. 2. Electron density for different densities of the heat flux onto the wall of the discharge chamber. Experimental points *1*, *2*, and *3* correspond to the electron densities in shots with maximum discharge currents of 2.5, 2, and 1 kA, respectively. Straight lines *1* and *2* are described in the text.

As in [4], we observed the emission of singly charged lithium ions corresponding to the 2^3P–2^3S_1 548.5-nm transition. The averaged (over the discharge cross section) density of the excited ions in the 2^3P state at the maximum of the radiation pulse was 2×10^8–1.5×10^9 cm^{-3}.

4. DISCUSSION OF THE RESULTS

Let us examine the experimental data on the Stark broadening of the H_β line. The choice of the axes in Fig. 2 seems to be most informative, because, if radiation is neglected, then the measured density turns out to be closely related to the heat flux onto the wall. If only Li^+ ions arrive at the wall, then this flux can be estimated as $q_1 = n_{i1}V_iE_1$ (line *1*), where n_{i1} is the density of Li^+ ions, $V_i \approx 6 \times 10^5$ cm/s is the ion-acoustic velocity, and $E_1 \approx 10$ eV is the energy transferred to the wall by a Li^+ ion (including the ionization energy).

When designing the Robotron device, it was suggested by one of the authors (E.V. Mudretskaya) that Li^{++} ions would constitute a considerable fraction of the plasma ions in spite of the very high energy of secondary ionization. It was also believed that the hot wall of a quartz tube would not be substantially destroyed by the lithium ion flow. The relative stability of quartz tubes against the reduction by lithium ions was confirmed in the first experiments with a lithium plasma [4]. These experiments demonstrated the presence of radiation from lithium ions attributed to the 2^3P–2^3S_1 transition from the excited level with an energy of 61.28 eV, which indirectly confirmed the presence of Li^{++} ions.

We also observed a rather intense radiation from singly charged lithium ions in this line. Since the

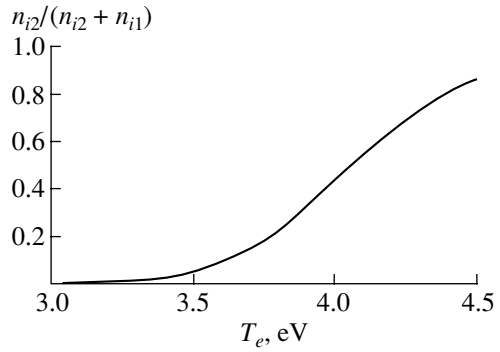

Fig. 3. Relative content of doubly charged ions in the plasma as a function of the electron temperature (calculated by the Saha formula).

energy difference between this level and the doubly ionized state of atomic lithium (E_2 = 75.64 eV) is relatively small, we can use the Saha–Boltzmann formula to estimate the density of Li^{++} ions from the measured density of singly charged ions in the 2^3P state:

$$N_z N_e / n_{z-1,k} = 2g_z \times 3 \times 10^{21} T^{3/2} \exp[-(I_{z-1} - E_k)/T] \quad (k > 1), \tag{1}$$

where N_z is the density of ions with the charge number Z (in cm^{-3}); N_e is the electron density (in cm^{-3}); g_z is the total statistical weight of ions with the charge number Z; $n_{z-1,k}$ is the reduced (per unit statistical weight) density of ions with the charge number $Z - 1$ in the kth state (in cm^{-3}); I_{z-1} and E_k are the ionization energy of an ion with the charge number $z - 1$ and the excitation energy of its kth level (in eV), respectively; T is the electron temperature (in eV); and $Z = 0$ corresponds to neutrals.

Estimates show that, at the above density of the excited ions and a temperature of 3–4.5 eV, the expected density of Li^{++} ions is $(0.2–4) \times 10^{14}$ cm^{-3}. Using the Saha equation, we can estimate the degree of secondary ionization in the temperature range 3–4.5 eV. Figure 3 shows the calculated curve $n_{i2}/(n_{i1} + n_{i2})$ for the total density $n_i = n_{i1} + n_{i2} = 10^{15}$ cm^{-3}.

If only Li^{++} ions arrive at the wall, then the heat flux onto the wall can be estimated as $q_2 = n_{i2} V_i E_2$, where $n_{i2} = 2n_e$ is the density of Li^{++} ions and $E_2 \approx 80$ eV (Fig. 2, line *2*). We can see that most of the experimental points fall in a domain between the lines n_{i1} and n_{i2}. These lines correspond to an ion flux of 10^{20}–10^{21} ion/(cm^2 s).

If the probability of the neutralization of an ion arriving at the wall is close to unity, then the discharge is sustained by an intense recycling of lithium on the discharge chamber wall. Hence, every ion neutralized on the wall must be ionized again. The probability of electron-impact excitation is usually higher than the probability of ionization. Therefore, it seems reasonable to assume that the lithium resonant radiation flux should be on the order of or higher than the ion energy flux onto the wall. However, the experimental values of the lithium resonant radiation flux are lower by several orders of magnitude: 5.5×10^{14}–2×10^{15} photon/(cm^2 s sr).

This discrepancy can be explained by the contribution from radiation associated with the three-body recombination of Li^{++} ions in the cold edge plasma. Let us estimate the thickness of a plasma layer with the temperature T_e = 0.4 eV, required to radiate a power of $q \sim 1$ kW/cm^2, assuming that ion recombination is accompanied by the emission of an energy of 75 eV. The number of recombination events per unit volume in unit time is given by the expression $N = \alpha n_e^2 n_{i2}$ ($Z = 2$) [5], where $\alpha \approx 5 \times 10^{-26} T_e^{-9/2}$ cm^6/s is the recombination rate constant. Then, at the densities $n_e \approx 10^{15}$ cm^{-3} and $n_{i2} \approx 10^{14}$ cm^{-3}, the sought thickness is equal to $L \approx q/(N \times 75 \times 1.6 \times 10^{-19}) \approx 0.3$ cm. Upon three-body recombination, the third particle carries away an energy on the order of T_e and, consequently, the bound electron appears at one of the high levels. The remaining energy on the order of $\sim(E_i - T_e) \sim 70$ eV is lost in cascade transitions.

The mechanism for the transport of a Li^{++} plasma to the low-temperature region can probably be associated with turbulence caused by the current–convective instability [2]. A characteristic parameter of the problem on the onset of helical instability is the so-called magnetic Rayleigh number [6]: $\mathrm{Ra}^* = 2\sigma EBa^3\sigma_T/c\eta\chi$, where $\sigma \approx 2e^2 n\tau_e/m_e$ is the plasma conductivity, $\sigma_T = d\ln\sigma/d\ln T = 1.5$, $\eta \approx nT_i\tau_i$ is the ion viscosity, and $\chi = k/5n \approx \frac{3}{5}\frac{T_e\tau_e}{m_e}$ is the thermal diffusivity. The instability develops when $\mathrm{Ra}^* > 3191$. Substituting the expressions for the ion viscosity and the electron thermal diffusivity into the formula for Ra* and estimating the longitudinal magnetic field produced by the current itself as $B \approx 2\pi a\sigma E/c$, we obtain

$$\mathrm{Ra}^* \simeq 0.8\left(\frac{T_e}{T_i}\right)^{5/2}\left(\frac{eEa}{T_e}\right)^2 r_e a^2 n, \tag{2}$$

where $r_e = e^2/m_e c^2$ is the classical electron radius. In the initial phase of the discharge, the time during which the ion and electron temperatures equalize can be longer than the growth time of the instability near the axis, so that the temperatures T_e and T_i can differ substantially. Assuming for estimates that $(eEa/T_e)^2 \approx 2$ and $T_e/T_i \approx 3$, we obtain that the helical instability develops under the condition $n \geq 10^{14}$ cm^{-3}, which is satisfied in the discharges under study.

5. CONCLUSIONS

(i) The photon flux corresponding to the resonant lithium line is a factor of 10^4–10^5 lower than it could be if all the ions arriving at the wall recombined there, assuming that energy is totally transferred by these ions.

(ii) The most probable mechanism for heat transfer onto the wall is the recombination of Li^{++} ions to Li^+ ions in the cold wall region of the discharge and the subsequent energy emission by Li^+ ions.

ACKNOWLEDGMENTS

This study was carried out under the supervision of A.V. Nedospasov and with his creative participation. We thank A.V. Zhmendak for technical support in operating the Robotron device and V.F. Virko for his help in preparing and performing experiments.

REFERENCES

1. U. Samm, G. Bertschinger, P. Bogen, *et al.*, Plasma Phys. Controlled Fusion **35**, B167 (1993).
2. A. V. Nedospasov, E. V. Mudretskaya, and A. V. Zhmendak, Dokl. Akad. Nauk **374**, 754 (2000) [Dokl. Phys. **45**, 531 (2000)].
3. E. V. Mudretskaya, A. V. Nedospasov, S. A. Perevoznikov, and A. V. Zhmendak, in *Proceedings of the XXIV International Conference on Phenomena in Ionized Gases, Warsaw, 1999*, Vol. 4, p. 49.
4. A. V. Nedospasov, G. V. Sergienko, N. M. Zykova, *et al.*, J. Nucl. Mater. **618**, 266 (1999).
5. L. M. Biberman, V. S. Vorob'ev, and I. T. Yakubov, *Kinetics of Nonequilibrium Low-Temperature Plasmas* (Nauka, Moscow, 1982; Consultants Bureau, New York, 1987).
6. V. D. Khait, Preprint No. 2-025 (Inst. for High Temperatures, USSR Academy of Sciences, Moscow, 1977).

Translated by N. F. Larionova

Plasma Physics Reports, Vol. 28, No. 1, 2002, p. 82. Translated from Fizika Plazmy, Vol. 28, No. 1, 2002, p. 88.
Original Russian Text Copyright © 2002 by the Editorial Board.

JUBILEES

Lev Mikhaĭlovich Kovrizhnykh (In Honor of His 70th Birthday)

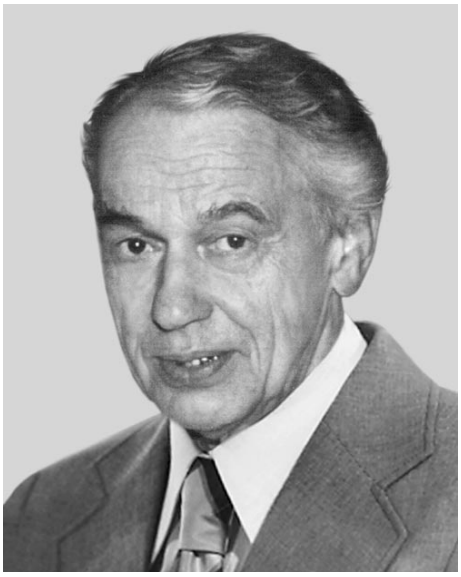

September 12, 2001 was the 70th birthday of Professor Lev Mikhaĭlovich Kovrizhnykh, a world-famous theoretical physicist, the head of the Plasma Physics Department at the Institute of General Physics of the Russian Academy of Sciences, and the Deputy Editor-in-Chief of our journal.

After graduating from Moscow State University in 1954, Kovriznykh began to work at the Lebedev Physical institute, in the laboratory headed by V.I. Veksler. During the first several years, he carried out a series of studies on the conventional methods for charged particle acceleration and the theory of new methods of radiative acceleration of plasma bunches. Based on these studies, he defended his candidate's dissertation in 1959. Then, he turned to the field of plasma physics and controlled nuclear fusion, where his talent as a theoretical physicist blossomed.

Kovriznykh's works on plasma turbulence and nonlinear interaction of waves are widely known. In 1967, he defended his doctoral dissertation on the statistical theory of wave interaction in plasma. In subsequent years, he repeatedly applied himself to these problems, in particular, to the problem of charged particle acceleration in the interaction of high-power electromagnetic radiation with plasmas.

Kovriznykh contributed greatly to controlled fusion research. He was one of the initiators of the studies on high-temperature plasma physics at the institute. His pioneer works on the stability of the structure of helical magnetic fields and the neutralization of resonant perturbations resulted in the development of a new stellarator concept that is presently used at all the leading stellarator laboratories in the world.

Kovriznykh is one of the founders of the neoclassical transport theory, underlying the modern concept of magnetic plasma confinement. For these works, he was awarded a Lenin Prize in 1984.

For almost two decades, Kovriznykh has been the head of the Plasma Physics Department (until 1982, headed by Professor M.S. Rabinovich). During this time, the experimental investigations at stellarators created at the Department showed considerable promise for using this type of magnetic confinement devices in controlled fusion research. Kovriznykh's works in this field received wide recognition; now, he is one of the leaders of the stellarator program in the world.

Kovriznykh conducts important organizing work. He is the chairman of the Scientific Council of the Russian Academy of Sciences on the problem "Plasma Physics," a member of the editorial boards of a number of Russian and foreign journals, a member of several international committees, and a member of the program and organizing committees of several large international conferences.

Lev Mikhaĭlovich greeted his 70th birthday full of ideas and energy. The members of the Editorial Board and his colleagues from the Institute of General Physics wish him robust health, happiness, and fulfillment of all his creative intentions.

1063-780X/02/2801-0082$22.00 © 2002 MAIK "Nauka/Interperiodica"